SCIENCE SUPPORT TO NRL'S SPACE SCIENCE DIVISION:

INSTRUMENT SUPPORT, DATA ANALYSIS, MODEL DEVELOPMENT, AND THEORETICAL STUDIES CONCERNING COMPOSITION AND PROCESSES OF THE MIDDLE AND UPPER ATMOSPHERE AND SOLAR ATMOSPHERE

Final Report

Contract No. N00014-88-C-2281

Prepared for:

Space Science Division
The Naval Research Laboratory
4555 Overlook Ave., SW
Washington, DC 20375-5000

Prepared by:

Computational Physics, Inc.
2750 Prosperity Ave.
Suite 600
Fairfax, VA 22031

September, 1991

TABLE OF CONTENTS

INTRODUCTION

OVERVIEW AND SUMMARY

APPENDICES

1. UVPI Imaging of Auroral Limb Data

2. A Study of O^+ 834 Å Limb Emission to be Observed by SSULI on Satellite DMSP

3. Development of an Inversion Algorithm for Retrieving Mesospheric O_3 and Thermospheric O_2 Density Profiles from SUSIM Solar Occultation Data

4. Development of a Climatology of the Middle Atmosphere for NRL's Middle Atmosphere Program

5. Modeling of Millimeter-Wave Emissions of the Middle Atmosphere Observed from the Ground and Development of Constituent Retrieval Algorithms

6. Characterization of the Remote Atmospheric and Ionospheric Detection System (RAIDS) Instrument

7. Investigation of Solar Atmospheric Processes in Support of the Solar-Terrestrial Relations Branch of NRL

DISCLAIMER NOTICE

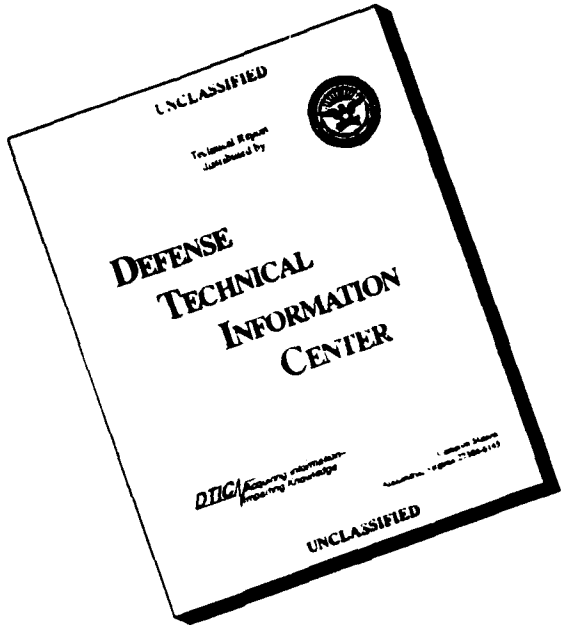

THIS REPORT IS INCOMPLETE BUT IS THE BEST AVAILABLE COPY FURNISHED TO THE CENTER. THERE ARE MULTIPLE MISSING PAGES. ALL ATTEMPTS TO DATE TO OBTAIN THE MISSING PAGES HAVE BEEN UNSUCCESSFUL.

INTRODUCTION

This final report documents work performed by Computational Physics, Inc. (CPI) for the Space Science Division of the Naval Research Laboratory (NRL) in support of contract number N00014-88-C-2281. Extensive documentation has been provided throughout the contract period in the form of monthly reports, as well as more formal reports detailing the completion of key research tasks. The series of appendices contained in this report summarize the technical work performed in key research areas. In addition, the following section gives a brief summary of the general scope of the entire contract.

OVERVIEW AND SUMMARY

The work performed on this contract falls into the following general categories:

1. satellite optical instrumentation
2. analysis of optical data from satellite experiments
3. analysis of solar spectra and optical images from satellite experiments to investigate physical processes taking place in the solar atmosphere, particularly the corona and transition zone region
4. modeling of the chemistry and dynamics of the middle atmosphere
5. modeling of the Earth's dayglow, Rayleigh scattering of sunlight, nightglow, and auroral emissions
6. development of retrieval algorithms to extract O_2 and O_3 vertical concentration profiles from solar occultation data obtained by the SUSIM instrument on UARS
7. development of software for generating global images of thermospheric emissions
8. modeling of millimeter-wave emissions of the middle atmosphere and development of corresponding retrieval algorithms
9. development of a trace constituent climatology of the middle atmosphere
10. improvements to CPI's optical emissions models.

CPI's research efforts were carried out by physicists on-site at NRL and in-house at CPI's headquarters in Annandale, VA. Table 1 identifies the on-site individuals and lists any key experiments or models associated with these researchers under this contract. Similar information is provided in Table 2 for in-house work.

Table 1. On-site CPI personnel who participated in this program. The last two column are intended to provide only an indication of involvement in experimental and modeling efforts by the listed personnel over the three year life of this program.

Investigator	Research Area	Satellites or Experiments Supported by Investigator	Key Models Used, Developed, or Modified by Investigator
Ms. K. A. Abbott	Solar XUV spectroscopy	Solar XUV images - Skylab	
Dr. S. L. Berg	Optical backgrounds	MSX, VUE, IBSS	
Mr. J. S. Morrill	Dayglow	RAIDS, UVLIM, MAHRSI	PEGFAC
Mr. W. J. Sawchuck	Modeling chemistry and dynamics of the middle atmosphere	MAHRSI	KINEARTH, 2D Chemistry and Dynamics Model
Dr. A. C. Sterling	Solar physics	Solar-A	
Mr. S. E. Thonnard	Dayglow, nightglow	RAIDS, SSULI, HIRAAS	

Key to selected abbreviations

Experiments

MSX	Midcourse Space Experiment
VUE	Visible Ultraviolet Experiment
IBSS	Infrared Background Signature Survey
RAIDS	Remote Atmospheric and Ionospheric Detection System
SSULI	Special Sensor Ultraviolet Limb Imager
UVLIM	Ultraviolet Limb Imager
MAHRSI	Middle Atmosphere High Resolution Spectrographic Investigation
HIRAAS	High Resolution Airglow and Auroral Spectrograph

Models

PEGFAC	CPI/NRL dayglow model (photoelectron g-factors)
KINEARTH	NRL mesosphere/stratosphere 1D chemical/dynamics model

Table 2. In-house CPI personnel who participated in this program. The last two column are intended to provide only an indication of involvement in experimental and modeling efforts by the listed personnel over the three year life of this program.

Investigator	Research Area	Experiments Supported by Investigator	Key Models Used, Developed, or Modified by Investigator
Dr. D. E. Anderson	Aeronomy	UVPI	LOWTRAN, RAYLIMB
Mr. R. P. Barnes	Atmospheric optical emissions	MAHRSI	RAYLIMB
Dr. C.-S. Chang	Atomic physics	SUSIM, POAM	
Mr. R. J. Cox	Atmospheric optical emissions	DE-1 (UV images), UVLIM	PEGFAC, DSDA, LIMB, imaging codes
Mr. J. S. Evans	Atmospheric optical emissions	UVPI, SSULI	PEGFAC, DSDA, LIMB
Ms. D. L. Kriebel	Remote sensing of middle atmosphere	MAS, WVMS	META
Dr. J. D. Lumpe	Inversion techniques	SUSIM, POAM, MAHRSI	LOWTRAN, SOLOC, other inversion models
Dr. D. J. Strickland	Aeronomy	UVPI, SSULI, VUE	PEGFAC, DSDA, LIMB

Key to selected abbreviations not included in Table 1:

Experiments

DE-1	Dynamics Explorer-1
MAS	Millimeter-wave Atmospheric Sounder
POAM	Polar Ozone and Aerosol Measurement
SUSIM	Solar Ultraviolet Spectral Irradiance Monitor
UVPI	Ultraviolet Plume Instrument

Models

DSDA	CPI/NRL photon transport code used to calculate source functions of optically thick lines in the thermosphere and ionosphere
LIMB	CPI code used to calculate limb radiances of dayglow and nightglow emission features
RAYLIMB	CPI code which calculates limb profiles of Rayleigh scattered sunlight
LOWTRAN	AFGL transmission/Rayleigh scattering code
SOLOC	CPI code used to invert extinction profiles of full solar disk irradiance observed by the NRL experiment SUSIM onboard satellite UARS
META	CPI/NRL code which calculates microwave emissions of minor species densities in middle and lower atmosphere

In summary, this contract provided the opportunity to conduct research on several topics in the general areas of upper atmospheric physics, middle atmospheric physics, and solar physics. It also provided the opportunity to support future experimental programs within NRL's Space Physics Division such as RAIDS, SSULI, SUSIM, MAHRSI, and POAM. Support was in the form of laboratory work, data simulations, and development of algorithms for retrieving geophysical information from the listed instruments. On the SSULI task, e.g., extensive calculations of the dayglow from 834 Å to 1800 Å were made to estimate signal strengths and investigate the sensitivity of O^+ 834 Å to O^+ in the F-region. Under the SUSIM task, an entirely new retrieval algorithm was developed which performs an inversion of the occultation data to determine number density profiles in a model independent manner. In addition, a great deal of work went into the development of an accurate forward model code which has been used extensively in the pre-flight phase to generate realistic simulations of the SUSIM occultation data sets. Under the task involving remote sensing at millimeter wavelengths, the META code has developed to the point where it provides accurate simulations of the ground based millimeter wave emission measurements being performed by NRL. This is a valuable resource in terms of experiment planning and the development of retrieval schemes for this program. More detailed discussions of these tasks and others follow in the appendices.

Papers have been written which document some of the research performed in this contract. A list of these papers follows. The list also includes abstracts of presentations made at AGU meetings. Some of them also appear in the appendices.

Lumpe, J. D., C. S. Chang, and D. J. Strickland, Atmospheric Constituent Density Profiles from Full Disk Solar Occultation Experiments, *J. Quant. Spectrosc. Radiat. Transfer*, *46*, 483, 1991.

Strickland, D. J., R. J. Cox, R. P. Barnes, L. J. Paxton, R. R. Meier, and S. E. Thonnard, A Model for Generating Global Images of Emission from the Thermosphere, to be submitted to *Applied Optics*.

Evans, J. S., D. J. Strickland, D. E. Anderson, Jr., R. R. Conway, H. W. Smathers, D. F. Bakeris, R. A. Swanson, T. A. Chubb, and J. G. Cardon, UVPI Imaging from the LACE Satellite: Analysis of Broad Band UV Auroral Limb Data, to be submitted to *J. Geophys. Res.*

Morrill, J., W. Benesch, Plasma Preconditioning and the Role of Elevated Vibrational Temperatures in Production of N_2 Excited State Vibrational Distributions, *J. Geophys. Res.*, *95*, 7711, 1990.

Carragher, B. A., J. Morrill, W. M. Benesch, Gas Phase Molecular Energy Transfer Studies via Time-Resolved Spectroscopy, *J. Optic. Soc. Am.*, *8*, 123, 1991.

Morrill, J., W. Benesch, and K. Widing, Electron Temperatures in a Pulsed Electric Discharge in N_2 and the Associated Electron Excitation Rate Coefficients, *J. Chem. Phys.*, *94*, 262, 1991.

Morrill, J., R. P. McCoy, and C. Meng, Diurnal Variation of Thermospheric Odd Nitrogen Observed from Low Earth Orbit, *EOS, Trans. Amer. Geophys. Union, 70(44)*, 1236, 1989.

Morrill, J., D. Prinz, and R. McCoy, The Performance of the MUV and NUV Instruments in the RAIDS Experiment, *EOS, Trans. Amer. Geophys. Union, 71(44)*, 1486, 1990.

Fritz, G. G., D. K. Prinz, R. P. McCoy, R. R. Meier, and J. S. Morrill, A Far-Ultraviolet Imaging Spectrograph for RAIDS, *EOS, Trans. Amer. Geophys. Union, 71(44)*, 1486 1990.

Newburn, D. R. Goodel, J. Morrill, and W. Benesch, Afterglow Emission of Auroral Molecular Nitrogen Bands, *EOS, Trans. Amer. Geophys. Union, 71(16)*, 213, 1991.

APPENDIX 1

UVPI IMAGING OF AURORAL LIMB DATA

Contributors:

J. S. Evans
D. J. Strickland
D. E. Anderson, Jr.

UVPI Imaging from the LACE Satellite: Analysis of Broad Band UV Auroral Limb Data

J. S. Evans
D. J. Strickland
D. E. Anderson, Jr.[†]

Computational Physics, Inc.
2750 Prosperity Avenue, Ste. 600
Fairfax, VA 22031

R. R. Conway
H. W. Smathers

Naval Research Laboratory
Washington, DC 20375

D. F. Bakeris
R. A. Swanson
T. A. Chubb

AlliedSignal Technical Services Inc.
Alexandria, VA 22314

J. G. Cardon[‡]

Applied Coherent Technology Corp.
Reston, VA 22091

[†] Now at Applied Physics Laboratory, The Johns Hopkins University, Laurel, MD 20723
[‡] Now at Computational Physics, Inc.

ABSTRACT

Southern auroral limb images have been recorded by the wide angle UV camera within the UltraViolet Plume Instrument (UVPI) onboard the Low-power Atmospheric Compensation Experiment (LACE) satellite. Tangent altitudes within each image have been determined using recorded stars along with the known position of the satellite. Range to the observed aurora has been determined by stereoscopic techniques using images of the same auroral forms collected over several seconds. An auroral model has been used to fit two limb profiles taken from the same image. The parameters varied within the model to achieve the given fits are 1) number of auroral forms within the observing region, 2) their locations, 3) thicknesses, and 4) spectral characteristics of the precipitating electron spectra. The model provides altitude profiles of volume emission for the relevant features based on electron transport calculations starting with a user specified precipitating electron spectrum. Volume emission for multiple precipitation patterns is then distributed within the observing region followed by line-of-sight integrations producing limb profiles. Excellent fits to the entire observed profiles were obtained using a combination of diffuse aurora and a single discrete aurora placed near the tangent point. The fitting process suggests that a good quantitative description of the aurora has been achieved in terms of precipitating electron spectral characteristics and spatial distribution of this precipitation.

1. INTRODUCTION

The subject of this paper is interpretation of a sequence of UV images acquired during a limb scan of a southern aurora by the UVPI (UltraViolet Plume Instrument) experiment on satellite LACE (Low-power Atmospheric Compensation Experiment). Spatial and energy characteristics of electron precipitation in the observed aurora are inferred from a detailed fitting of calculated broad band UV limb profiles to the data. To our knowledge, this is the first paper to address satellite observed aurora on the limb in a quantitative fashion without the use of tomographic inversion or algebraic reconstruction techniques (see e.g., Solomon et al., 1984, Solomon et al., 1985, McDade and Llewellyn, 1991, and references therein). Past satellite UV imaging experiments have obtained auroral images containing mostly disk emission. Any auroral limb data currently available have either been on much coarser tangent altitude scales or were measured tomographically (i.e. limb scans through one or more emitting regions observed from different locations). Satellite observations include those from Dynamics Explorer [Frank and Craven, 1988], Viking [Anger et al., 1987], HILAT [Meng and Huffman, 1984], and PolarBEAR [Schenkel et al., 1986] (also see Solomon et al., 1988, Solomon, 1989, McDade et al., 1991, Swenson et al., 1990).

Our interest is to understand the spectral content of the auroral emission being observed and to investigate how well spatial and energy characteristics of the aurora can be inferred from single scan limb observations. Four characteristics of the aurora determine its variation in luminosity with tangent altitude. They are 1) number of forms along the line-of-sight, 2) their locations, 3) their horizontal extents, and 4) hardnesses and energy content of the incident electron spectra. We will quantitatively address the relationship between luminosity variations across the limb and these properties using the auroral model of Strickland et al. [1976] (also see Strickland et al., 1983, Strickland et al., 1989, Basu et al., 1993, and Strickland et al., 1993). The model is then used to fit two limb profiles taken from a single tracker camera image. As will be shown, this requires a minimum of two auroral forms along the line-of-sight. While the above inferred properties are not unique, we believe that the four parameters identified above can be sufficiently restricted to provide quantitative information on spatial and energy characteristics of the aurora.

2. THE LACE SATELLITE

The LACE satellite was designed and built by the Naval Research Laboratory (NRL) for the Strategic Defense Initiative Organization. The satellite's primary mission was to provide a sensing array in orbit for evaluating the effect of active compensation of a ground based laser system on light propagated through the atmosphere. On February 14, 1990, the LACE satellite was launched into a circular orbit of 540 km with an inclination of 43°. The LACE spacecraft was designed to operate the primary experiment for a 30 month lifetime. It is a gravity-gradient stabilized satellite with attitude measurement accuracy better than 1°. To support the LACE spacecraft, there were three ground stations operated by NRL, one permanent and two transportable. LACE was decommissioned on February 14, 1993.

The UVPI was a pointable, telescopic instrument mounted on the Earth facing side of the LACE spacecraft. Its mission was to collect images of rocket plumes in the near- and mid-ultraviolet regimes from a space based platform. It was also used to collect background image data of the Earth, Earth's limb, and celestial objects. Background imaging performed by UVPI included the day, night, and dawn limb, aurora, sunlit and moonlit clouds, and the Earth's hardbody.

The UVPI consisted of two intensified CCD cameras that were boresighted and shared a Maksutov-Cassegrain telescope. The tracker camera was sensitive in the near-ultraviolet/visible wavelength region, had a 15 times larger field-of-view than the plume camera, and was used to locate, acquire, and track a target. The plume camera collected images at near- and mid-ultraviolet wavelengths selectable with a filter wheel. Fig. 1 shows a schematic of the intensified camera. Table 1 lists characteristics of the optics and each camera. The camera images were digitized and transmitted to the ground or were recorded onboard for later transmission.

The optics for both camera systems are shown in Fig. 2. The UVPI was mounted within the satellite and looked through an aperture in the Earth oriented end panel. By use of a gimballed mirror the UVPI had a field of regard of a 50° half-angle cone about the satellite's nadir. When not in use, a door covered the UVPI aperture. Attached to the inside of this door

was a flat mirror which, when the door was opened part way, allowed the UVPI cameras to view celestial objects or the Earth's limb. Because of the hinge arrangement of the calibration door, limb viewing was only possible out the right side of the spacecraft, which was due south when the spacecraft was moving due east at 43° south or north latitude. No viewing of the northern aurora was possible.

The images analyzed in this paper were acquired at a rate of 5 s^{-1}. The camera output was an analog signal read from a CCD chip as a sequence of interlaced image fields. The analog signal was immediately digitized to produce a shifted (temporally delayed) image field once every 1/60 s. Pairs of interlaced field readouts were summed to provide a full digitized image frame once every 1/30 s. In normal mode, every sixth frame was sent to the ground in real-time, or was sent to a tape recorder and subsequently transmitted to a ground station. Each image consists of an array of 251 x 240 8-bit numbers that measures the flux distribution on the CCD sensor plane.

The photometric range and sensitivity of the UVPI cameras were optimized for nighttime operations. That is, the instrument was designed to view and track relatively bright targets against a dark background. The UVPI tracker camera could image stars as dim as visual magnitude 7. The plume camera had a commandable filter wheel allowing selection from four filters of varying passbands. The relative spectral responsivity was determined from transmission and reflectivity measurements of the optical components of the system and measurement of the photoelectric efficiency of the image intensifier photocathode. The absolute responsivity of the system was determined from post-launch observations of stars. The average deviation in the ratio of observed to calculated star responses was about 10-15 percent in the plume camera, and about 16 percent in the tracker camera. Reynolds et al., [1989] give a more complete description of the UVPI and its requirements.

On-orbit calibration was accomplished by observing and actively tracking stars with a known spectrum. Calibration star measurements were made frequently, about four to eight times a month, mostly to support UVPI's primary mission and to collect UV spectral data on stars. Smathers et al., [1989] gives a description of pre-launch calibration and performance. The data

presented in this paper come from the tracker camera over the wavelength interval from 250 to 450 nm. For these data, the tracker camera was not centered on the observed auroral forms; thus the plume camera did not record them.

3. OBSERVING CONDITIONS

The images of interest were recorded during orbit 2570 on August 3, 1990 while viewing the southern aurora in the morning sector at approximately 17:20 GMT. The spacecraft was in darkness over the entire viewing period which provided optimum efficiency of the CCD cameras and associated optics. The observed aurora was also in darkness. The K_p index was 3 which reflects moderate geomagnetic activity. The spacecraft was near the southernmost point of the orbit (43.1° latitude, 110° E longitude) off the southern coast of Australia. Viewing was to the south and for the data of interest, the horizontal center line of the image occurred at about 100 km tangent altitude with a corresponding slant range of 2475 km where the spatial coverage of the tracker camera was 374 km x 491 km (vertical by horizontal). Several auroral forms are present in the data collected. Some 300 frames were recorded by the tracker camera during an observation period of 100 s. Plate 1 shows a composite of selected overlapping frames from which the data to be presented in Section 6 were taken.

4. TANGENT ALTITUDE AND RANGE DETERMINATIONS

The apparent height of the aurora above the limb was determined from the apparent height of a background star observed in the same images, using the star coordinates and the orbital elements of the spacecraft (s/c). Auroral range was determined from the apparent backward motion of the aurora (v_{aur}). This motion results primarily from the forward orbital velocity but is also affected by rotation of the spacecraft (one rotation per orbit) and rotation of the Earth. Assuming a stationary aurora, v_{aur} is given by

$$v_{aur} = -v_{s/c} + \omega_{s/c} \times r_{LOS} + \Omega_E \times R_{aur} \cdot u_r \qquad (1)$$

where $v_{s/c}$ is the orbital velocity, $\omega_{s/c} = R_{s/c} \times v_{s/c}$ is the angular velocity of the spacecraft in its orbit, r_{LOS} is the line-of-sight vector from the spacecraft to the aurora, R_{aur} and $R_{s/c}$ are vectors from Earth center to the aurora and the s/c respectively, Ω_E is the angular velocity of Earth, and u_v is the unit vector $v_{s/c} / |v_{s/c}|$. Solving for the range r_{los}

$$r_{LOS} = \frac{v_{aur} + v_{s/c} - \Omega_E R_{aur} \cos(L_{aur}) \cos(\delta)}{\omega_{s/c} \sin(\alpha)} \qquad (2)$$

where α is the depression angle of r_{LOS}, L_{aur} is the latitude of the aurora, and δ is the angle between $v_{s/c}$ and due East. For the data of interest here, the contributions to apparent auroral velocity were $v_{s/c}$ = -7.204 km/s, $|\omega_{s/c} \times r_{los}|$ = 0.992 km/s, and $|\Omega_E \times R_{aur} \cdot u_v|$ = 0.229 km/s. The range to the aurora seen near a tangent altitude of 110 km was r_{los} = 2475 km.

5. MODELLING OF AURORAL EMISSION IN A LIMB VIEWING GEOMETRY

We use the electron transport model of Strickland et al. [1976] generalized to three neutral density constituents for calculating the electron flux $\phi(z,E,\mu)$ in $e^- cm^{-2} s^{-1} eV^{-1} sr^{-1}$ starting with a precipitating electron spectrum $\phi_o(E,\mu)$ in the same units. The independent variables are altitude z in km, energy E in eV, and cosine of the pitch angle μ. Maxwellian and Gaussian distributions isotropic over the downward hemisphere have been used to characterize ϕ_o in this work. We use Gaussian distributions to describe the precipitating electron spectrum for the discrete aurora and either Gaussian or Maxwellian distributions to describe electron spectrum for the diffuse aurora. High and low energy tails are included as given in Strickland et al. [1993]. For either representation, the key parameters are energy flux Q in ergs $cm^{-2}s^{-1}$ and characteristic energy E_o. For Maxwellians, E_o is half the mean energy while for Gaussians, it refers to the energy of the Gaussian peak. The approximate range of E_o for diffuse aurora is 0.5 to 3 keV. For discrete aurora, a few keV to about 10 keV is common.

From $\phi(z,E,\mu)$, we calculate volume excitation and ionization rates with the appropriate cross sections for use in chemistry modeling and in specifying emission rates. Examples of

excitation and ionization rates for a variety of ϕ_o's may be seen in Strickland et al. [1989]. Figure 3 shows emission rates for lines and band systems within the wavelength interval of interest here (180 - 450 nm). A Gaussian distribution as described above with Q = 10 ergs $cm^{-2}s^{-1}$ and E_o = 5 keV was used to characterize the precipitating electron spectrum. The emission features include the atomic lines OI 297.2 nm and NI 346.6 nm and bands of the following molecular systems: N_2 LBH, N_2 VK, N_2 2PG, N_2^+ 1NG, O_2 Herzberg I and II, and O_2 Chamberlain. The O_2 volume emission rate profile does not include nightglow. A nightglow component will be included when comparing with UVPI data. The emission at 346.6 nm arises from dissociative excitation of N_2. Quenching is responsible for the slower altitude variation of the N_2 VK and OI 297.2 nm profiles.

Figure 4 illustrates the spectral characteristics of limb emission from N_2 LBH, N_2 VK, N_2 2PG, and N_2^+ 1NG. The incident electron spectrum is the same as used to generate the volume emission rates in Figure 3. The arc thickness is 100 km with a position of -1000 km. The tangent altitude is -25 km.

Figure 5 shows a sketch illustrating how slant intensities for various auroral forms were computed. The narrow shaded region represents a discrete arc at the tangent point while the wide shaded region represents diffuse aurora between the tangent point and the spacecraft. We assume a given thickness for an arc such as 100 km and assume the precipitating electron spectrum to be the same over this thickness. The arc is then placed at some position along the line-of-sight as shown in the figure. The emitting layer shown in Figure 5 is meant to represent the vertical extent of the auroral arcs. The emitting region generally begins around 80 km and ends at about 300 km with peak intensities occurring in the vicinity of 110 km. The arc position is referenced to the tangent point. For example, a distance of -500 km would refer to an arc whose center is 500 km from the tangent point in the direction of the observer.

Figure 6 provides examples of limb intensity profiles of the N_2^+ 1NG system in Rayleighs for a 100 km thick arc placed at the following locations: -1000, -500, 0, and 500 km. The incident electron spectrum is the same one used to generate the results in Figures 3 and 4. As expected, the profile for the arc at the tangent point peaks at a higher tangent altitude than those

in the near- and far-field. Its maximum value occurs at 115 km which is close to the altitude of maximum volume emission. The +1000 km profile has the sharpest fall off on its bottom side due to geometry considerations. Attenuation along the line-of-sight was not taken into account in the calculations. It is not important for the given system except possibly at tangent altitudes well below 100 km for arcs on the far side of the tangent point. In this case, Rayleigh scattering will reduce the intensity on the bottom side of the profiles but not enough to significantly change their shapes. For emission below 300 nm (see Figure 4), an additional source of attenuation is ozone. Again, it is not important except for emission originating on the far side of the tangent point and being recorded at tangent altitudes well below 100 km. For the data to follow, we will argue that most of the recorded emission at small tangent altitudes comes from the near side of the tangent point and thus experiences little or no attenuation by either absorption or scattering.

Figure 7 shows the sensitivity of limb intensities to E_o using Gaussian distributions with tails and for a Q value of 10 ergs cm^{-2} s^{-1}. The arc has a thickness of 100 km with its center located at the tangent point. As in Figure 6, we have selected the N_2^+ 1NG system for displaying the results. The same variation versus E_o as well as versus arc location (previous figure) occurs for any other emission feature within the 180 to 450 nm region. A comparison of Figure 5 and Figure 6 shows that changes in arc location mimic changes in E_o. As an arc moves away from the tangent point, the limb intensity profile peak decreases in tangent altitude as if an increase in E_o had occurred. Unlike the latter case, however, the tangent altitude of the peak can decrease to values considerably below 100 km which, if interpreted in terms of E_o, would lead to unrealistically large values in this parameter. It is important to be able to distinguish between changes in the limb intensity profile due to changes in arc position versus changes in E_o. Otherwise, unique information on the spatial distribution of emission and characteristics of the associated precipitation cannot be obtained from limb intensity profiles. In the next section, we will argue that it is possible to distinguish between these two effects using limb data that provide a well defined shape to the limb intensity profile. Support for this argument comes from Figures 6 and 7 where it is seen that considerably more change in *shape* (ignoring where the tangent altitude of the peak occurs) occurs as E_o changes compared to changes in arc location.

6. FITTING MODEL LIMB PROFILES TO THE DATA

The shape of an auroral limb profile is a function of the number of auroral forms along the line-of-sight and individual characteristics of these forms. These characteristics fall into spatial and spectral categories. Within the spatial category are thickness and location. Within the spectral category are Q, E_o, and the type of distribution (Maxwellian or Gaussian in this work). This totals to six parameters/descriptions which raises the question of uniqueness when a good fit to the data is achieved. We will not address this issue in any detail here but will show that real constraints can be placed on their inferred values through observing the quality of fit as these parameters/descriptions are changed. An example of one condition imposed by the given data is that at least two auroral forms are required to fit the data. A good fit could not be achieved using one auroral structure regardless of its spatial and spectral characteristics. More will be said about this below. Limb profile shape is most sensitive to the location of the auroral form and to E_o. The degree of sensitivity was illustrated in Figures 6 and 7 as discussed in the previous section. Sensitivity to the remaining parameters/descriptions is less important but all parameters were varied during the data fits to be discussed next.

Figure 8 shows the best fits to two data sets taken from the same tracker camera image. As noted in Section 2, the data were collected on pass 2570 looking south at the southern nighttime aurora on August 3, 1990 (see plate 1). The error bars shown with the data represent ± 1 standard deviation (assuming Poisson statistics). We will refer to the data in the upper (lower) panel as Set #1 (Set #2) data. The two measured profiles possess similar peaks and topside scale heights. The bottomsides, however, are different and will be further discussed below. The model profiles each comprise a nightglow (O_2 Herzberg I, II and Chamberlain band systems) and two auroral components. The nightglow component used in this analysis is based on the work of Stegman and Murtagh [1991] and is consistent with the results obtained therein. For the brightness of the given aurora, the nightglow component is unimportant.

As mentioned above, a good fit could not be achieved with a single auroral form. Excellent fits were achievable, however, by introducing two auroral forms, one near the tangent point and the other in front of it. Table 2 provides details by identifying the six

parameters/conditions discussed above. The inferred location of the auroral forms provided in Table 2 refer to distance from the tangent point towards the observer. The included error estimates are acceptable deviations from the inferred values and reflect the sensitivity analysis performed on the data. For values outside these deviations, the fits to the data become degraded. It should be noted that any errors in calibration are directly reflected in the magnitudes of the Q values.

For either data set, an arc at the tangent point is needed to fit the peak region. The inferred thickness is 300 km and suggests a discrete aurora. A second auroral structure in front of the tangent point is required to fit the topside and bottomside. If placed behind the tangent point, a fit to the bottomside cannot be achieved. The inferred thickness is approximately 1000 km for either data set and suggests diffuse aurora. The inferred E_o's for the second auroral structure are typical hardnesses of a diffuse aurora. The difference in bottomsides of the two data sets is due to differences in the diffuse aurora in front of the tangent point. To achieve the greater falloff in Set 2, a somewhat narrower diffuse region closer to the observation point was needed as quantified in Table 2.

7. DISCUSSION AND CONCLUSIONS

A detailed analysis of single scan satellite observed auroral limb emission in terms of structure and spectral characteristics has not been performed before. A general impression within the field has been that little useful quantitative information comes from such data given the general lack of knowledge about structure along the line-of-sight. This analysis suggests that an accurate measurement of limb emission from, say, 0 to 200 km in tangent altitude allows one to reasonably specify the gross structural characteristics of the emission. For example, it seems clear from this analysis that two structured forms with the characteristics given in Table 2 produced the observed limb profiles. It then follows that one can also infer spectral characteristics of the precipitating electrons as was done here. The shortcoming of the present results is that we did not apply an error propagation model to produce good quantitative error bars which would address the issue of uniqueness. A first step was made in the form of a

sensitivity study in which the quality of fit was monitored as parameter values were varied. The next step is to perform similar analyses of limb data for other auroras exhibiting distinctly different spatial and/or spectral characteristics. This will provide more information on constraints imposed by the fitting process. Independent information on spatial structure from ground based or space based imagery would also be useful.

In conclusion, we believe that Table 2 provides a good overall description of the aurora producing the data in Sets 1 and 2 based on our detailed examination of fitting errors as the parameters listed in Table 2 were varied.

ACKNOWLEDGEMENTS

The authors would like to thank Don Horan for many useful discussions. This work was supported by SDIO through the Naval Research Laboratory.

REFERENCES

Anger, C. D., et al., Scientific Results from the Viking ultraviolet Imager: an introduction, *Geophys. Res. Lett.*, *14*, 383, 1987.

Basu, B., J. R. Jasperse, D. J. Strickland, and R. E. Daniell, Jr., Transport-Theoretic Model for the Electron-Proton-Hydrogen Atom Aurora: 1. Theory, accepted for publication in *J. Geophys. Res.*, 1993.

Frank, L. A., and J. D. Craven, Imaging results from Dynamics Explorer I, *Rev. Geophys.*, *26*, 249, 1988.

McDade, I. C., N. D. Lloyd and E. J. Llewellyn, A rocket tomography measurement of the N_2^+ 3914 Å emission rate within an auroral arc, *Planet. Space Sci.*, *39*, 895, 1991.

McDade, I. C., and E. J. Llewellyn, Inversion techniques for recovering two-dimensional distributions of auroral emission rates from tomographic rocket photometer measurements, *Can. J. Phys.*, , , 1991.

Meng, C.-I., and R. E. Huffman, Ultraviolet imaging from space of the aurora under full sunlight, *Geophys. Res. Lett.*, *11*, 315, 1984.

Packer, D. M. and I. G. Packer, Exploring the Earth's atmosphere by photography from Skylab, *Appl. Opt.*, *16*, 983-992, 1977.

Reynolds, L. H., H. W. Ramsey, H. D. Wolpert, H. W. Smathers, and D. M. Horan, Design and description of the Ultraviolet Plume Instrument (UVPI), in *Proc. SPIE Ultraviolet Technology III*, *1158*, 196, 1989.

Schenkel, F. W., B. S. Ogorzalek, R. R. Gardner, R. A. Hutchins, R. E. Huffman, and J. C. Larrabee, Simultaneous multi-spectral narrow band auroral imagery from space (1150 Å to 6300

Å), *Proc. SPIE Ultraviolet Technology, 687*, 1986.

Smathers, H. W., G. R. Carruthers, H. W. Ramsey, G. Steiner, W. Louissant, Calibration and performance of the Ultraviolet Plume Instrument (UVPI), *Proc. SPIE Ultraviolet Technology III, 1158*, 212, 1989.

Solomon, S. C., P. B. Hays and V. J. Abreu, Tomographic inversion of satellite photometry, *Appl. Opt., 23*, 3409, 1984.

Solomon, S. C., P. B. Hays and V. J. Abreu, Tomographic inversion of satellite photometry. Part 2, *Appl. Opt., 24*, 4134, 1985.

Solomon, S. C., P. B. Hays and V. J. Abreu, The auroral 6300 Å emission: observations and modelling, *J. Geophys. Res., 93*, 9867, 1988.

Solomon, S. C., Auroral excitation of the N_2 2P(0,0) and VK(0,9) bands, *J. Geophys. Res., 94*, 17215, 1989.

Stegman, J. and D. P. Murtagh, The Molecular Oxygen Band Systems in the U.V. Nightglow: Measured and Modelled, *Planet Space Sci., 39*, No. 4, 595-609, 1991.

Strickland, D. J., D. L. Book, T. P. Coffey and J. A. Fedder, Transport Equation Techniques for the Deposition of Auroral Electrons, *J. Geophys. Res., 81*, 2755, 1976.

Strickland, D. J., J. R. Jasperse and J. A. Whalen, Dependence of Auroral FUV Emission on the Incident Electron Spectrum and Neutral Atmosphere, *J. Geophys. Res., 88*, 8051, 1983.

Strickland, D. J., R. R. Meier, J. H. Hecht and A. B. Christensen, Deducing Composition and Incident Electron Spectra from Ground-Based Auroral Optical Measurements: Theory and Model Results, *J. Geophys. Res., 94*, 13527, 1989.

Strickland, D. J., R. E. Daniell, J. R. Jasperse, and B. Basu, Transport-Theoretic Model for the Electron-Proton-Hydrogen Atom Aurora: 1. Theory, accepted for publication in *J. Geophys. Res.*, 1993.

Swenson, G. R., S. B. Mende, and E. J. Llewellyn, Imaging observations of lower thermospheric O(^{1}S) and 2° airglow emissions from STS 9: Implications of height variations, *J. Geophys. Res.*, *94*, 1417-1429, 1989.

Swenson, G. R., S. B. Mende, and E. J. Llewellyn, Observations of a proton aurora from the space shuttle, *Eos Transactions, American Geophysical Union*, *71*, 1488, 1990.

PLATES

Plate 1. Tracker camera composite limb image of the southern aurora taken from ~17:20 to 17:22 GMT on August 3, 1990. The horizontal center line of the image corresponds to a tangent altitude of ~100 km. The white dots show the centers of the individual frames used to make the composite. Where two frames overlap, data are taken from the most recently recorded frame. The frame centers are connected to emphasize the motion of the cameras (tracker and plume). The vertical motion is produced by a moving mirror while that in the horizontal direction is produced by the motion of the satellite. The data to be analyzed were taken from two vertical cuts through the image. Data set 1 (set 2) contains limb emission from the brightest region of the structure on the left (right).

FIGURES

Figure 1. Schematic diagram of the CCD cameras of the Ultraviolet Plume Instrument.

Figure 2. Diagram of the shared optics of UVPI including Maksutov-Cassegrain telescope.

Figure 3. Volume emission rates of the key features contributing to the spectral region from 180 to 450 nm. The applied incident electron spectrum is a Gaussian distribution with low and high energy tails having Q and E_o values of 10 ergs cm^{-2} s^{-1} and 5 keV, respectively. The profile labeled "HBRG" gives emission from the O_2 Herzberg I, Herzberg II, and Chamberlain systems by electron impact.

Figure 4. Spectra for individual band systems in Rayleighs/nm seen at a tangent altitude of -25 km from 180 to 450 nm. The arc used to generate these results is at -1000 km and has a thickness of 100 km. The O_2 Herzberg I, Herzberg II, and Chamberlain band systems are not displayed for lack of synthetic spectral models at this time. Their total emission, however, is included in the figure.

Figure 5. Schematic diagram for illustrating how auroral structure is treated in the calculations.

Figure 6. Limb intensity profiles of N_2^+ 1NG emission for a 100 km thick arc at four locations along the line-of-sight. The locations are relative to the tangent point. The incident electron spectrum is the same used to generate the results in Figure 3. The observation altitude is 500 km.

Figure 7. Limb intensity profiles of N_2^+ 1NG emission versus E_o for Gaussian distributions with tails. The energy flux Q = 10 ergs $cm^{-2}s^{-1}$. The arc is centered at the tangent point with a thickness of 100 km. The observation altitude is 500 km.

Figure 8. Fits to two auroral limb profiles taken from a single UVPI tracker camera image. Each of the two calculated profiles is composed of the three components displayed in the figure. For the given brightness of this aurora, the nightglow component is unimportant. The observation altitude is 535 km.

Tables

Table 1. UVPI tracker and plume camera characteristics and performance.

Parameter	Plume Camera	Tracker Camera
Spectral region	195-350 nm	255-450 nm
Number of filters	4	1
Time for filter change	1.7 sec	n/a
Frame rate, normal	5 per sec	5 per sec
Frame rate, zoom*	30 per sec	30 per sec
Super pixels, normal	251 x 240	251 x 240
Super pixels, zoom*	91 x 112	91 x 112
Digitization	8 bits/pixel	8 bits/pixel
Image data rate	2.5 MB/sec	2.5 MB/sec
Field of view	0.184 x 0.137 deg	2.60 x 1.98 deg
Field of regard	100 x 97 deg	100 x 97 deg
Pixel field of view	12.8 x 10.0 μR	181 x 143.9 μR
System resolution	80 - 100 μR	220 - 250 μR
Pixel exposure time	33 ms	≤33 ms (adjustable)
Frames integrated	1 - 6	n/a
Telescope aperture	10 cm	10 cm

*reduced field of view

Table 2. Parameters used to fit the data in Figure 8. M/G in the third column refers to Maxwellian or Gaussian distributions.

Data Set	Auroral Structure	ϕ_o (M/G)	E_o (keV)	Q (ergs cm^{-2} s^{-1})	Thickness (km)	Location (km)
#1	#1	G	4.5 ± .5	8.2 ± 2.5	300 ± 100	0 ± 50
#1	#2	G	2.2 ± .3	3.8 ± 1.3	1 100 ± 250	-550 ± 50
#2	#1	G	7.0 ± 1	4.2 ± 1.4	300 ± 100	0 ± 50
#2	#2	M	1.0 ± .5	5.7 ± 1.8	950 ± 250	-350 ± 50

Plate 1.

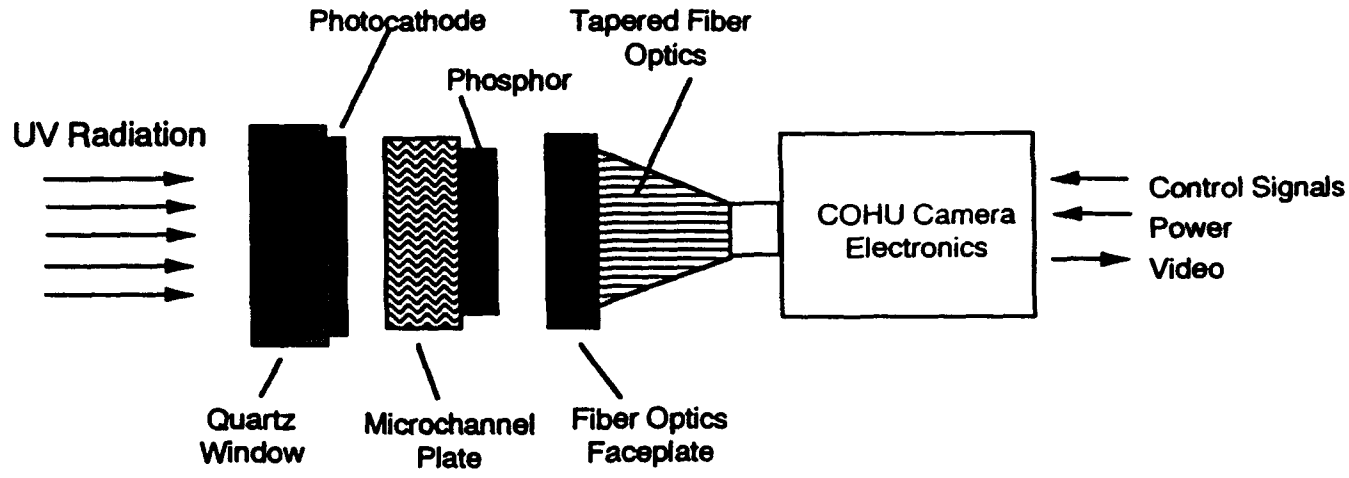

ITT Image Intensified

- ° Photocathode
  - CsTe (Plume) - 25 mm Dia.
  - BiAlkali (Track) - 40 mm Dia.
- °Microchannel Plate
  - 2 Stage (Plume)
  - 2 Stage (Track)
- ° P 20 Phosphor Output

COHU Camera Characteristics

- ° RS-170 Output - 30 Frames/sec.
- ° 754 Pixel x 240 Line Array. [TI 241 Chip set].
- ° Array Has 11 mm Diagonal.

Control - Telemetry

- ° MCP Gain.
- ° Camera Temperature.

Figure 1.

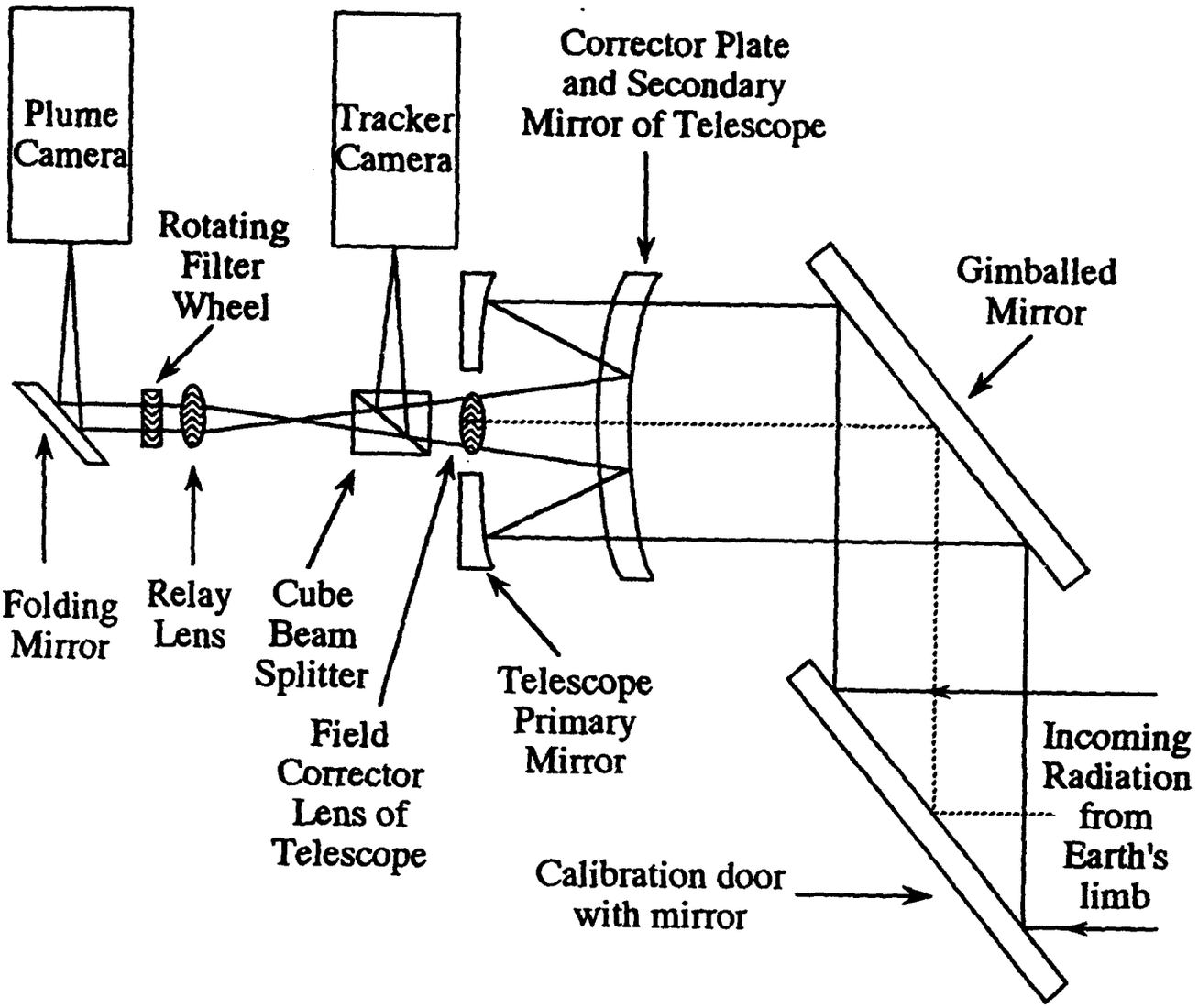
Plume Camera
Tracker Camera
Corrector Plate and Secondary Mirror of Telescope
Rotating Filter Wheel
Gimballed Mirror
Folding Mirror
Relay Lens
Cube Beam Splitter
Field Corrector Lens of Telescope
Telescope Primary Mirror
Incoming Radiation from Earth's limb
Calibration door with mirror

Figure 2.

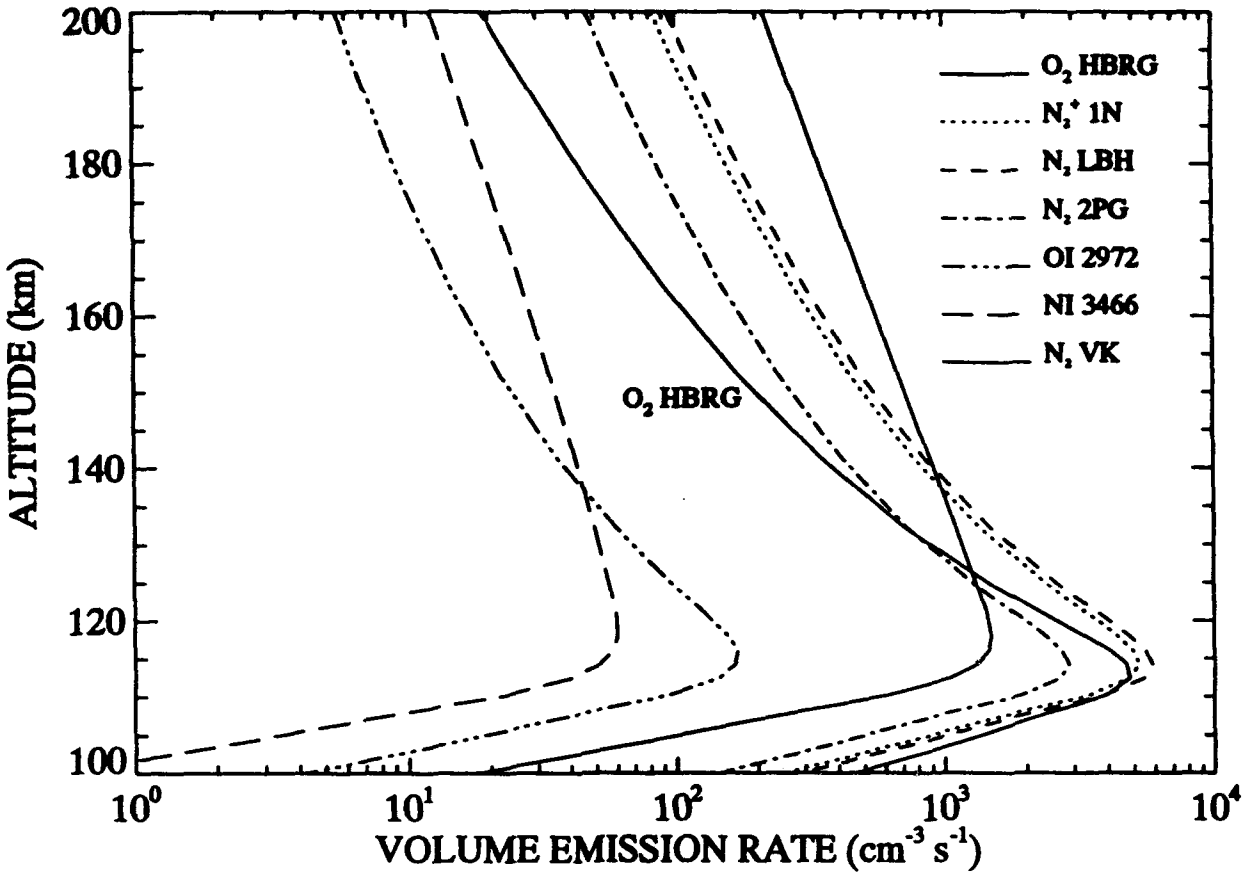
200
180
160
140
120
100
ALTITUDE (km)
10^0
10^1
10^2
10^3
10^4
VOLUME EMISSION RATE (cm^{-3} s^{-1})
O_2 HBRG
N_2^+ 1N
N, LBH
N, 2PG
OI 2972
NI 3466
N, VK
O_2 HBRG

Figure 3.

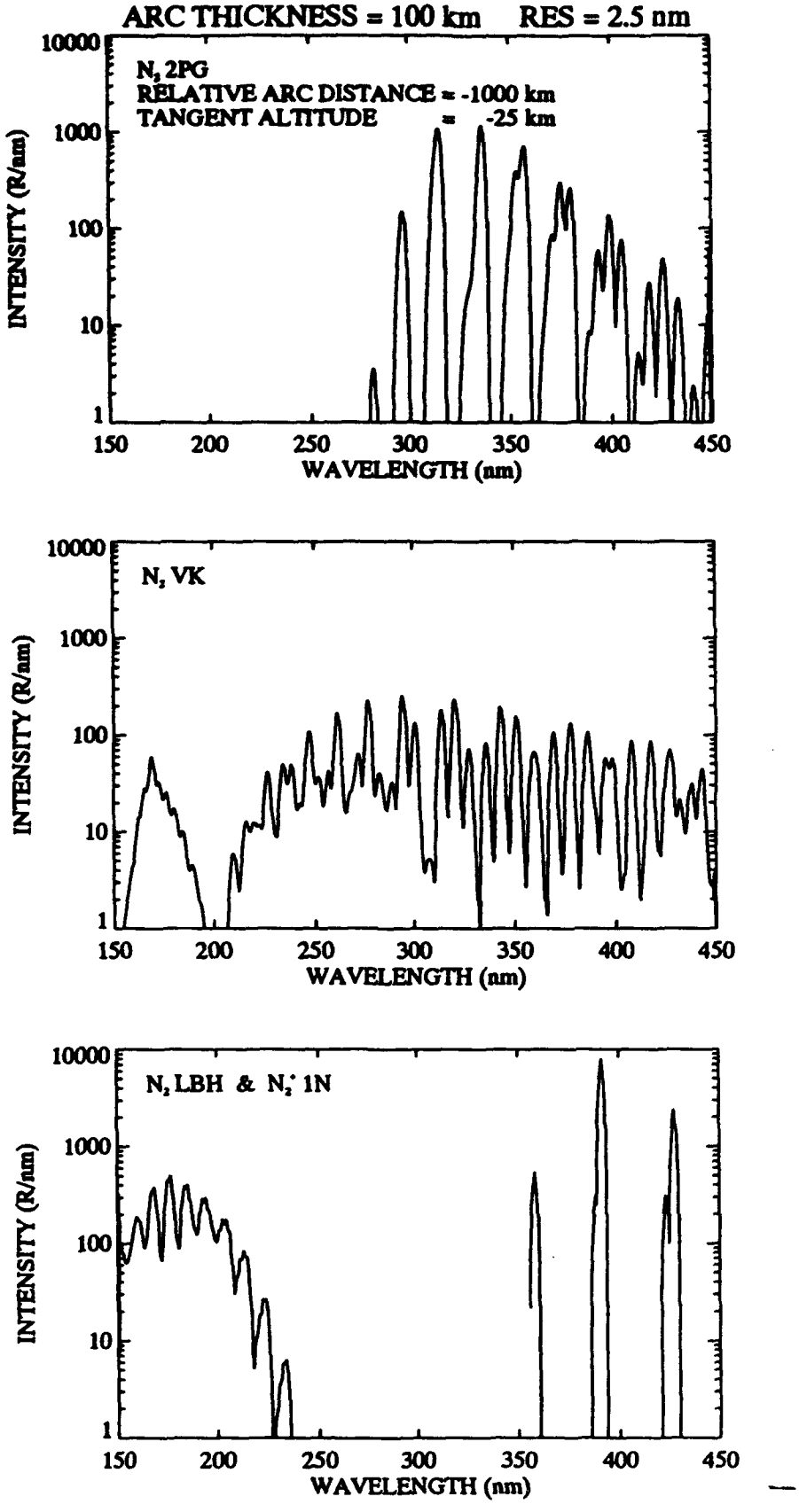
ARC THICKNESS = 100 km RES = 2.5 nm
N2 2PG
RELATIVE ARC DISTANCE = -1000 km
TANGENT ALTITUDE = -25 km
INTENSITY (R/nm)
WAVELENGTH (nm)
N2 VK
INTENSITY (R/nm)
WAVELENGTH (nm)
N2 LBH & N2+ 1N
INTENSITY (R/nm)
WAVELENGTH (nm)

Figure 4.

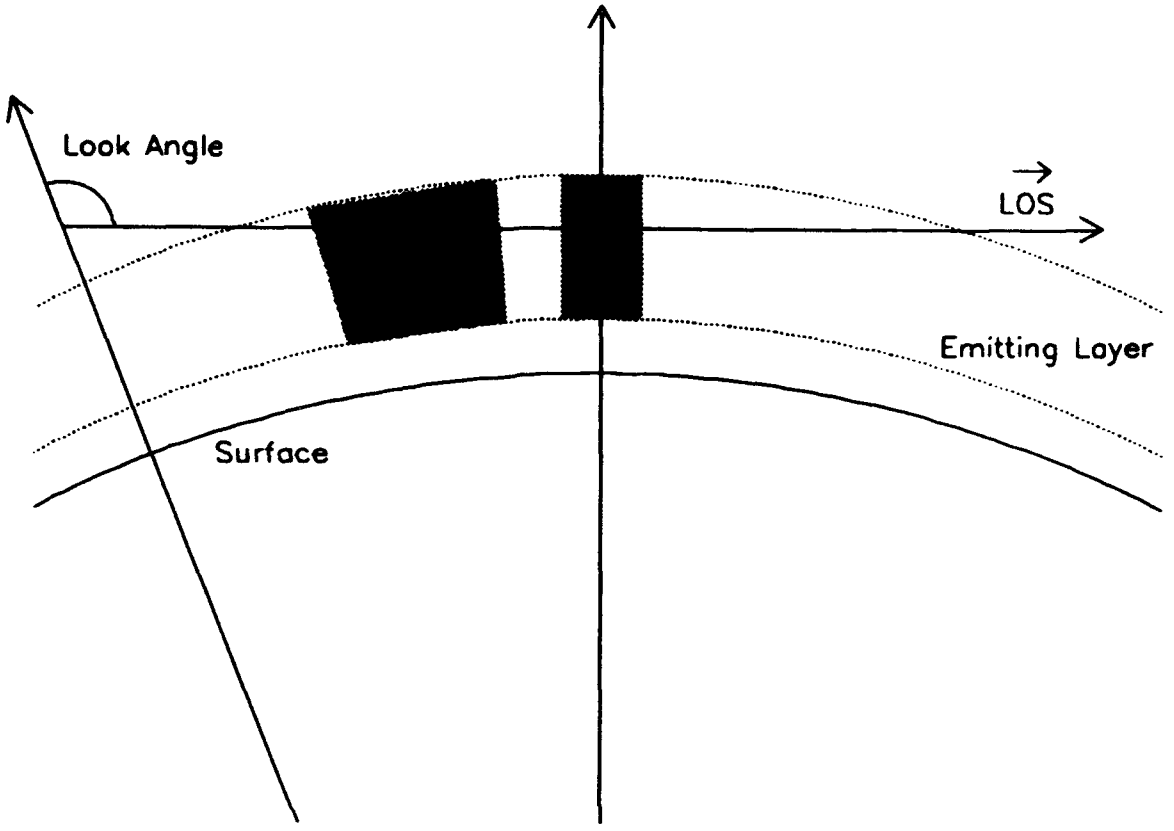

Figure 5.

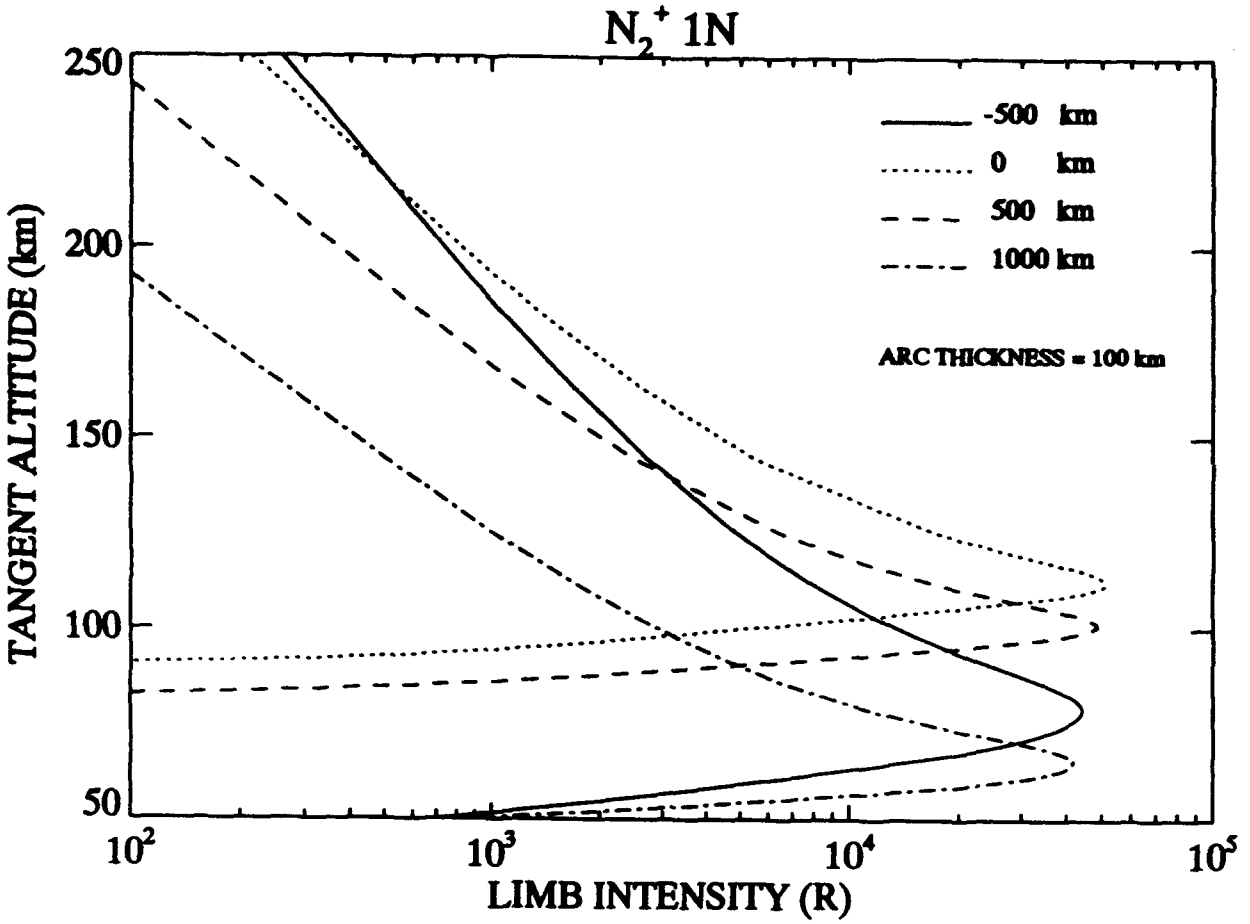
N_2^+ 1N
250
200
150
100
50
TANGENT ALTITUDE (km)
-500 km
0 km
500 km
1000 km
ARC THICKNESS = 100 km
10^2
10^3
10^4
10^5
LIMB INTENSITY (R)

Figure 6.

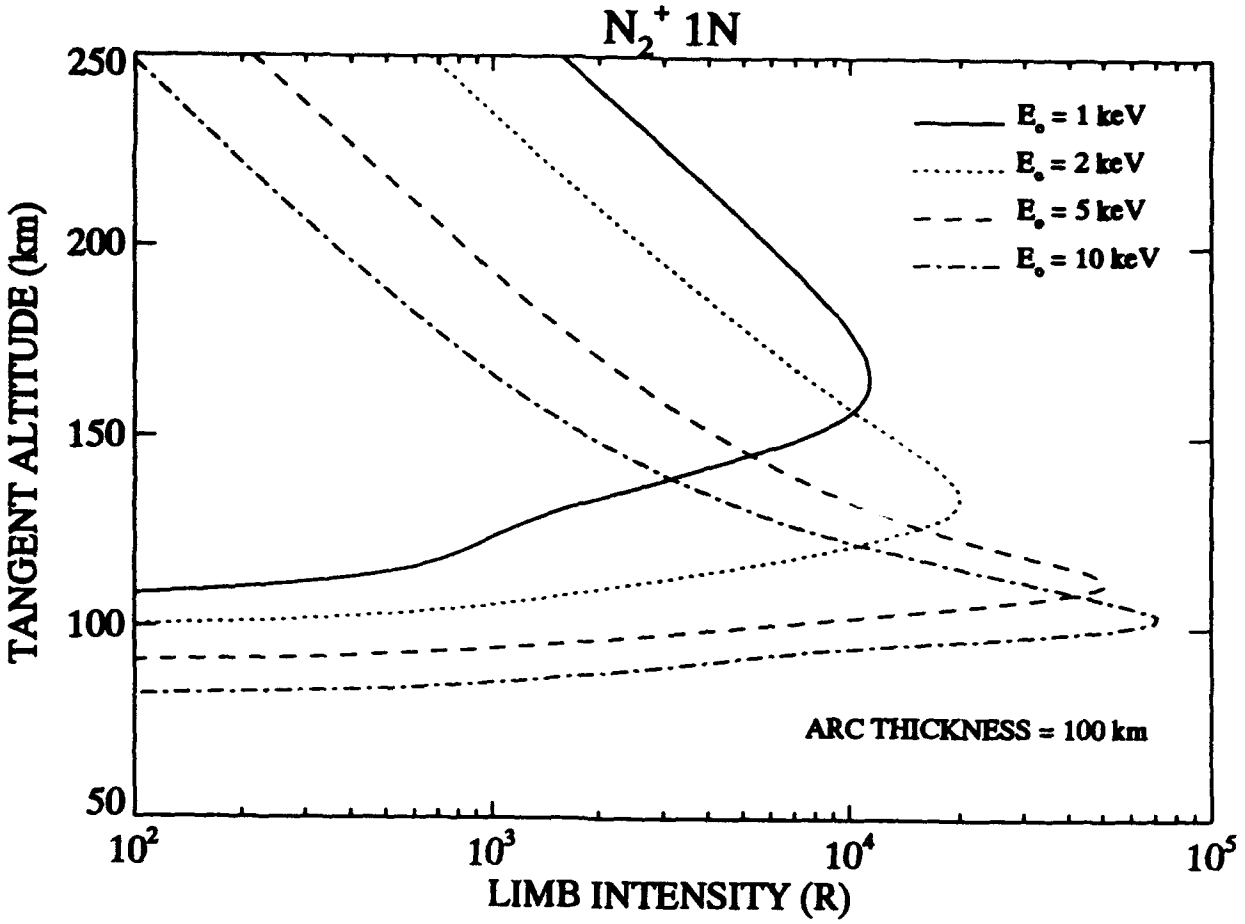
N_2^+ 1N
250
200
150
100
50
TANGENT ALTITUDE (km)
10^2
10^3
10^4
10^5
LIMB INTENSITY (R)
E_o = 1 keV
E_o = 2 keV
E_o = 5 keV
E_o = 10 keV
ARC THICKNESS = 100 km

Figure 7.

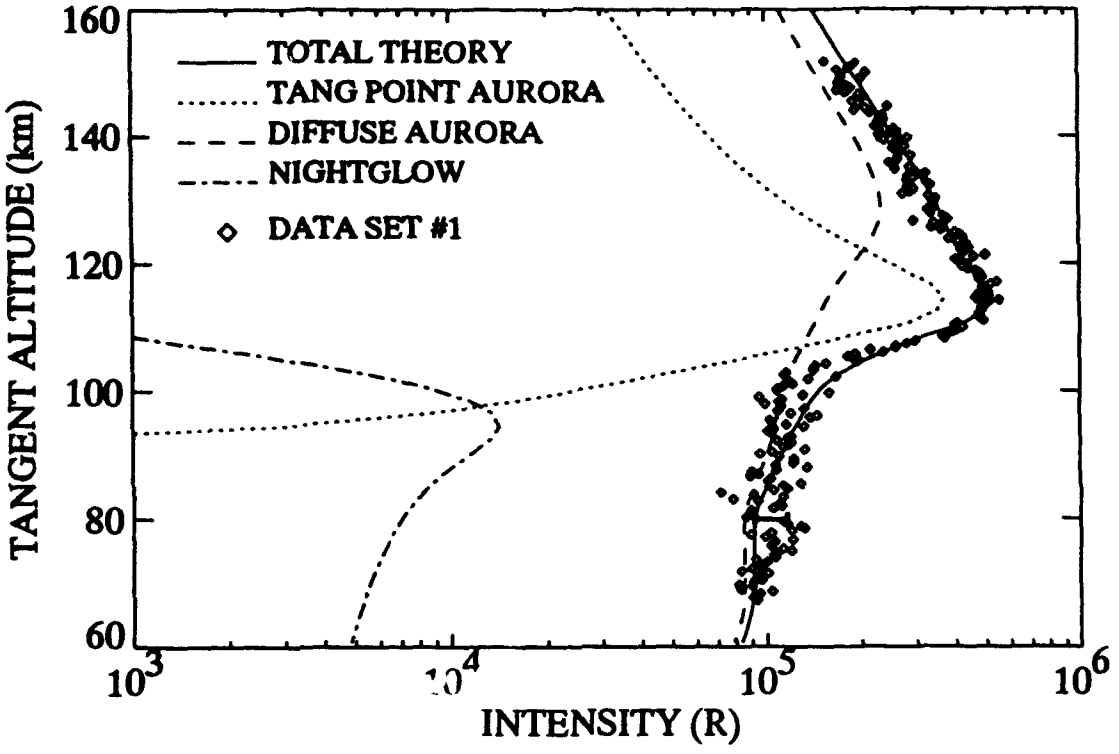
TOTAL THEORY
TANG POINT AURORA
DIFFUSE AURORA
NIGHTGLOW
DATA SET #1
TANGENT ALTITUDE (km)
160
140
120
100
80
60
10^3
10^4
10^5
10^6
INTENSITY (R)

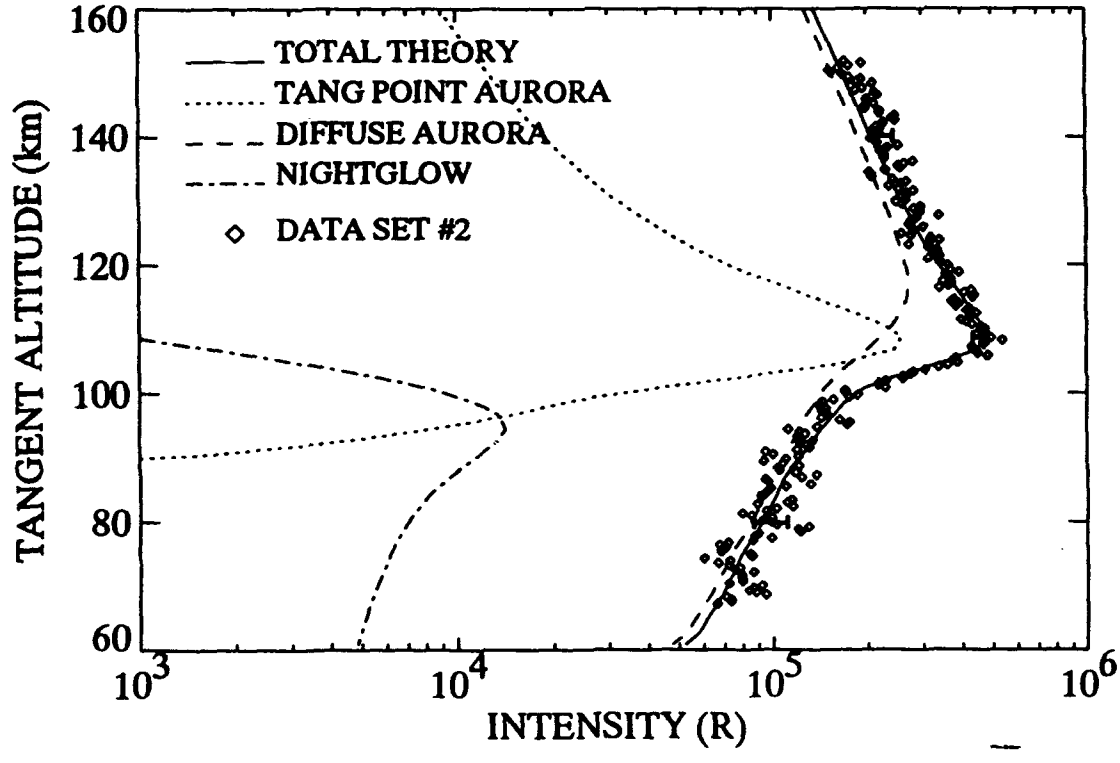
TOTAL THEORY
TANG POINT AURORA
DIFFUSE AURORA
NIGHTGLOW
DATA SET #2
TANGENT ALTITUDE (km)
160
140
120
100
80
60
10^3
10^4
10^5
10^6
INTENSITY (R)

Figure 8.

APPENDIX 2

A STUDY OF O^+ 834 Å LIMB EMISSION TO BE OBSERVED BY SSULI ON SATELLITE DMSP

Contributors:

D. J. Strickland
J. S. Evans
P. M. Shen

A STUDY OF O^+ 834 Å LIMB EMISSION TO BE OBSERVED BY SSULI ON SATELLITE DMSP

NRL CONTRACT No. N00014-88-C-2281

Prepared for:

The Naval Research Laboratory
Washington, D.C. 20375

Prepared by:

D. J. Strickland
J. S. Evans
P. M. Shen

Computational Physics, Inc.
2750 Prosperity Ave.
Suite 600
Fairfax, VA 22031

TABLE OF CONTENTS

FIGURES ..... p. i

TABLES ..... p. ii

1. INTRODUCTION ..... p. 1

2. KEY INPUT PARAMETERS ..... p. 1

3. SAMPLE DMSP ORBIT AND MODEL 834 Å LIMB PROFILES ALONG ORBIT ..... p. 3

4. CHAPMAN FUNCTIONS USED TO CHARACTERIZE O^+ DENSITY PROFILES ..... p. 8

5. EXAMPLES OF 834 Å VOLUME EMISSION RATES ..... p. 10

6. 834 Å LIMB PROFILES BASED ON CHAPMAN FUNCTIONS ..... p. 10

7. CONCLUSIONS ..... p. 18

8. REFERENCES ..... p. 23

FIGURES

1. Solar EUV spectrum used to calculate 834 Å emission by direct photoionization and by electron impact on O. The spectrum is based on the Hinteregger reference spectrum with scalings using an $F_{10.7}$ value of 200 . . . . . p. 4

2. Vertical perspective projection showing a 4:30 pm DMSP orbit at equinox . . . . p. 5

3. Solar zenith angle along the orbital track for 4:30 pm DMSP orbits at summer solstice (upper panel) and at equinox (lower panel) . . . . . p. 6

4. Dayside ICED electron density profiles at selected latitudes for a 4:30 pm DMSP orbit (upper panel) and corresponding O^+ 834 Å limb profiles observed from 850 km (lower panel). The O^+ density profiles used in the calculations were assumed to be spherically symmetric and equal to the profiles in the upper panel. An effective sunspot number of 200 and an effective Q value of 5 were used to specify the density profiles. A single MSIS-86 model atmosphere and solar zenith angle of 70° were used in order to unambiguously relate changes in 834 Å to changes in O^+ . . . . . p. 7

5. O^+ profiles taken from Figure 4 with a scaling or the -20° latitude profile (upper panel) in order to produce similar magnitudes in the corresponding 834 Å profiles shown in the lower panel. The diamonds represent simulated SSULI data based on the solid profile . . . . . p. 9

6. A subset of the Chapman functions used to characterize O^+ for determining the 834 Å limb profiles in Section 6. The values of the Chapman parameters for the displayed profiles are H_{top} = 120 km, $N_{max} = 10^6$ cm^{-3}, and h_{max} = 300 to 600 km in increments of 50 km . . . . . p. 11

7. Source functions S (labeled as volume emission rates) for the long wavelength line of the 834 Å triplet based on O^+ profiles with $N_{max} = 5x10^4$ cm^{-3} and h_{max} values of 300, 450, and 600 km. The same initial source function S_o for an SZA of 75° was used calculate each of the *Ss* . . . . . p. 12

8. Similar to Figure 6 except for $N_{max} = 5x10^5$ cm^{-3} . . . . . p. 13

9. Similar to Figure 6 except for $N_{max} = 5x10^6$ cm^{-3} . . . . . p. 14

10. 834 Å limb profiles versus look angle for the three lines combined. The corresponding tangent altitude ranges from 0 to 740 km. The profiles in the upper panel are for O^+ profiles with $N_{max} = 5x10^4$ cm^{-3} and h_{max} values from 300 to 600 km in 50 km increments. Similar profiles are displayed in the lower panel for $N_{max} = 10^5$ cm^{-3} . . . . . p. 15

11. Similar to Figure 9 except for N_{max} values of $5x10^5$ and 10^6 cm^{-3} . . . . . p. 16

12. Similar to Figure 9 except for $N_{max} = 5x10^6$ cm^{-3} . . . . . p. 17

13. Similar to Figures 9 - 11 except arranged to conveniently compare profiles for different N_{max} values. Profiles in the upper and lower panel are for h_{max} values of 300 and 350 km, respectively . . . . . p. 19

14. Similar to Figure 12 except for h_{max} values of 400 and 450 km . . . . . p. 20

15. Similar to Figure 12 except for h_{max} values of 500 and 550 km . . . . . p. 21

16. Similar to Figure 12 except for an h_{max} value of 600 km . . . . . p. 22

TABLES

1. Values of MSIS input parameters used to calculate 834 Å results . . . . . p. 2

2. Pure absorption and resonance cross sections of the 834 Å triplet lines used to perform the multiple scattering calculations . . . . . p. 2

1. INTRODUCTION

In this report, we begin to assess how well the daytime F-region O^+ density profile (effectively, the F-region electron density profile) can be inferred from O^+ 834 Å limb profiles to be obtained by the EUV/FUV limb sensor SSULI (Special Sensor Ultraviolet Limb Imager) on future DMSP (Defense Meteorogical Satellite Program) 5D3 satellites. Emphasis will be on the shape of the 834 Å limb profile and how sensitive it is to changes in the O^+ concentration which we will characterize by Chapman functions. The independent variables are peak density N_{max}, altitude of the peak, h_{max}, and topside scale height H_{top}. Changes in the 834 Å limb profile will be examined for changes in N_{max} from $5x10^4$ to $6x10^6$ cm^{-3} and h_{max} from 300 to 600 km. The topside scale height is kept fixed at 120 km. The dependence of 834 Å emission on O^+ is through the multiple scattering of its photons which are initially produced by photoionization of O with minor contributions from electron impact on O and resonance scattering of 834 Å solar photons. The dayglow model PEGFAC (Strickland and Meier, 1982) is used to calculate the initial 834 Å volume emission rates followed by use of code DSDA (Strickland and Anderson, 1983) to calculate the corresponding final rates obtained from multiple scattering calculations. Code LIMB is then used to perform line-of-sight integrations giving 834 Å limb intensity profiles in units of Rayleighs. For this study, the solar zenith angle (SZA) was held fixed along the line-of-sight. We refer the reader to the studies of Anderson and Meier (1985), McCoy et al. (1985), Cleary et al. (1989), Paxton and Strickland (1988), Strickland et al. (1993), and Link et al. (1993) for previous work on this problem.

2. KEY INPUT PARAMETERS

The model atmosphere used to calculate the 834 Å dayglow is MSIS-86 (Hedin, 1987). Table 1 shows the assumed values of its input parameters. We have chosen an $F_{10.7}$ value of 200 which corresponds to moderate to high solar activity. This value is also used to specify the solar EUV spectrum which will be discussed below. The resonance and pure

Table 1. Values of MSIS input parameters used to calculate 834 Å results.

Model Atmosphere	
Model	MSIS-86
Year	1990
Day	81
UT (sec)	0.0
Geo. lat	67.6°
Geo. lon	224.1°
$F_{10.7}$	200
$\langle F_{10.7} \rangle$	200
Ap	40

Table 2. Pure absorption and resonance cross sections of the 834 Å triplet lines used to perform the multiple scattering calculations.

Wavelength (Å)	Pure Absorption Cross Section (cm^2)			Resonance Cross Section (cm^2)
	N_2	O_2	O	
832	1.00×10^{-19}	3.30×10^{-17}	4.20×10^{-18}	4.14×10^{-14}
833	4.00×10^{-19}	1.40×10^{-17}	4.20×10^{-18}	8.80×10^{-14}
834	1.20×10^{-18}	1.10×10^{-17}	4.20×10^{-18}	1.22×10^{-13}

absorption cross sections needed to perform the multiple scattering calculations are shown in Table 2. The solar EUV spectrum comes from Hinteregger (1981a and 1981b) and is shown in Figure 1. Hinteregger provides an empirical model for wavelength dependent scaling of his reference spectrum to account for solar activity. The parameter used for the scaling is $F_{10.7}$. As noted above, we have used a value of 200 for producing this spectrum.

3. SAMPLE DMSP ORBIT AND MODEL 834 Å LIMB PROFILES ALONG ORBIT

Figure 2 shows a vertical perspective projection of a 4:30 pm DMSP orbit (this is the local time at that point in the orbit when the satellite crosses the equator going north). The satellite altitude is 850 km. The boundaries of the continents are positioned for a universal time of 00:00. The time of year is equinox (either spring or fall) as indicated by the placement of the terminator. The SZA along the orbit is of particular interest since it is one of the parameters defining the region of useable data from SSULI. Calculations of SZA have been performed for the above orbit and another at summer solstice. Figure 3 shows these results versus latitude over a full period of the orbit. At equinox, the minimum value is about 67°. The corresponding value at summer solstice is about 52°. The range of useful data is at SZA values less than approximately 80°.

Simulations of SSULI 834 Å limb observations (without noise) along the above displayed orbit are given in the lower panel of Figure 4. The ionospheric specification model ICED (Tascione et al., 1988) was used to specify the O^+ profiles for the multiple scattering calculations (equated to ICED's electron density profile). The profiles corresponding to the 834 Å results appear in the upper panel. A single model atmosphere and SZA (70°) have been used in order to directly relate changes in 834 Å to O^+. It should be noted that these results were obtained at a later date than those to follow in subsequent sections. The radiative transfer model of Gladstone (1982) was used to perform the multiple scattering

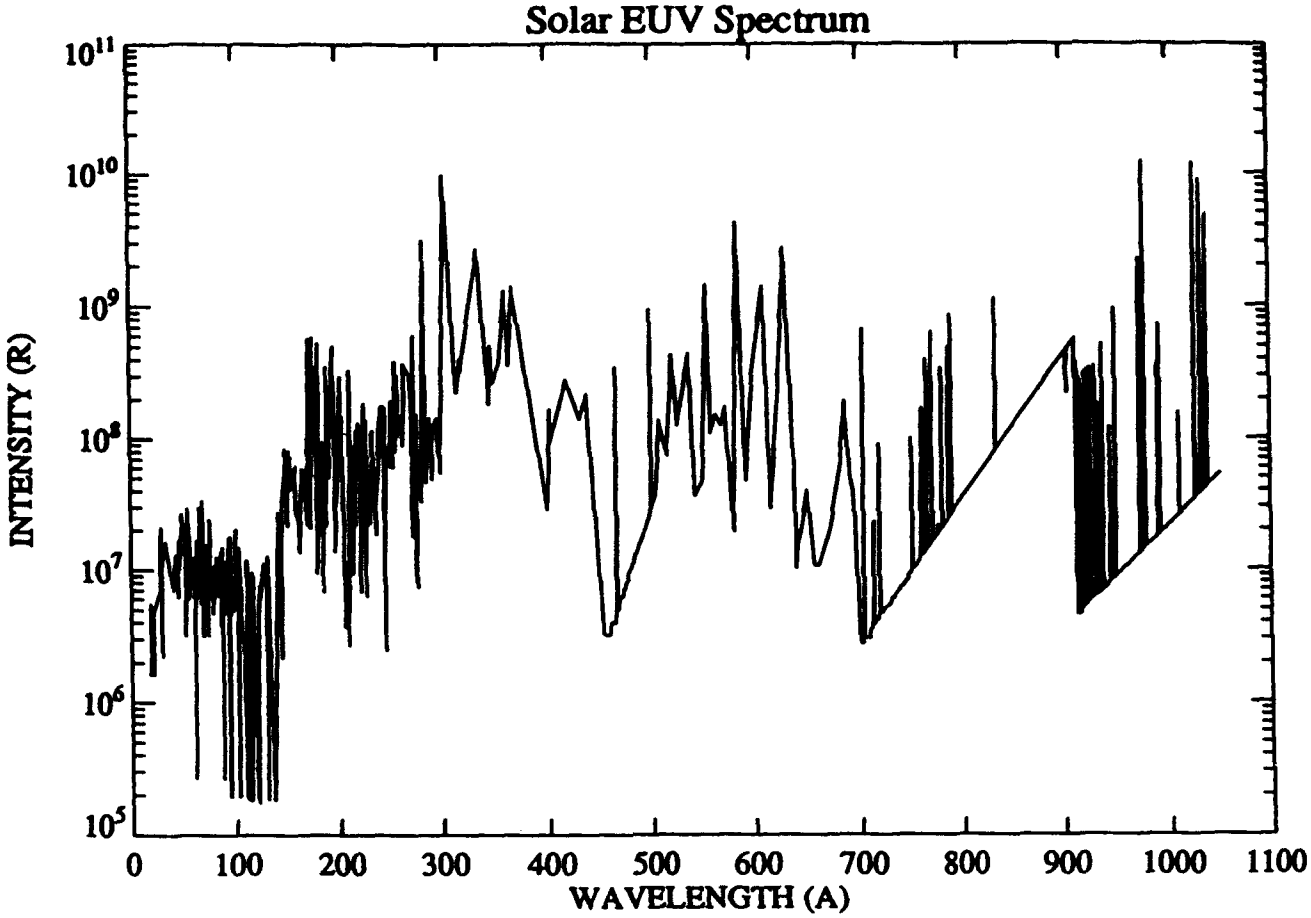

Figure 1. Solar EUV spectrum used to calculate 834 Å emission by direct photoionization and by electron impact on O. The spectrum is based on the Hinteregger reference spectrum with scalings using an $F_{10.7}$ value of 200.

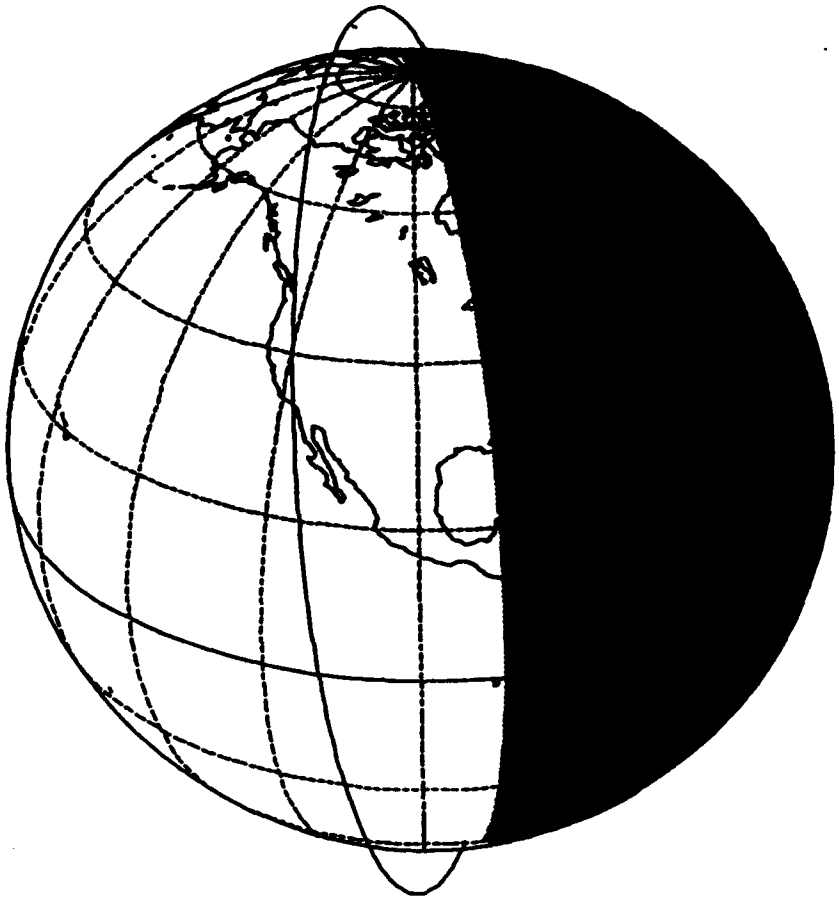

Figure 2. Vertical perspective projection showing a 4:30 pm DMSP orbit at equinox.

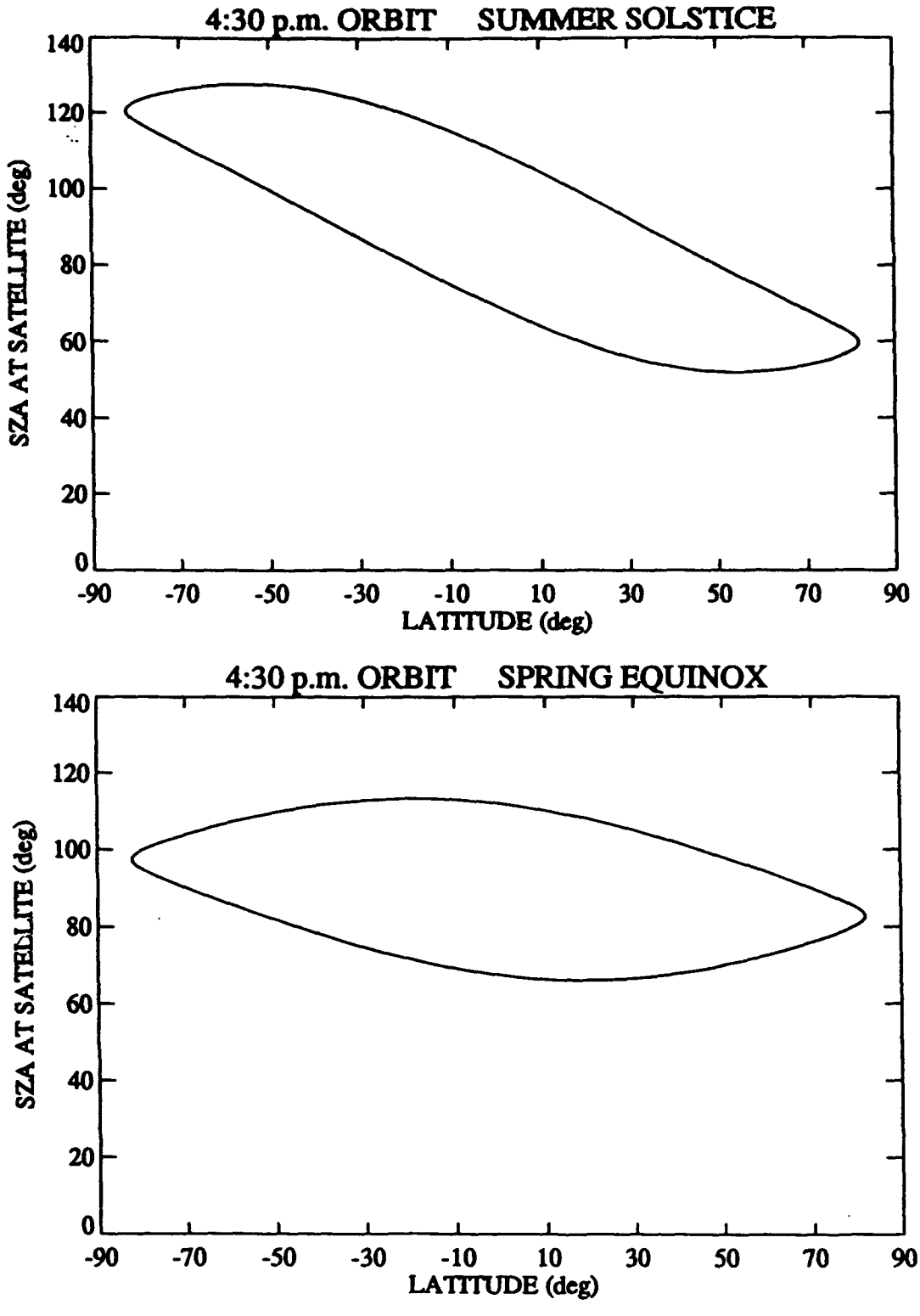

Figure 3. Solar zenith angle along the orbital track for 4:30 pm DMSP orbits at summer solstice (upper panel) and at equinox (lower panel).

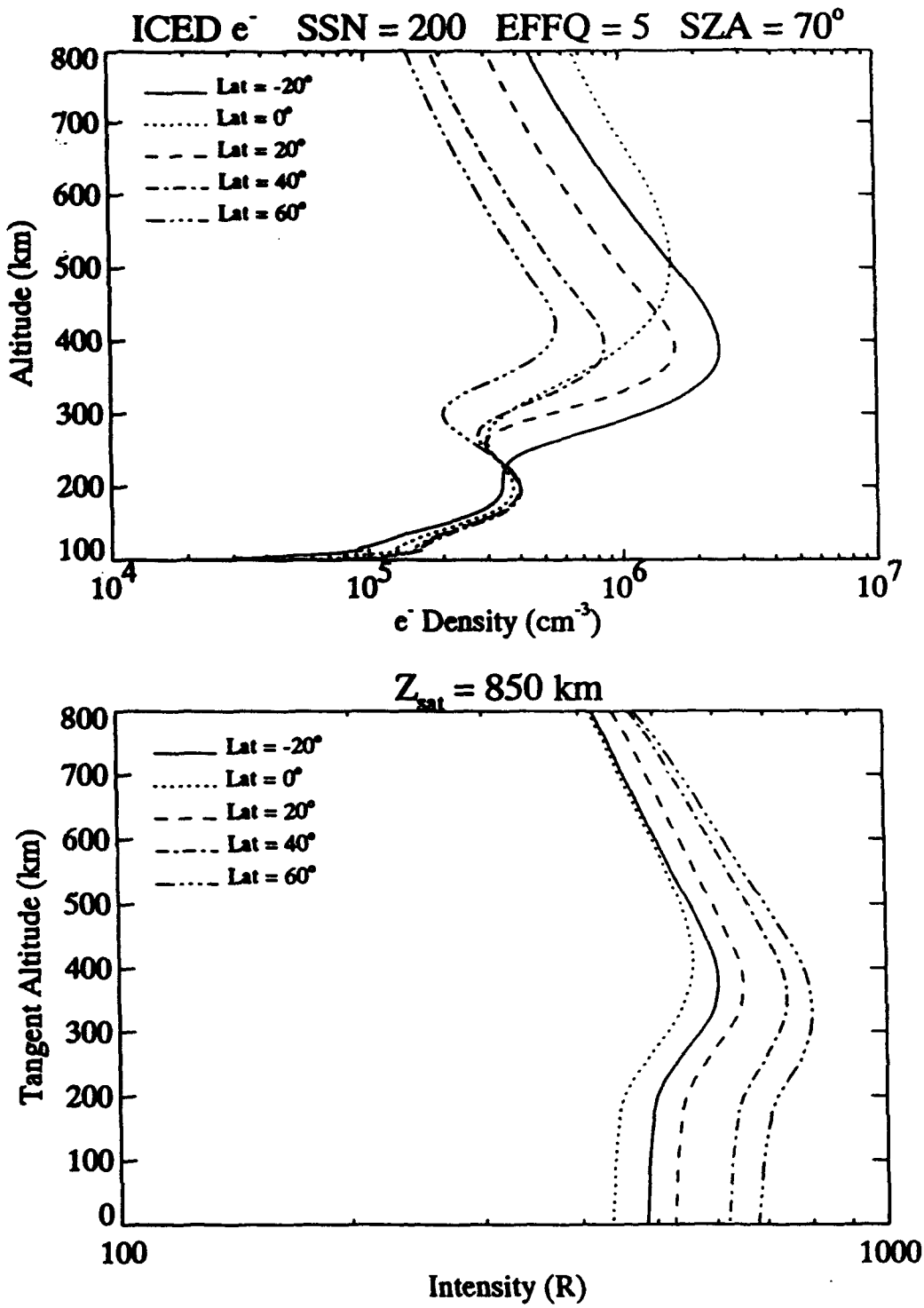

Figure 4. Dayside ICED electron density profiles at selected latitudes for a 4:30 pm DMSP orbit (upper panel) and corresponding O^+ 834 Å limb profiles observed from 850 km (lower panel). The O^+ density profiles used in the calculations were assumed to be spherically symmetric and equal to the profiles in the upper panel. An effective sunspot number of 200 and an effective Q value of 5 were used to specify the density profiles. A single MSIS-86 model atmosphere and solar zenith angle of 70° were used in order to unambiguously relate changes in 834 Å to changes in O^+.

calculations. Those to follow in later sections used codes DSDA and LIMB. Comparisons have been made between the models and show similar results for 834 Å.

The shapes of the 834 Å profiles in Figure 4 are similar in spite of the corresponding O^+ profiles having N_{max} values ranging from 0.5 to 2.5 x 10^6 cm^{-3} and h_{max} values ranging from 370 to 500 km. The magnitude of the 834 Å profile decreases as O^+ increases since attenuation by self absorption more than compensates for increases in the source function (see Section 5 for the dependence of the source function on O^+). To further examine the dependence of shape of the 834 Å limb profile on O^+, the O^+ profile at -20° latitude (solid curve) has been scaled to produce an 834 Å profile similar in magnitude to that at 0°. The upper panel in Figure 5 shows the unscaled O^+ profile at 0° and the scaled profile at -20°. The lower panel shows the corresponding 834 Å profiles in counts based on a calibration factor of .2 counts/s/R, 90 s/limb scan, and 1 s/measurement. While the magnitudes are similar, their peaks do differ by about 50 km in tangent altitude. This difference arises for profiles having the same scale heights. With differing scale heights, the difference could be either larger or smaller. The diamonds show a simulation of the measurements based on the solid curve using Poisson statistics. Note that unlike the previous figure, the results are shown on a linear intensity scale. This simulation suggests that it will not be possible to distinguish between O^+ profiles like those in the upper panel which are in the range expected for daytime conditions. These profiles show substantial differences with the ratio of N_{max}'s exceeding a factor of two and the h_{max}'s differing by more than 100 km. The difference in TEC up to 800 km is more than a factor of two.

4. CHAPMAN FUNCTIONS USED TO CHARACTERIZE O^+ DENSITY PROFILES

At the request of R. McCoy of NRL, calculations of the 834 Å limb profile were performed for O^+ distributions given by Chapman functions. These results will be presented in the next section. McCoy requested that this be done for five values of N_{max}, seven values of h_{max}, and a single value for H_{top} (we selected this value to be 120 km). The N_{max} values in

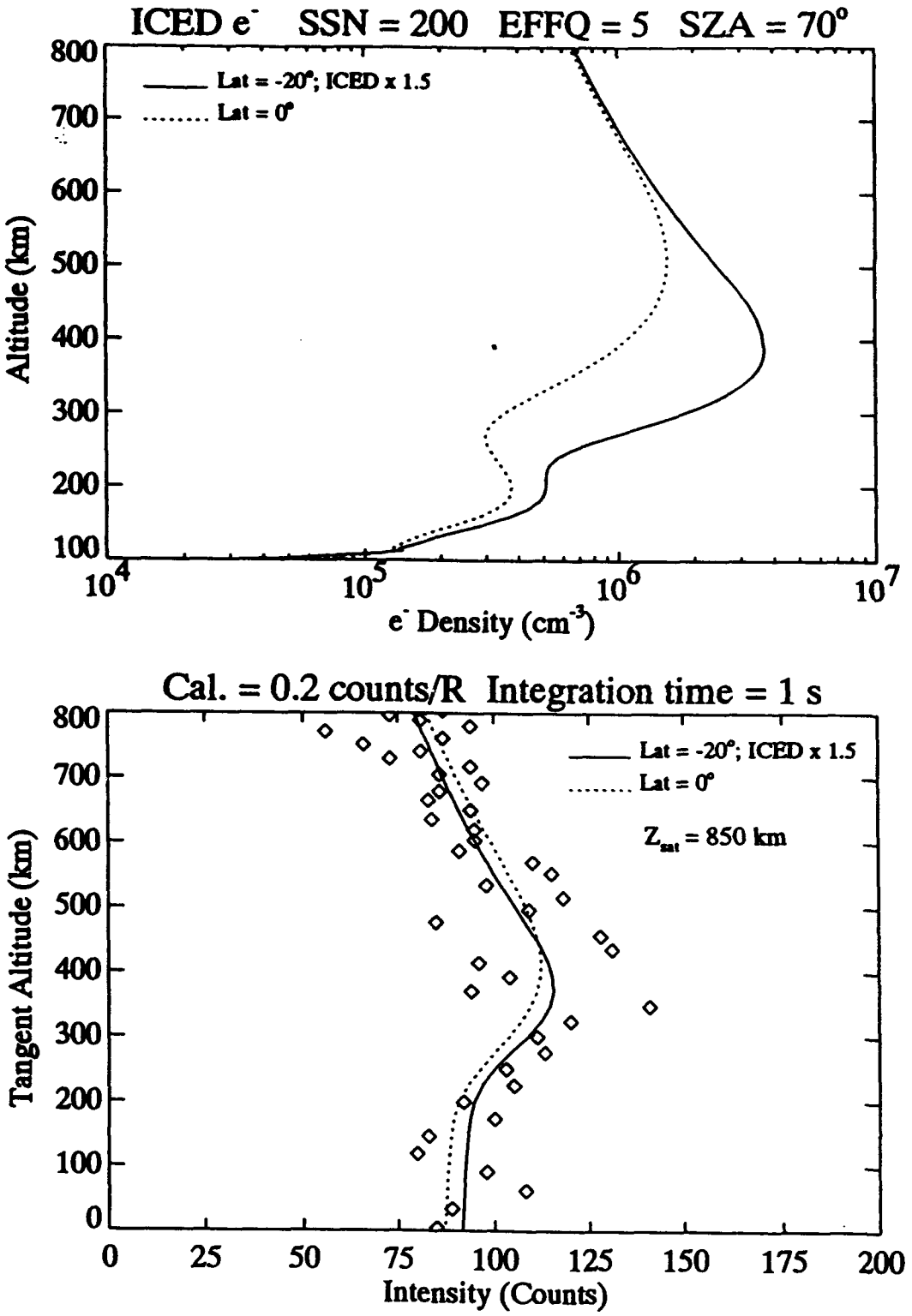

Figure 5. O^+ profiles taken from Figure 4 with a scaling of the -20° latitude profile (upper panel) in order to produce similar magnitudes in the corresponding 834 Å profiles shown in the lower panel. The diamonds represent simulated SSULI data based on the solid profile.

units of 10^5 cm^{-3} are 0.5, 1.0, 5.0, 10, and 50. Units of 10^5 cm^{-3} will be used in the remainder of this report when discussing N_{max}. A value of 50 is somewhat larger than expected at solar maximum while the values of .5 and 1 are more appropriate to nighttime conditions. We will take note of this when discussing the 834 Å results in the next section. The h_{max} values uniformly span the range from 300 to 600 km in 50 km increments. The larger values apply to O^+ distributions in the tropical arcs which are situated to either side of the geomagnetic equator. Figure 6 shows Chapman functions for the seven h_{max} values and the single N_{max} value of 10 (in the above units).

5. EXAMPLES OF 834 Å VOLUME EMISSION RATES

Examples of the source function S(z) (total volume emission rate) for the long wavelength line of the triplet (at 834 Å) will follow. They were obtained from code DSDA using a single initial source function S_o (initial emission from the sources cited in Section 1) based on the parameters given in Section 2 and an SZA of 75°. The large SZA reflects the situation to be encountered during a 4:30 pm orbit. Three figures follow for N_{max} values of 0.5, 5.0, and 50. Figure 7 shows S for N_{max} = .5 and h_{max} = 300, 450, and 500 km along with the single S_o cited above. Figures 8 and 9 show similar results for the other two N_{max} values. As expected, S departs increasingly from S_o as N_{max} and h_{max} become larger. Corresponding limb profiles show much less sensitivity to O^+ due to a compensating effect by the transmission function for self absorption. This was seen in Figures 4 and 5 and will be seen in results to follow.

6. 834 Å LIMB PROFILES BASED ON CHAPMAN FUNCTIONS

Figures 10 - 12 give 834 Å limb profiles for the combined three lines in displays

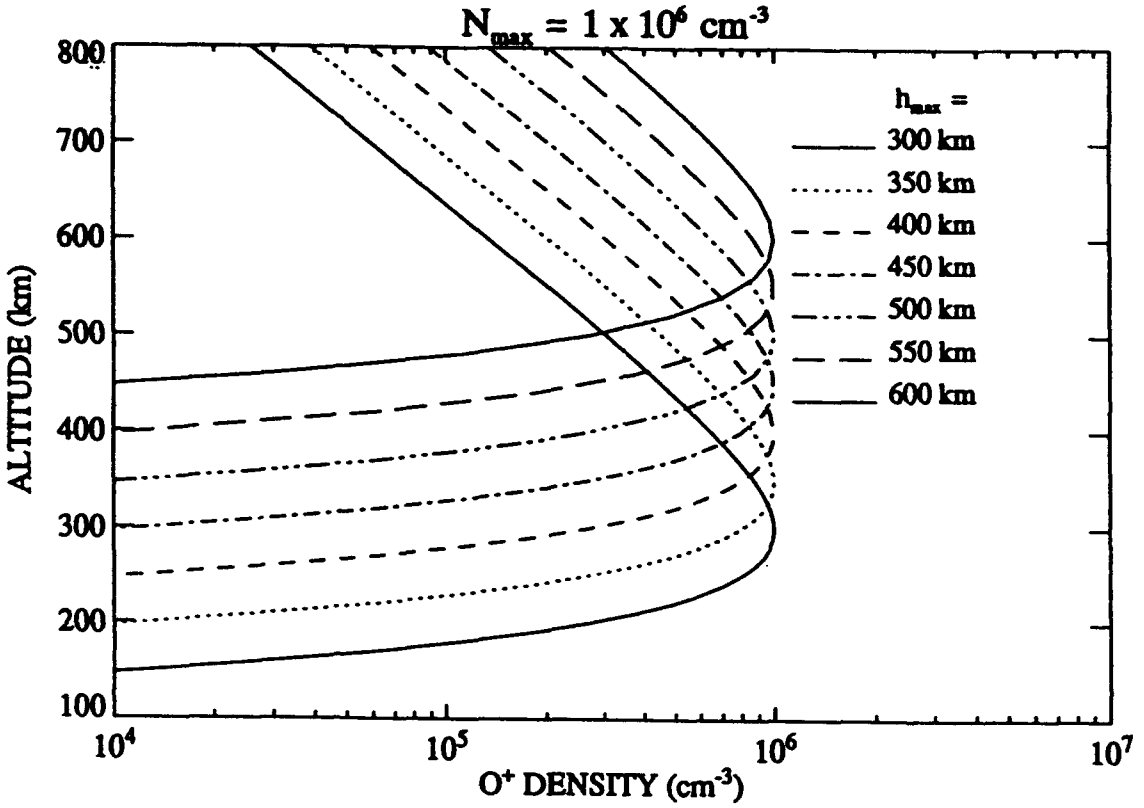

Figure 6. A subset of the Chapman functions used to characterize O^+ for determining the 834 Å limb profiles in Section 6. The values of the Chapman parameters for the displayed profiles are H_{bp} = 120 km, N_{max} = 10^6 cm^{-3}, and h_{max} = 300 to 600 km in increments of 50 km.

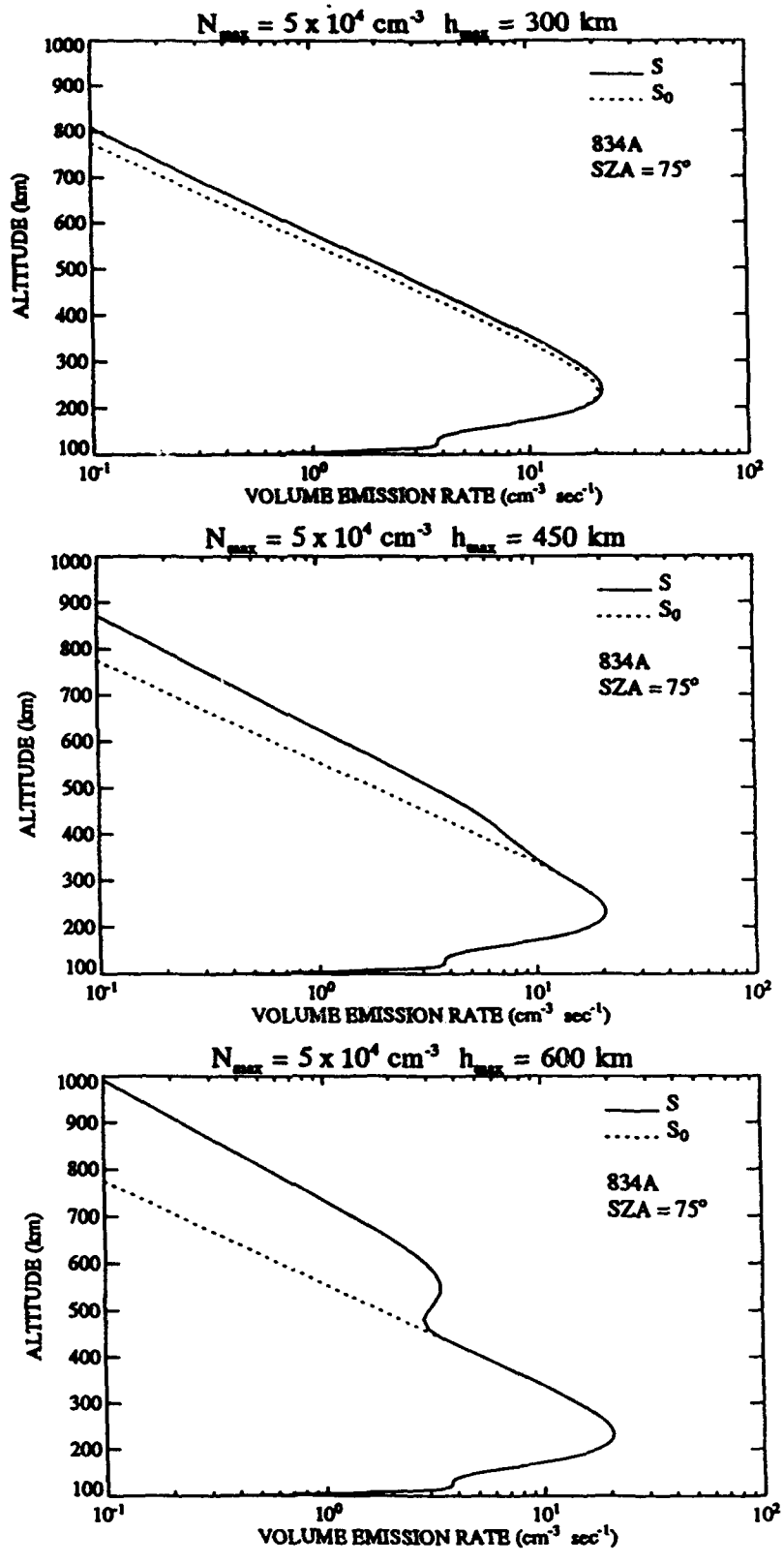

Figure 7. Source functions S (labeled as volume emission rates) for the long wavelength line of the 834 Å triplet based on O^+ profiles with N_{max} = 5x10^4 cm^{-3} and h_{max} values of 300, 450, and 600 km. The same initial source function S_o for an SZA of 75° was used calculate each of the S*s*.

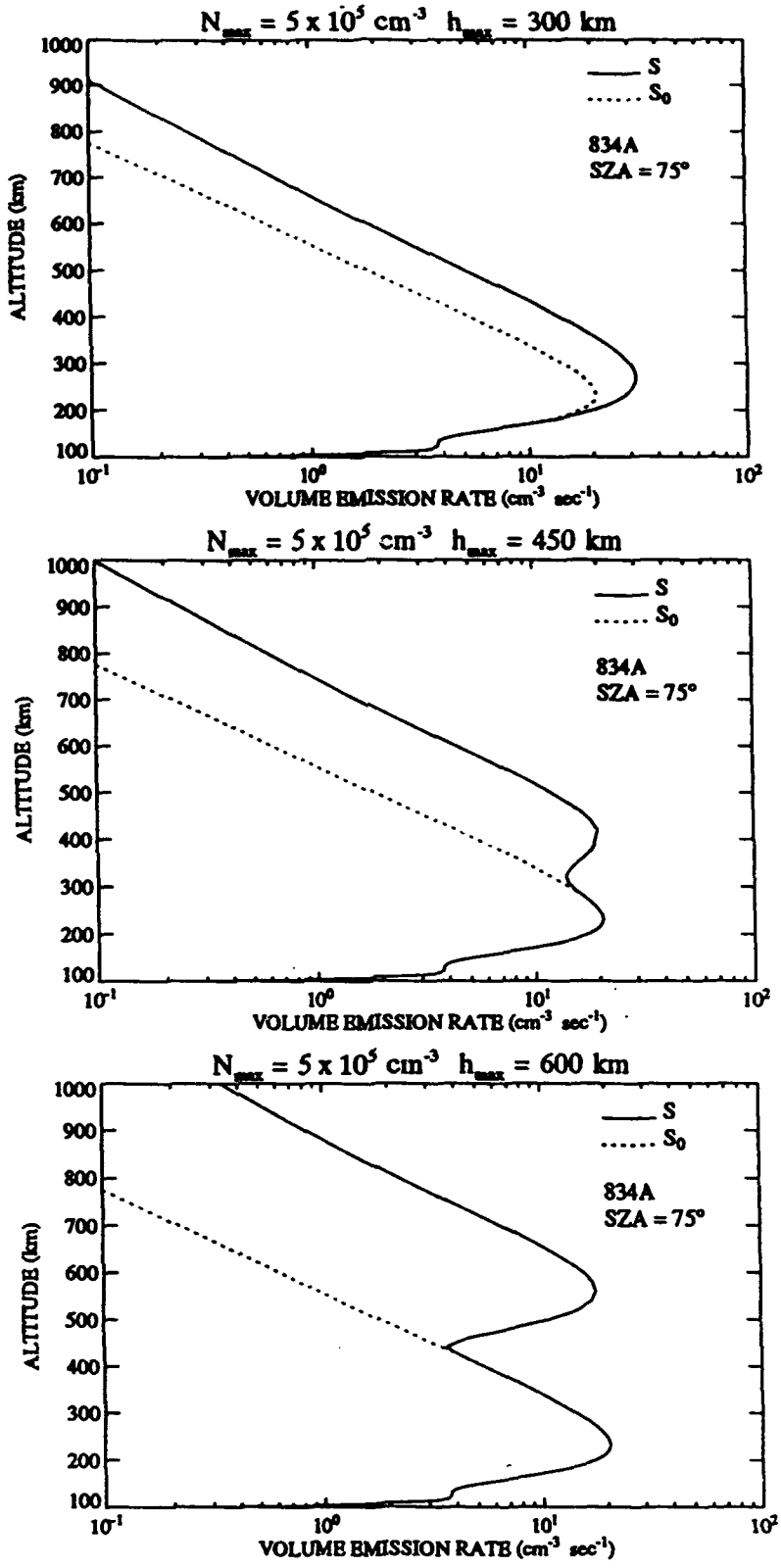

Figure 8. Similar to Figure 6 except for N_{max} = 5x10^5 cm^{-3}.

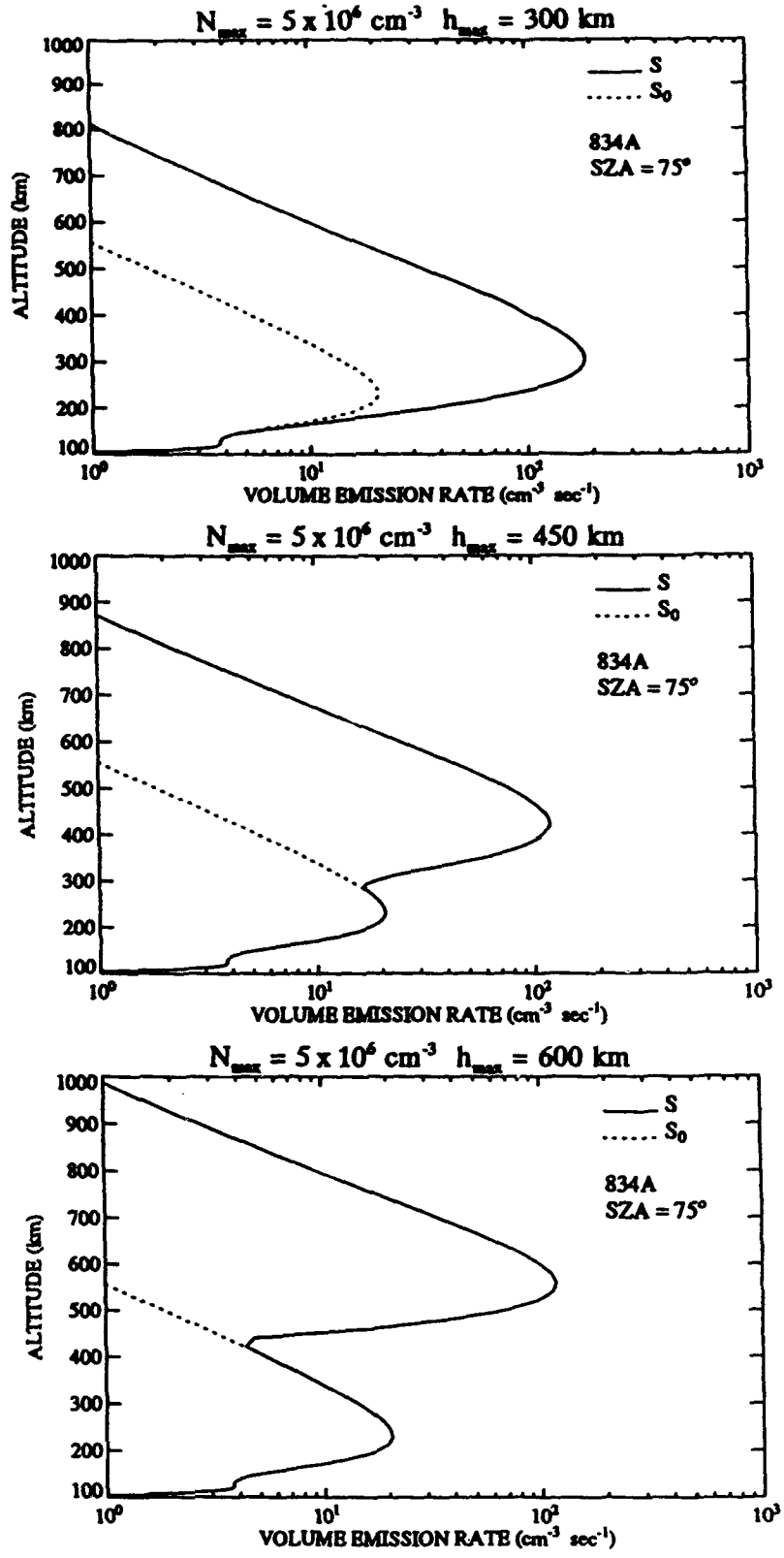

Figure 9. Similar to Figure 6 except for N_{max} = 5x10^6 cm^{-3}.

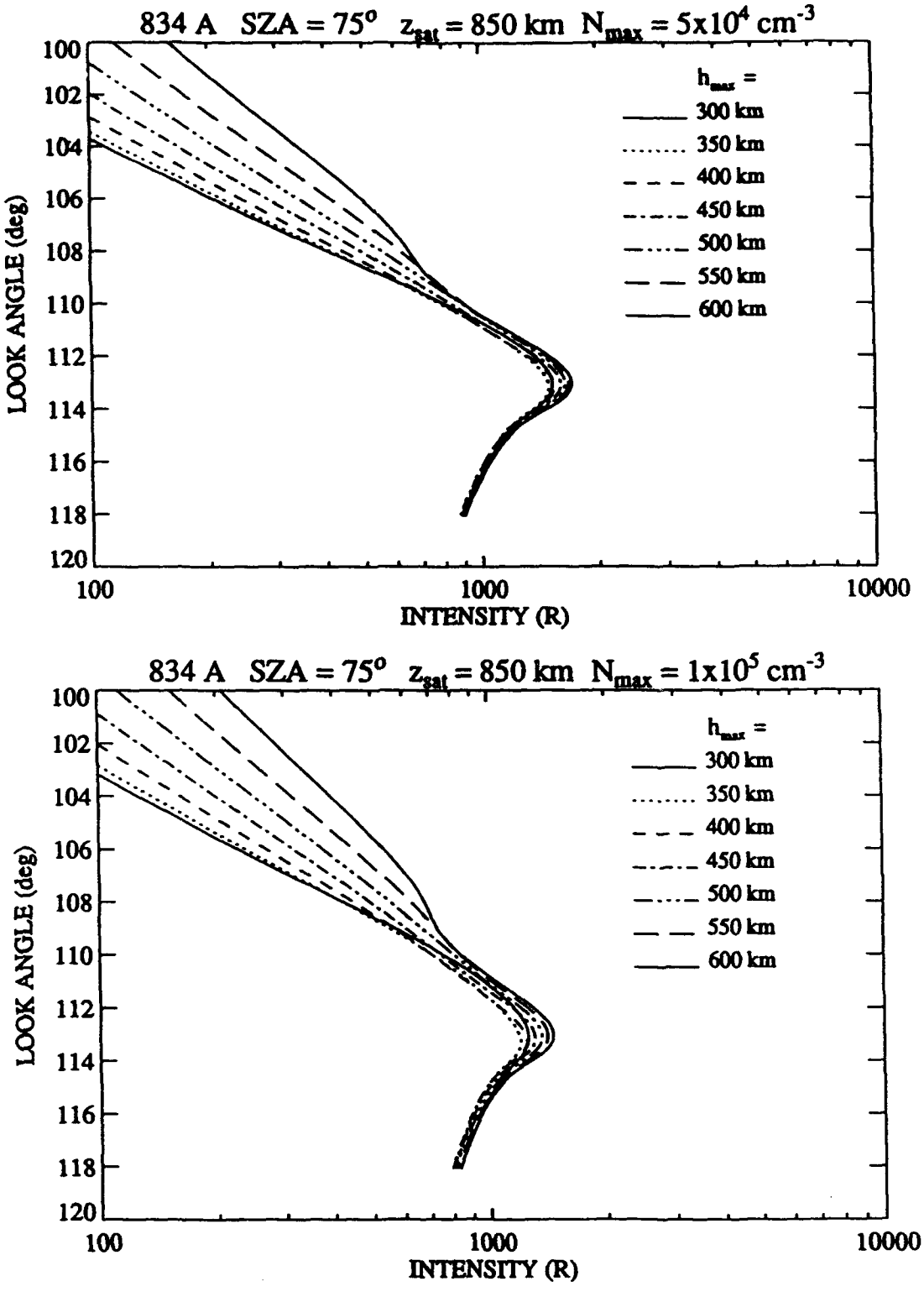

Figure 10. 834 Å limb profiles versus look angle for the three lines combined. The corresponding tangent altitude ranges from 0 to 740 km. The profiles in the upper panel are for O^+ profiles with N_{max} = 5x10^4 cm^{-3} and h_{max} values from 300 to 600 km in 50 km increments. Similar profiles are displayed in the lower panel for N_{max} = 10^5 cm^{-3}.

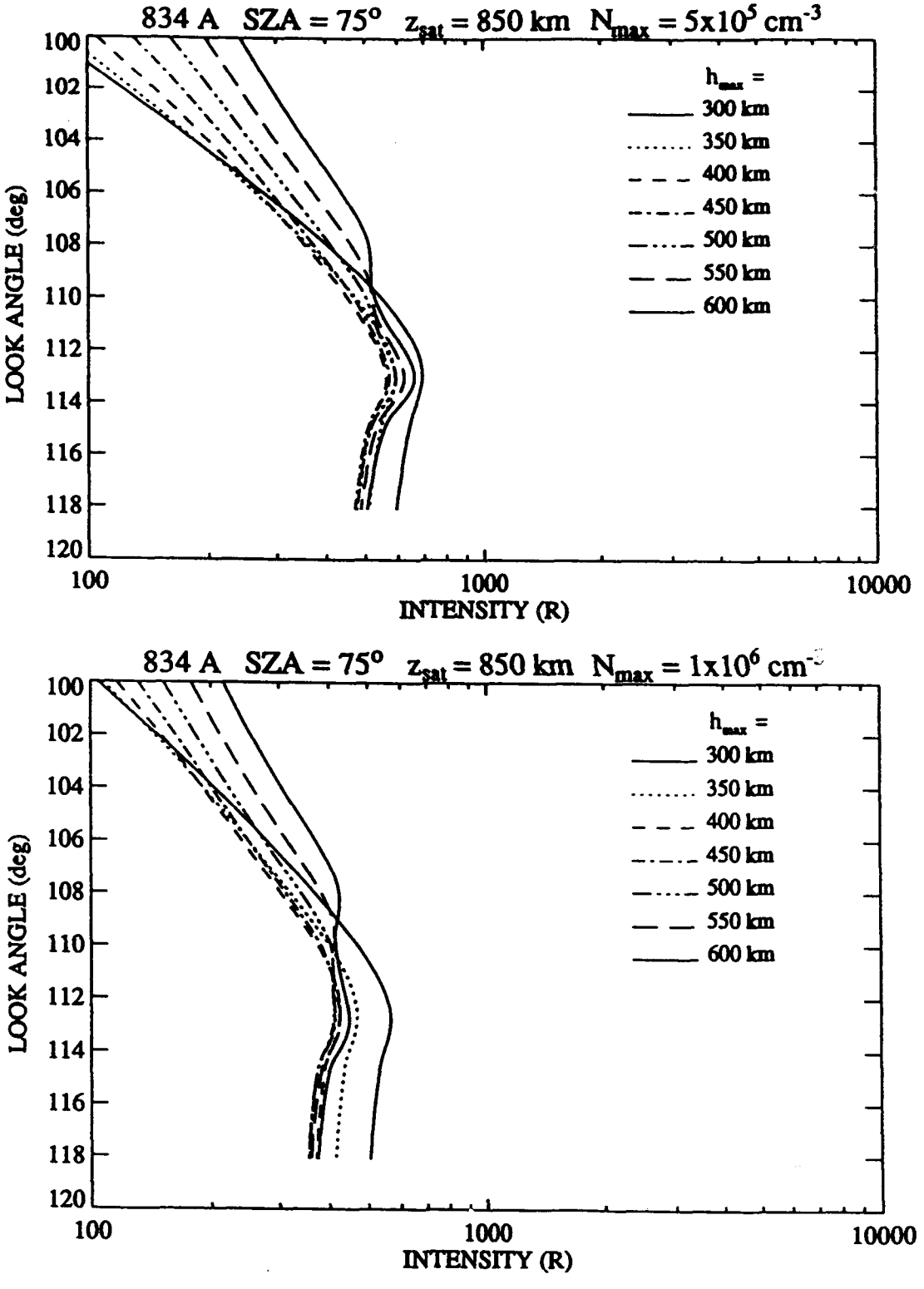

Figure 11. Similar to Figure 9 except for N_{max} values of 5x10^5 and 10^6 cm^{-3}.

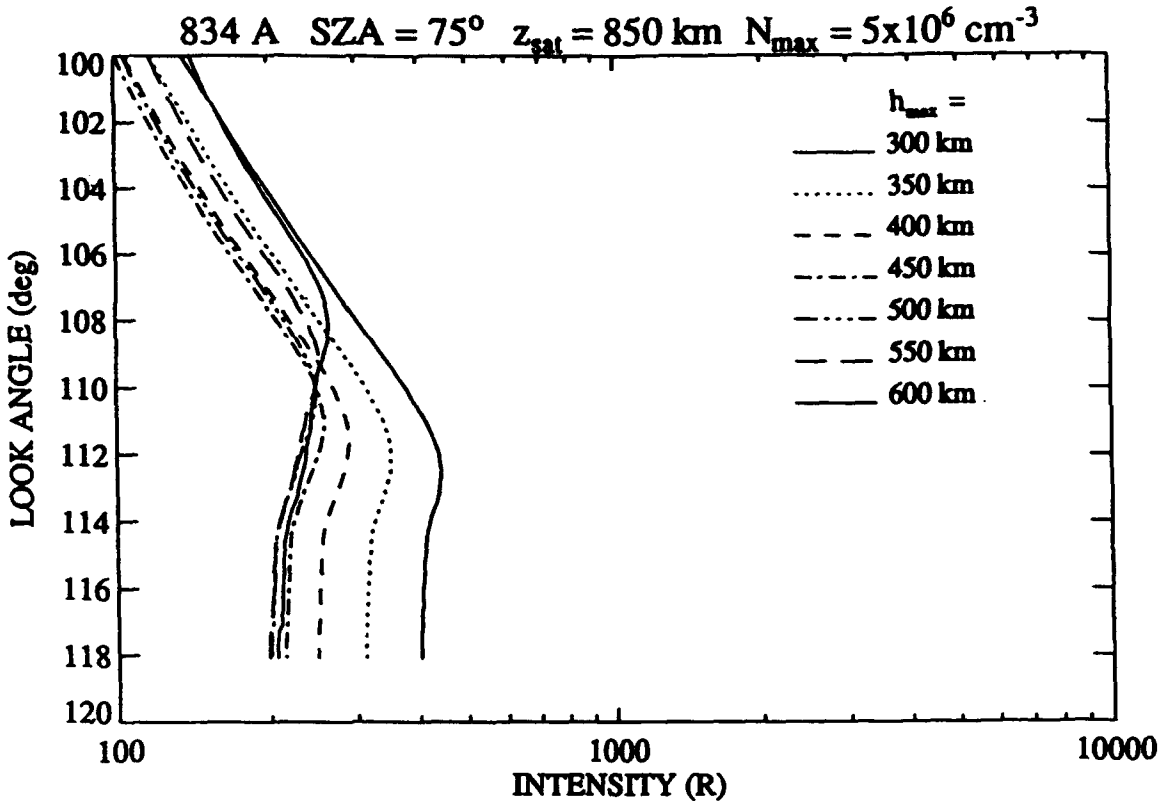

Figure 12. Similar to Figure 9 except for N_{max} = 5x10^6 cm^{-3}.

convenient for showing the effect of changing h_{max}. For example, the upper panel of Figure 10 shows profiles for the seven chosen values of h_{max} at the smallest selected N_{max} value (0.5). The profiles are displayed versus look angle (0° refers to zenith viewing) and correspond to tangent altitudes from 0 to 740 km. The remaining panels in these figures refer to the rest of the selected N_{max} values. Figures 13 - 16 show the same results from the previous three figures expect versus N_{max} in each of seven panels for the seven h_{max} values. In a given panel, the 834 Å profile is seen to flatten as N_{max} increases. It becomes less bright near and below its peak and brighter at high tangent altitudes. The overall behavior is caused by a combination of changes in S (see Figures 7 - 9) and transmission effects along the line-of-sight. The latter effects lead to the decrease in brightness at the lower tangent altitudes. At high tangent altitudes, these effects are weak allowing for detection of the enhancement in S caused by increases in N_{max}.

For remote sensing of O^+, measurement of changes in the shape of the 834 Å is more important than measurement of absolute brightness. Measured brightness is a function of calibration, the solar EUV flux, neutral composition, SZA along the line-of-sight, and finally O^+. The uncertainties associated with the first three of these items will not allow for the desired accuracy in determining O^+ from the overall magnitude of the observed profile. Regarding shape, there is considerable variation over the full range of N_{max} values considered. Nevertheless, the variation is weak over the range expected for nominal daytime conditions (10 to 30).

7. CONCLUSIONS

A sensitivity study has been undertaken to better understand the expected properties of 834 Å data to be obtained by SSULI. Calculated 834 Å limb profiles have been presented for O^+ profiles given by the model ICED and by Chapman functions. While considerable variation in the shape of the 834 Å profile is exhibited over the full range of N_{max} (0.5 to 50 in units of 10^5 cm^{-3}) and h_{max} (300 to 600 km) considered (at an SZA of 75°), only a modest change occurs over the expected range of these parameters for most daytime conditions.

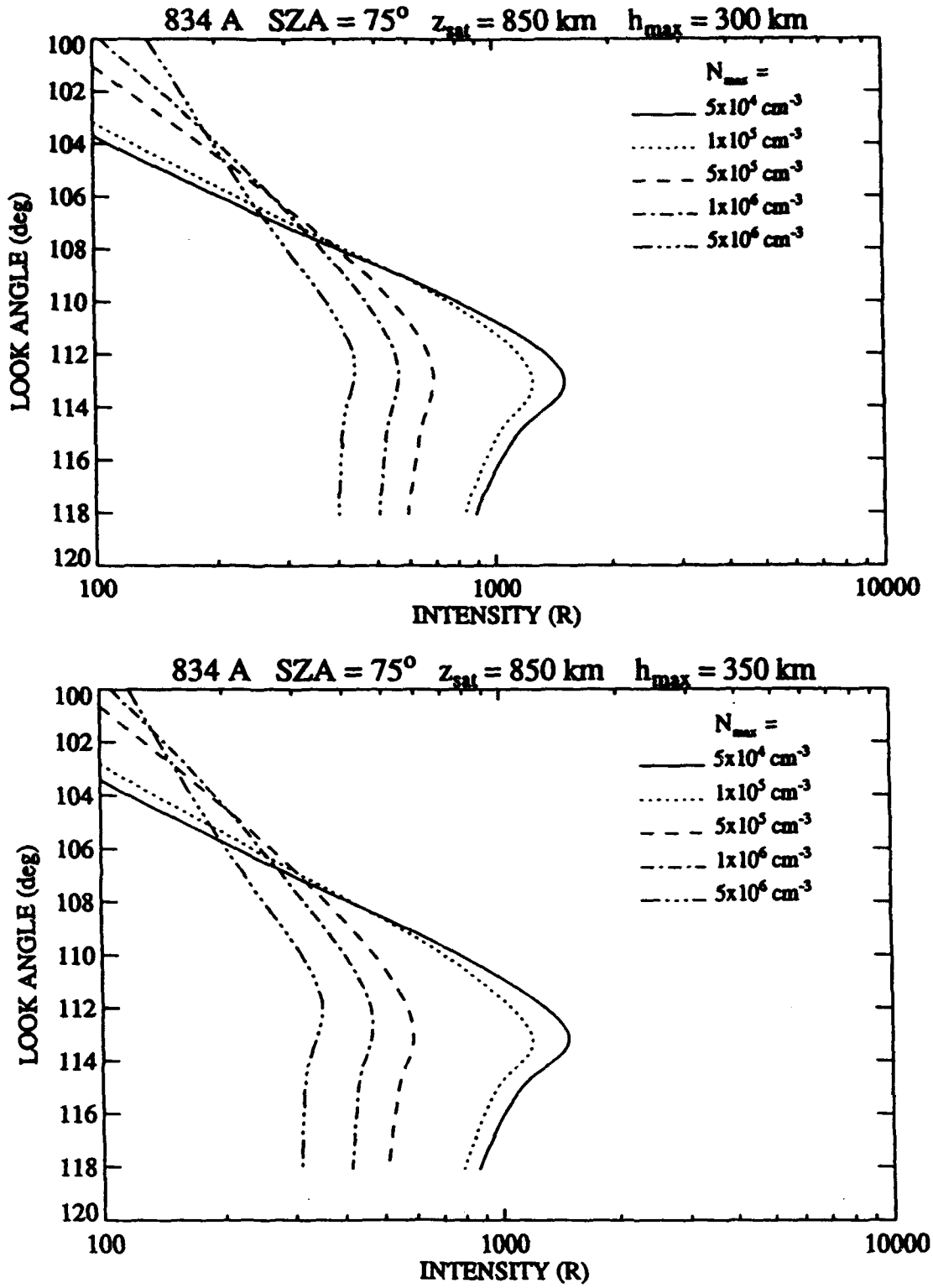

Figure 13. Similar to Figures 9 - 11 except arranged to conveniently compare profiles for different N_{max} values. Profiles in the upper and lower panel are for h_{max} values of 300 and 350 km, respectively.

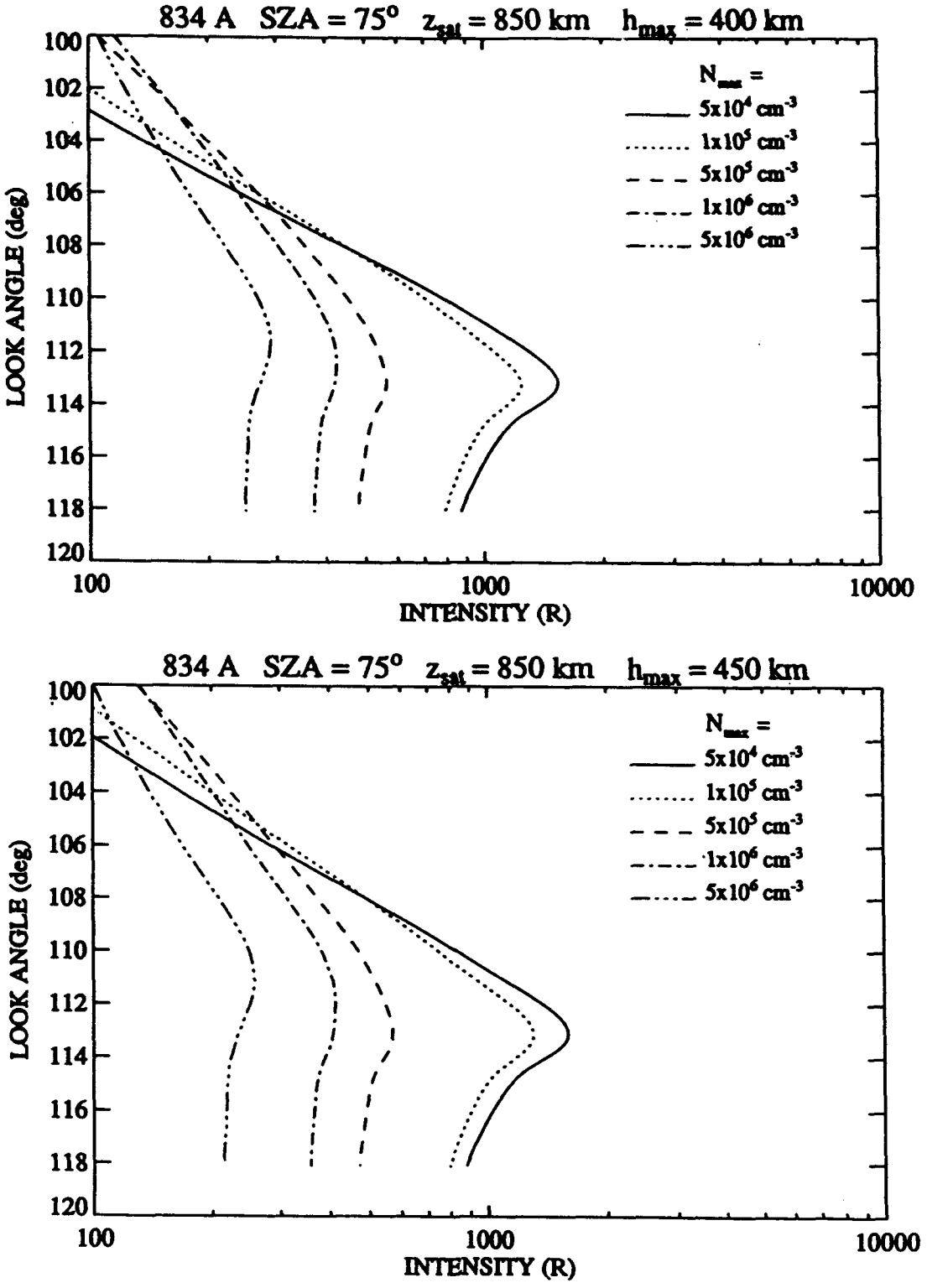

Figure 14. Similar to Figure 12 except for h_{max} values of 400 and 450 km.

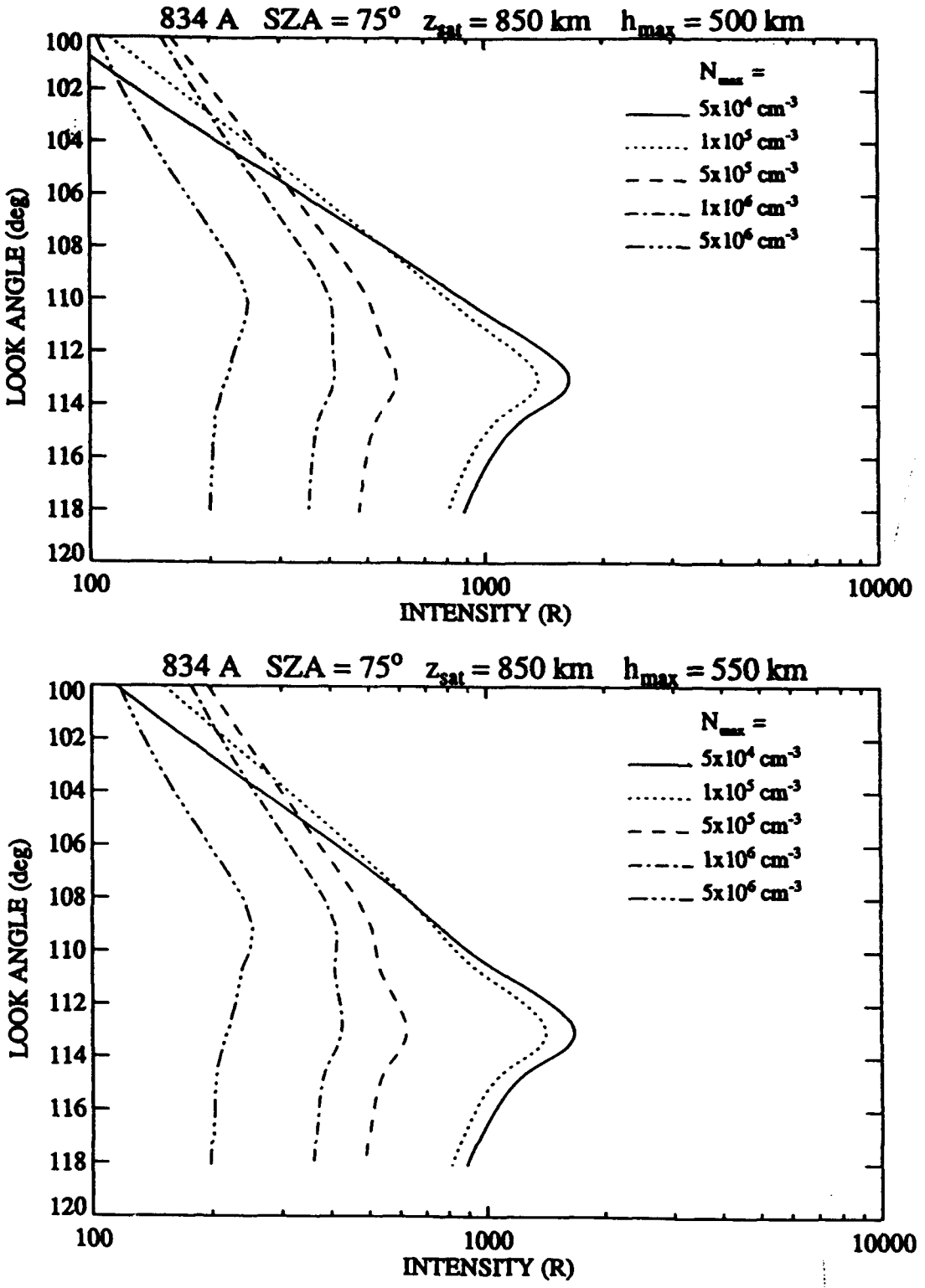

Figure 15. Similar to Figure 12 except for h_{max} values of 500 and 550 km.

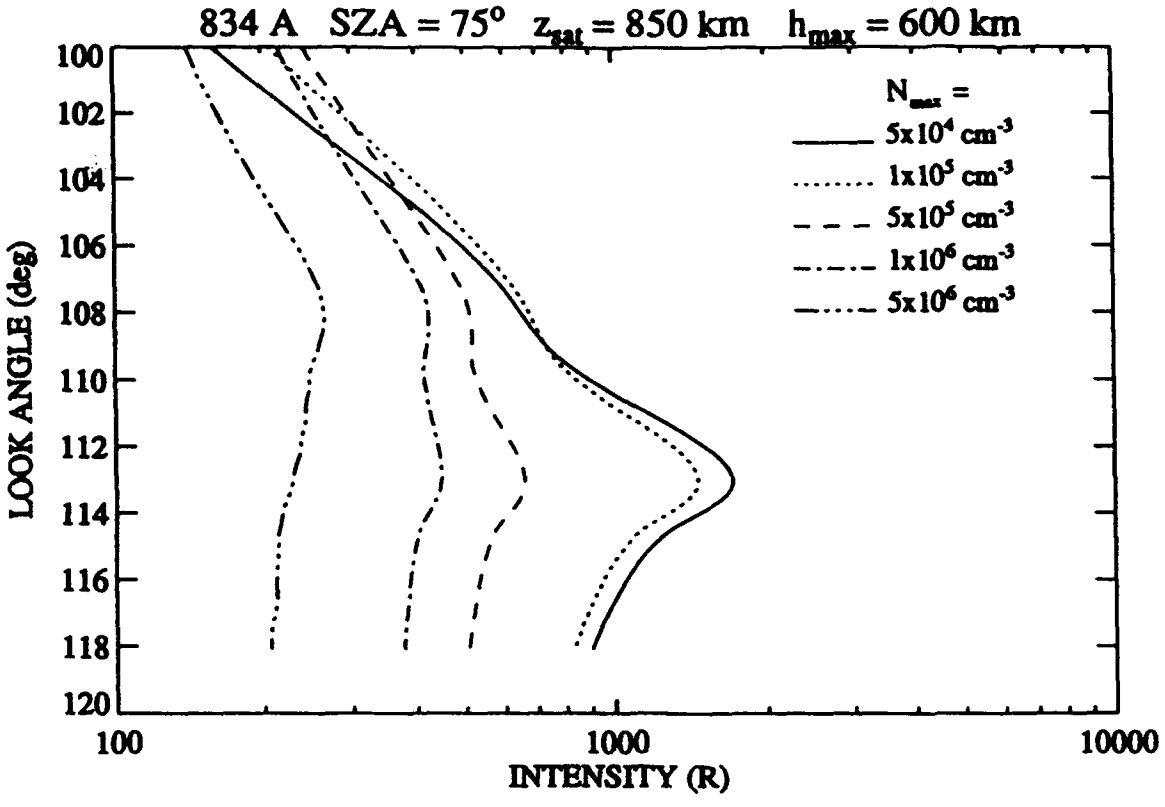

Figure 16. Similar to Figure 12 except for an h_{max} value of 600 km.

8. REFERENCES

Anderson, D. E., Jr., and R. R. Meier, The OII 834 A dayglow: A general model for excitation rate and intensity calculations, *Planet. Space Sci., 33*, 1179, 1985.

Cleary, D. D., R. R. Meier, E. P. Gentieu, P. D.Feldman, and A. B.Christensen, An analysis of the effects of N_2 absorption on the O^+ 834 Å emission from rocket observations, *J. Geophys. Res., 94*, 17281, 1989.

Hedin, A. E., MSIS-86 Thermospheric Model, *J. Geophys, Res., 92*, 4649, 1987.

Hinteregger, H.E., Representations of solar EUV fluxes for aeronomical applications, *Adv. Space Res., 1*, 39, 1981a.

Hinteregger, H.E., K. Fukui and B.R. Gibson, Observational, reference, and model data on solar EUV from measurements of AE-E, *Geophys. Res. Lett., 8*, 1147, 1981b.

Link, R., J. S. Evans, and G. R. Gladstone, The O^+ 834-Å dayglow: Revised cross sections, submitted to *J. Geophys. Res.*, February, 1993.

McCoy, R. P., D. E. Anderson, Jr., and S. Chakrabarti, F_2 region ion densities from analysis of O^+ 834 A airglow: A parametric study and comparision with satellite data, *J. Geophys. Res., 90*, 12257, 1985.

Paxton, L. J., and D. J. Strickland, EUV imaging of the ionosphere from space, *SPIE, 932, Ultraviolet Technology II*, 190, 1988.

Strickland, D. J., R. J. Cox, R. P. Barnes, L. J. Paxton, R. R. Meier, and S. E. Thonnard, A model for generating global images of emission from the thermosphere , in press, *J. Applied*

Opt., 1993.

Strickland, D. J., and R. R. Meier, A photoelectron model for the rapid computation of atmospheric excitation rates, *NRL Memo. Report 5004*, Naval Research Laboratory, Washington, D.C., 20375-5000, 1982.

Strickland, D. J., and D. E. Anderson, Jr., Radiation transport effects on the OI 1356 Å limb intensity profile in the dayglow, *J. Geophys. Res.*, *88*, 9260, 1983.

Tascione, T. F., H. W. Kroehl, R. Creiger, J. W. Freeman, Jr., R. A. Wolf, R. W. Spiro, R. V. Hilmer, J. W. Shade, and B. A. Hausman, New ionospheric and magnetospheric specification models, *Radio Sci.*, *23*, 211, 1988.

APPENDIX 3

DEVELOPMENT OF AN INVERSION ALGORITHM FOR RETRIEVING MESOSPHERIC O_3 AND THERMOSPHERIC O_2 DENSITY PROFILES FROM SUSIM SOLAR OCCULTATION DATA

Contributors:

J. D. Lumpe
C. S. Chang
D. J. Strickland

SUSIM

CPI has been involved in an ongoing effort to develop inversion algorithms for the retrieval of O_2 and O_3 number density profiles from solar occultation data to be obtained from the SUSIM instrument on UARS. This problem is challenging because SUSIM views the full solar disk, in contrast to most current occultation experiments in which the instrument field of view is restricted to only a small fraction of the disk. The resulting inversion problem requires the solution of two successive integral equations, one arising from the integration over the finite source and the second due to the integration along the slant path through the atmosphere, which is an inherent feature of the limb viewing geometry. The latter gives rise to the well known Abel integral equation.

The initial method proposed for the inversion involved using simulations to generate a model dependent functional relationship between the extinction (or normalized intensity) profile and the slant column density of the absorbing species. Given an extinction profile measured by SUSIM, the corresponding column density was obtained by a simple interpolation on this functional relationship, assuming an initial model profile and iterating until some convergence criterion was satisfied. The number density profile was then determined by numerically evaluating the Abel integral, using a quadratic least squares fit to the column density in order to minimize magnification of errors due to statistical fluctuations in the data. This method was capable of determining the overall magnitude of the ozone density profile assuming that the vertical structure was (somehow) known beforehand. This is not usually the case of course, and in general the algorithm failed to converge to the correct density profile in realistic simulations.

An improved inversion algorithm has been developed over the past 2-3 years which shows real promise for extracting useful O_2 and O_3 vertical profiles. This algorithm solves the finite source integral equation by expanding both the measured absorption profile and the unknown number density profile in terms of Laguerre polynomials. The integral equation is therefore solved exactly, resulting in a smooth, analytic representation for the density profile. This method does not require the assumption of an initial model density - the data themselves determine unambiguously the number density profile. The essential assumptions made are that there is only one dominant absorbing constituent at the wavelength of interest and that the concentration of this species possesses spherical symmetry, i.e., it is a function of altitude only.

A detailed discussion of the algorithm may be found in the published paper which has been included here in Appendix A. It is worthwhile to discuss briefly several improvements which have been made in the algorithm since its initial publication. A more general approach has been developed for the solution of arbitrary integral equations utilizing the same idea of expansions in complete sets of orthogonal polynomials. This generalized algorithm is simpler both in terms of the mathematical formalism and its numerical implementation on the computer. One major practical improvement is the ease with which solar limb darkening effects may be incorporated into the new algorithm. Other corrections to the original solution, such as

wavelength dependence of the absorption cross sections across the instrument bandpass and variations of the apparent solar disk size with altitude are also more easily incorporated into the new framework.

By way of example we present in Figs. 1-4 several representative results from simulations of SUSIM occultation data for both O_2 and O_3. These results were generated using the code SOLOC, which contains both a forward module for accurate simulation of SUSIM data as well as the inversion algorithm discussed above. These simulations involve the following steps. First a model O_2 or O_3 density profile is used to generate a slant column density as a function of tangent altitude. The resulting transmission profile is then integrated over the solar disk, as well as the instrument bandpass, to generate the integrated extinction profile as a function of altitude. Finally, a random number generator is used to simulate realistic effects of statistical scatter in the data. This data profile is then read into the inversion algorithm and the retrieved number density profile is compared to the original model profile to determine the accuracy of the inversion procedure. It should be noted that the inversion cannot be exact once it has been corrupted by random noise, which means that it is impossible in principle to extract exactly the model density profile under these conditions. The most one can hope for is that the model profile and the extracted profile are consistent to within the total error bars specified on the extracted profile. At this point the error analysis has not been completed and so there are no error bars given on the inversion results.

In Fig. 1, the top panel shows a simulated full disk absorption profile for ozone (open squares) and the fit generated with 25 terms in the Laguerre expansion (solid line). The wavelength is 3090 Angstroms, with narrow/narrow slit configuration. The lower panel shows the percentage difference between the data and the fit as a function of tangent altitude. Note the random nature of the scatter about the fit, on the order of 10% at high altitudes. Figure 2 shows the retrieved ozone density (solid line) vs the initial model density used to generate the data (dotted line). Figures 3 and 4 are similar results for an O_2 measurement at 1600 Angstroms. Note that although there is more statistical noise in the O_2 data, due to the diminished solar flux at 1600 Angstroms, the density retrieval is better than for the O_3 case, largely because the larger scale height of O_2 requires many fewer terms in the Laguerre expansion (5 vs 25). Overall, however, both results are encouraging.

FIGURE CAPTIONS

Fig. 1a — Simulation of measured full disk absorption profile for ozone at 3090 A (open squares) compared to the Laguerre expansion fit with N = 25 (solid line).

Fig. 1b — Percentage difference between the data and fit shown in Figure 1.

Fig. 2 — Deduced ozone density obtained from retrieval algorithm (solid line) compared to model ("true") density used to generate the data (dotted line).

Figs. 3a-b — Same as Figure 1 except the simulated measurement is O_2 at a wavelength of 1600 A and the Laguerre expansion has 5 terms.

Fig. 4 — Same as Figure 2 but for the O_2 retrieval problem.

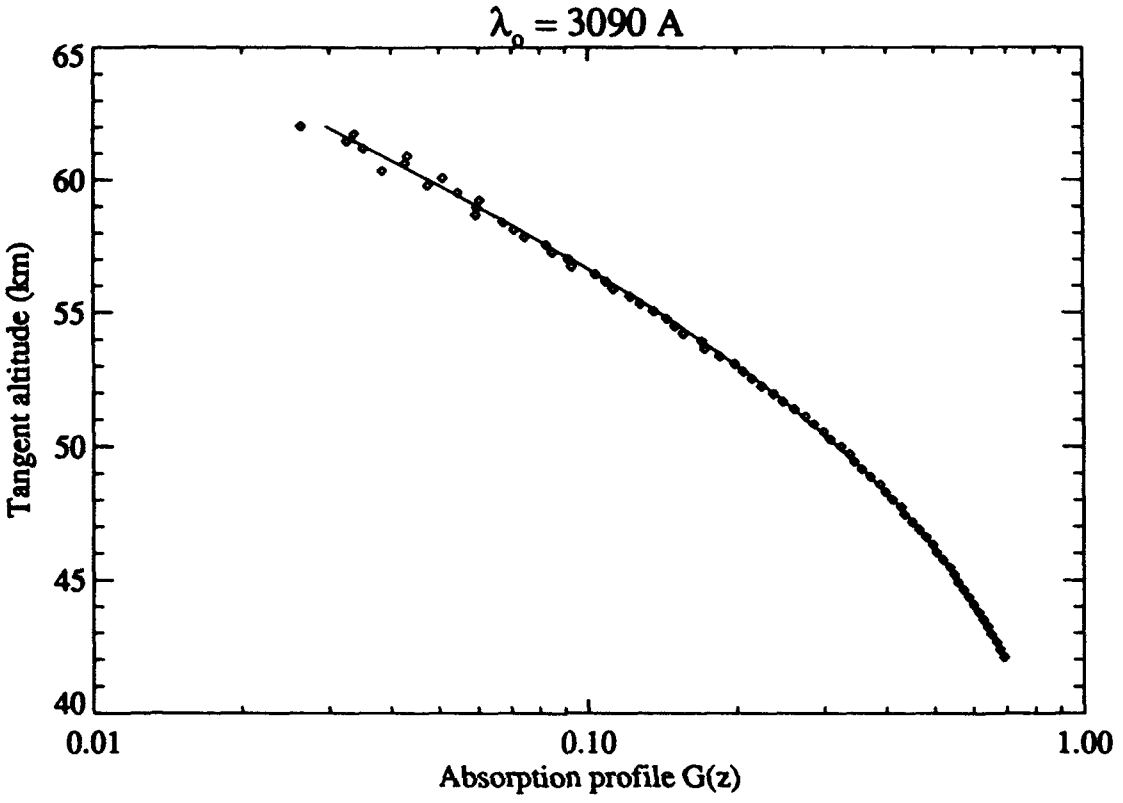
λ0 = 3090 A
Tangent altitude (km)
65
60
55
50
45
40
0.01
0.10
1.00
Absorption profile G(z)

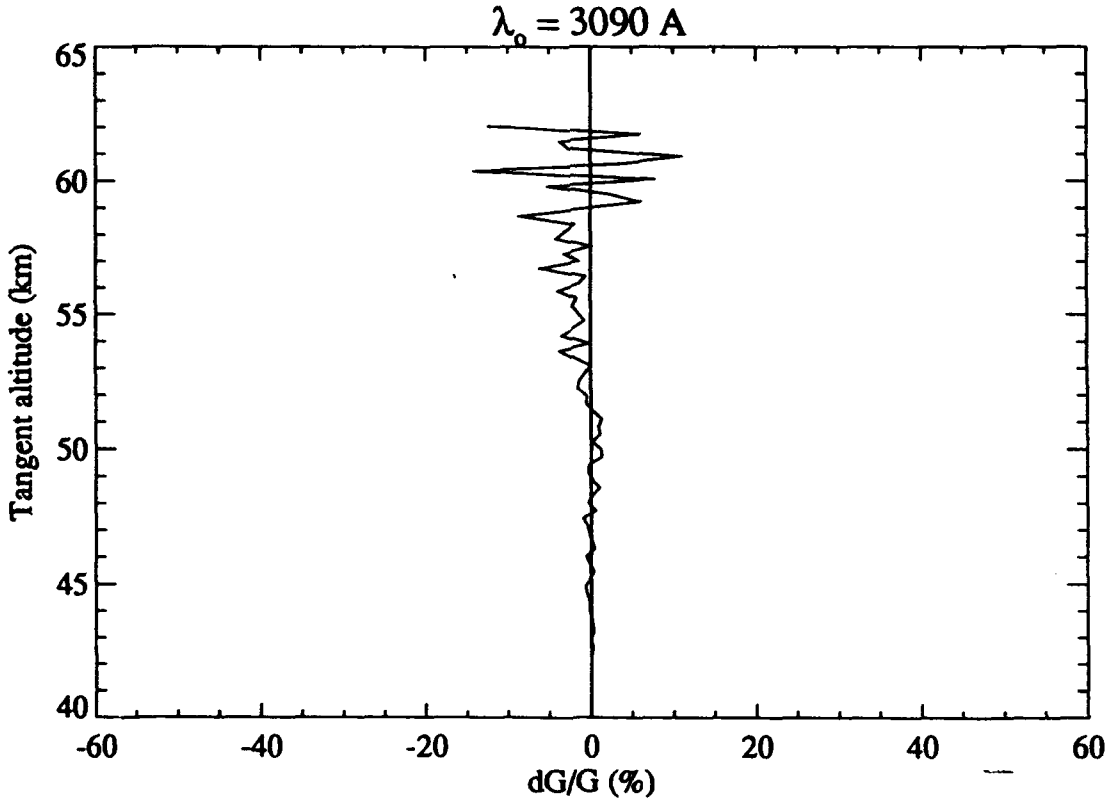
λ0 = 3090 A
Tangent altitude (km)
65
60
55
50
45
40
-60
-40
-20
0
20
40
60
dG/G (%)

Figure 1

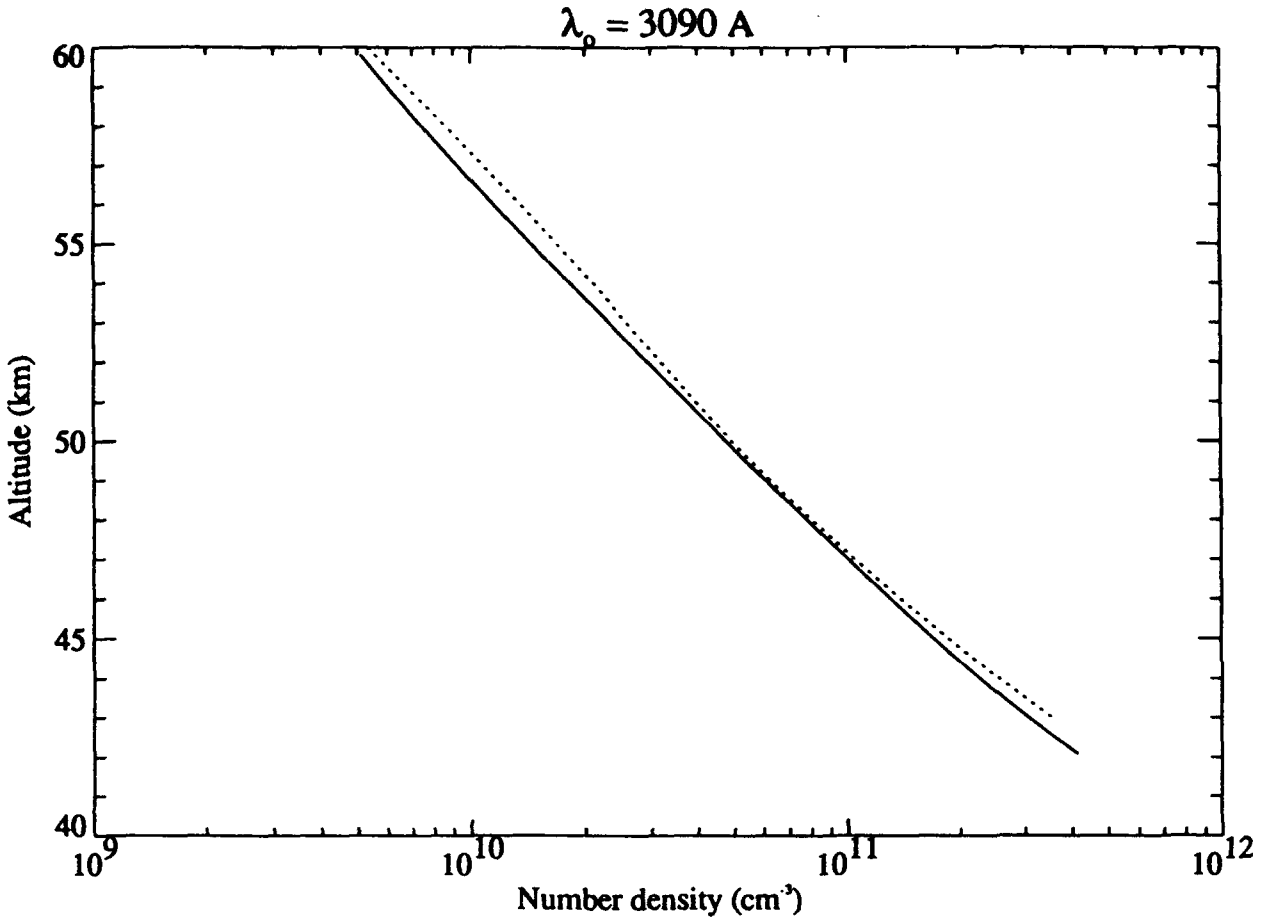
λ_o = 3090 A
60
55
50
45
40
Altitude (km)
10^9
10^{10}
10^{11}
10^{12}
Number density (cm^{-3})

Figure 2

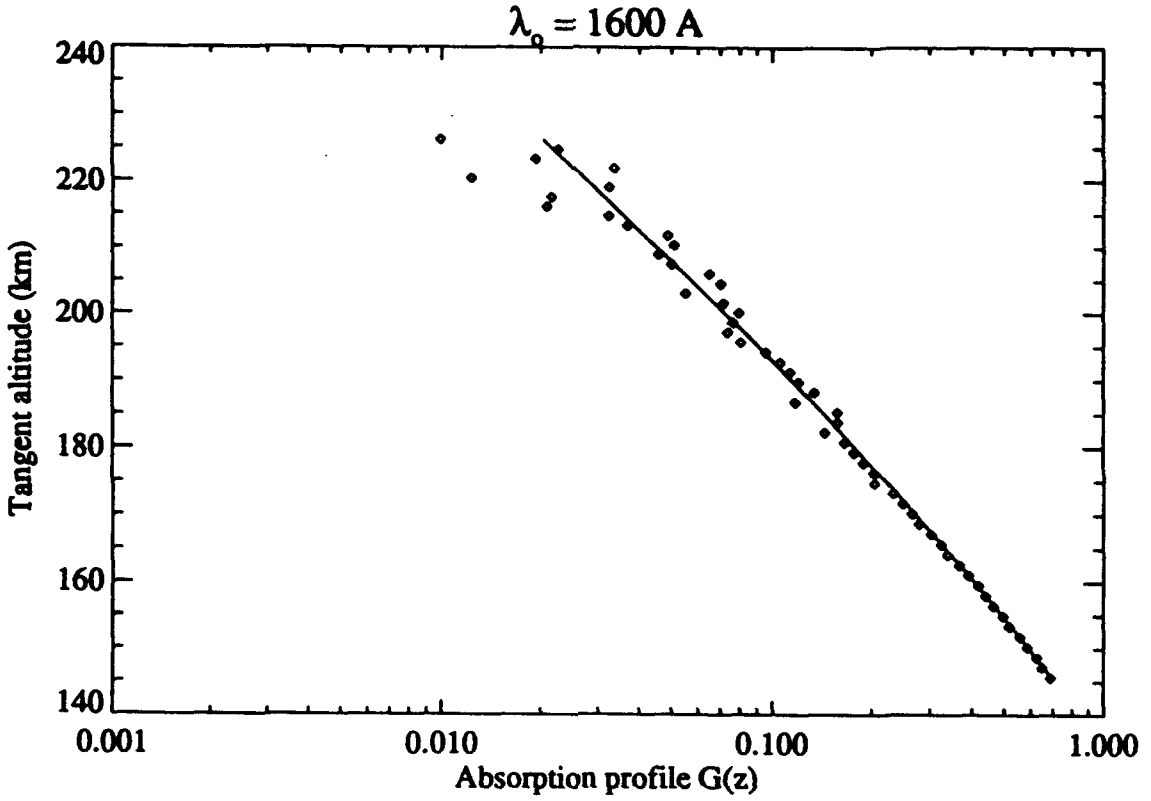
λ_o = 1600 A
240
220
200
180
160
140
Tangent altitude (km)
0.001
0.010
0.100
1.000
Absorption profile G(z)

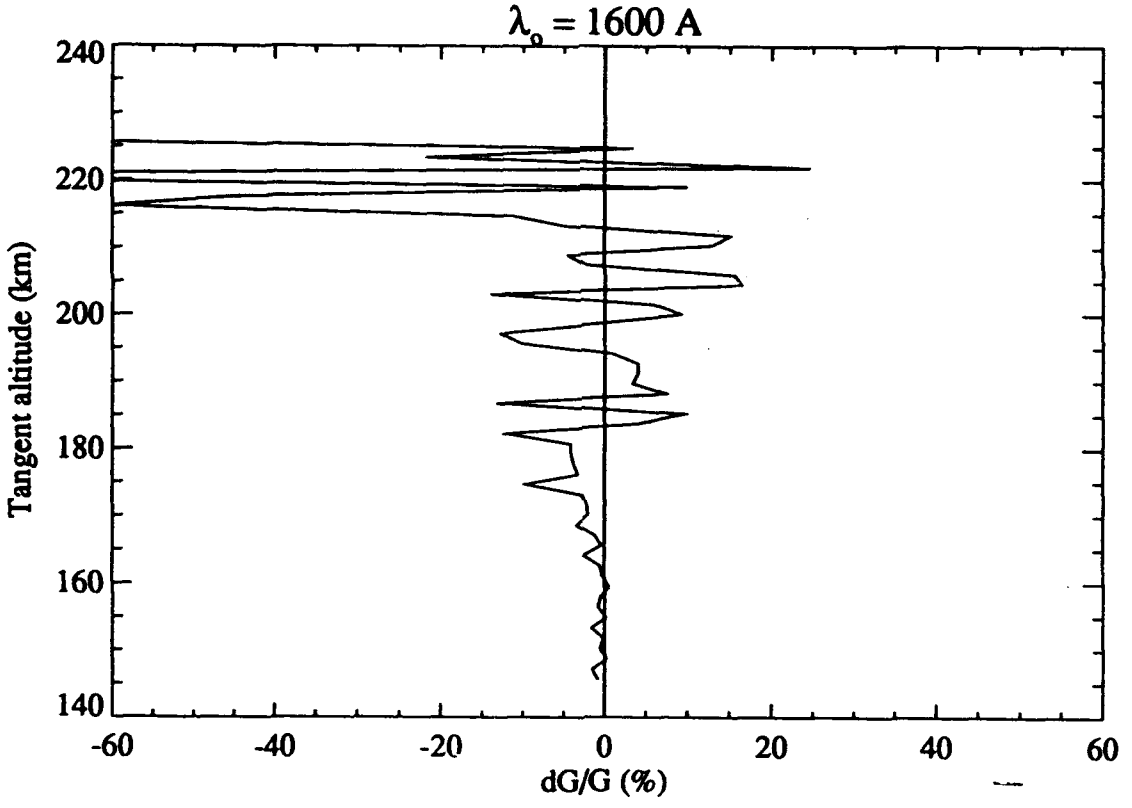
λ_o = 1600 A
240
220
200
180
160
140
Tangent altitude (km)
-60
-40
-20
0
20
40
60
dG/G (%)

Figure 3

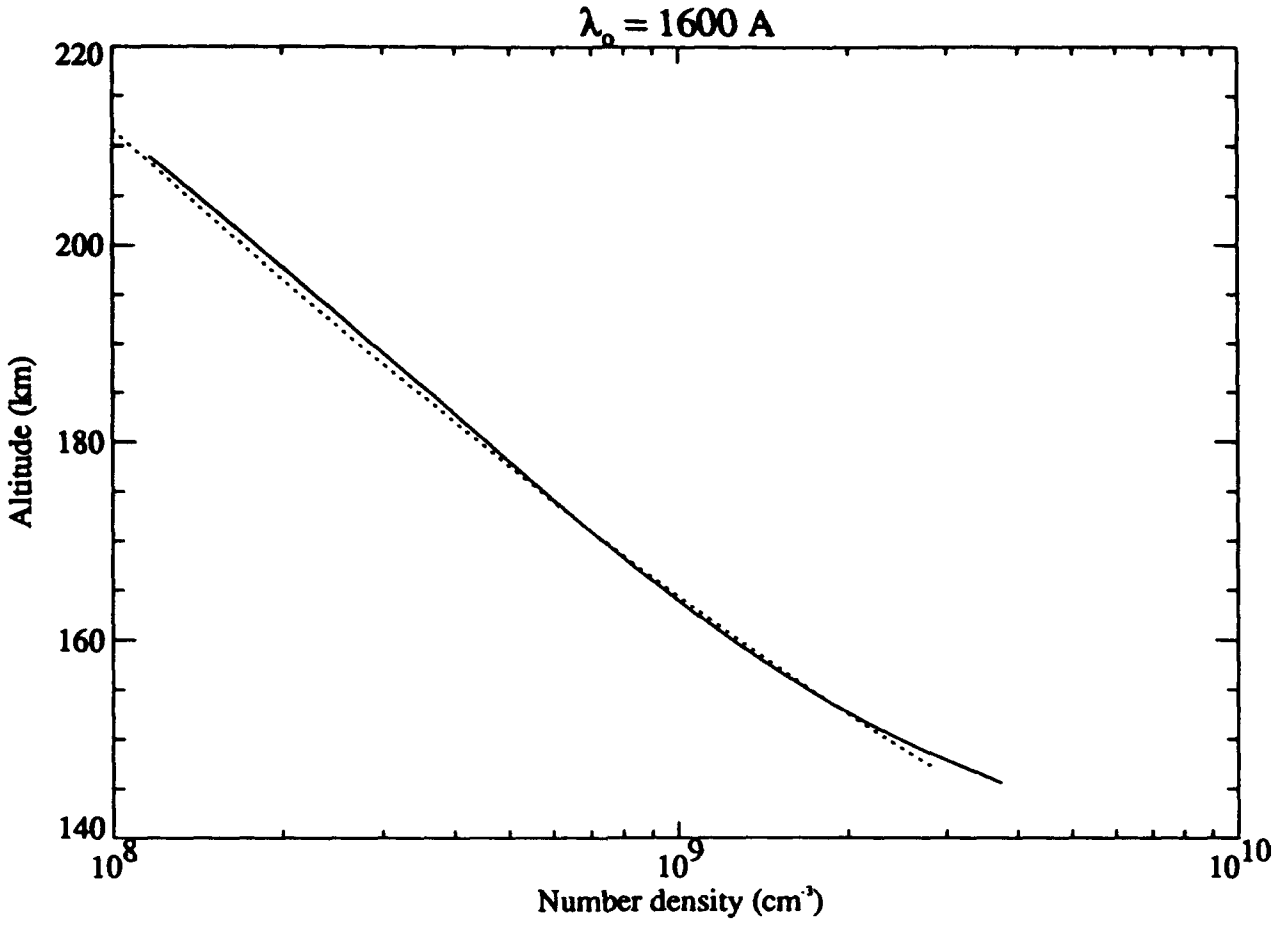
$\lambda_o = 1600$ A
220
200
180
160
140
Altitude (km)
10^8
10^9
10^{10}
Number density (cm^{-3})

Figure 4

J. Quant. Spectrosc. Radiat. Transfer Vol. 46, No. 6, pp. 483–506, 1991
Printed in Great Britain.

0022-4073/91 $3.00 + 0.00

ATMOSPHERIC CONSTITUENT DENSITY PROFILES FROM FULL DISK SOLAR OCCULTATION EXPERIMENTS

J. D. LUMPE,† C. S. CHANG, and D. J. STRICKLAND
Computational Physics, Inc., P.O. Box 360, Annandale, VA 22003, U.S.A.

(Received 22 April 1991)

Abstract—An algorithm is presented for the retrieval of atmospheric number density profiles by inversion of full disk solar occultation data. A general derivation of the normalized absorption profile obtained from such measurements is first given, assuming an arbitrary solar intensity distribution. Using Fourier transform techniques, the resulting integral equation is then solved exactly to yield an expression for the number density in terms of the measured absorption profile. This exact mathematical solution of the integral equation eliminates the need for an iterative solution based on an assumed model density profile and makes the inversion algorithm presented here unique among the currently used algorithms known to the authors. The formal solution is implemented numerically by introducing a suitable representation of the data in terms of Laguerre polynomials, and model calculations are presented for the special case of a uniform solar intensity distribution. The results of these calculations are used to demonstrate the convergence properties of the algorithm and its suitability for accurate reproduction of several representative model density profiles with both constant and altitude-dependent scale heights. Finally, a simple numerical calculation is performed to estimate the effect of nonuniform solar intensity distributions on the retrieved density.

1. INTRODUCTION

In this paper, we describe mathematical methods which can be used to deduce the number of density profiles of atmospheric constituents from solar occultation measurements. This technique uses an Earth-orbiting detector to measure the relative change in solar irradiance as the Sun is occulted by the limb of the Earth (either sunrise or sunset). At a given wavelength, the signal is attenuated due to photo-absorption by the species present in the atmosphere which absorb solar radiation at that wavelength. The measured transmission profile therefore contains information about the combined slant path column density of all of these species. In the special case in which there is one dominant absorber at the wavelength of interest, the data are directly related to the column density of that species. Because the occultation technique involves a relative measurement, with normalization given by the measured solar irradiance above the atmosphere during each event, the results are independent of instrument calibration. This is a very advantageous feature because it tends to negate the effects of instrument degradation over time. On the other hand, the inversion of full disk occultation data presents special problems because the apparent size of the source, as seen by the detector, is generally large compared to the local atmospheric scale height. A single measurement therefore consists of light received from widely separated ray paths, which collectively sample a region of the atmosphere over which the density distribution can vary significantly.

A good deal of work performed in the past was related to stellar occultation measurements,[1] or to measurements which view only a small fraction of the solar disk.[2] The calculations in this case are relatively straightforward since a simple exponential relationship exists between the measured transmission profile and the slant column density at each altitude. In general, however, the solar occultation problem requires an integration over the finite source to generate the transmission profile, and therefore the inversion process involves the solution of a nonlinear integral equation. Previous attempts at deducing species concentrations from full disk solar occultation data relied on an iterative approach based on the assumption of an initial model density profile.[3] The integral

†To whom all correspondence should be addressed.

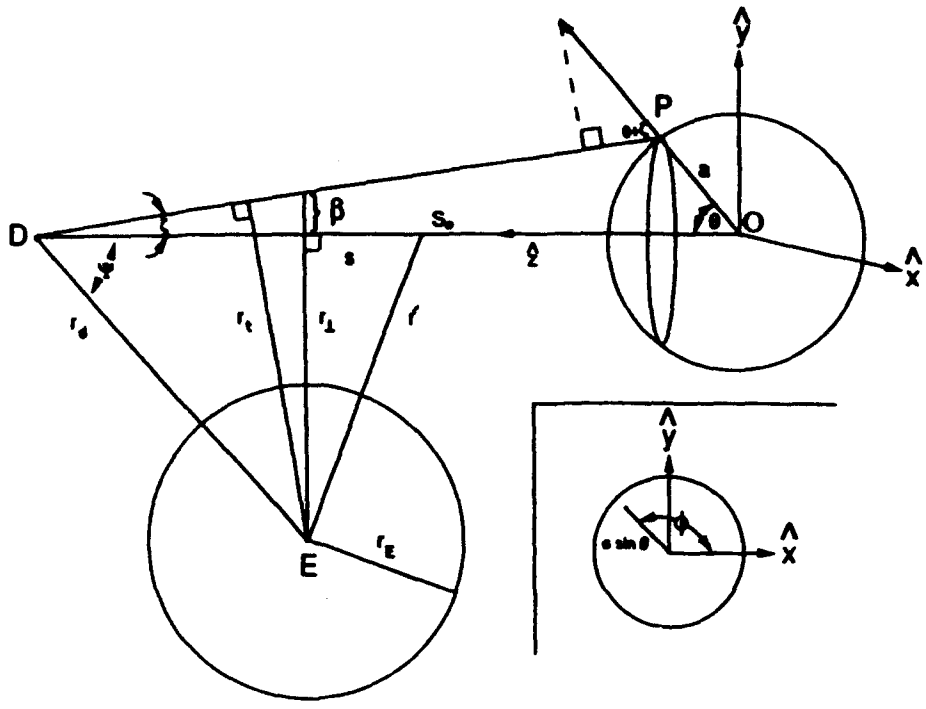

Fig. 1. Viewing geometry for the solar occulation experiment.

Here, $I(\lambda, \theta, \phi)$ is the unattenuated solar flux (photons/Å/sr/sec) at wavelength λ from the source point $P = (\theta, \phi)$; $\sigma(\lambda)$ is the absorption cross section, $N[r_t(\theta, \phi)]$ is the slant column density corresponding to an integration along the line-of-sight from detector to the point P, defined by the tangent radius r_t, and $Q(\lambda)$ is the relative responsivity function of the instrument. The geometric factor $\cos(\theta + \zeta)$ gives the projection of a light ray originating at point P along the line of sight to the detector. It should be noted that F is a function of two variables: the tangent radius $r_\perp$ defined by a look angle Ψ to the center of the source and the observation wavelength λ.

The first integration in Eq. (1) is over the bandwidth of the instrument. The integration over angles (θ, ϕ) is a consequence of the finite source size and represents the essential difference between the solar and stellar occultation problems. This added complexity makes the inversion of the extended source problem, i.e., the solution of Eq. (1) for N in terms of F, much more difficult than for the point source problem.

Equation (1) can be simplified by making two mathematical approximations based on the geometry of Fig. 1. We first note that $|\zeta| \leqslant \zeta_m \ll 1$, where ζ_m is the solar half angle ($\sim 15'$), and therefore the projection factor $\cos(\theta + \zeta) \approx \cos\theta$. Second, we use the fact that $S_0 \gg a \gg r_d$, where S_0 is the Sun-to-detector distance, a is the solar radius and r_d the orbit radius, to make the approximation $\theta_{max} = \sin^{-1}[1 - (a/S_0)^2]^{1/2} \approx \pi/2$. Finally, we make the physical assumption of azimuthal symmetry in the solar flux distribution, so that $I(\lambda, \theta, \phi) = I(\lambda, \theta)$. Equation (1) then becomes

$$F(\lambda, r_\perp) = \frac{1}{K} \int_{\Delta\lambda} d\lambda Q(\lambda) \int_0^{\pi/2} d\theta \sin\theta \cos\theta I(\lambda, \theta) \int_0^{2\pi} d\phi e^{-\sigma(\lambda) N(r_\perp - \beta \sin\theta \cos\phi)} \tag{2}$$

and

$$K = 2\pi \int_{\Delta\lambda} d\lambda Q(\lambda) \int_0^{\pi/2} d\theta \sin\theta \cos\theta I(\lambda, \theta),$$

where we have defined the quantity $\beta = r_t a / S_0$, with $r_t = (r_d^2 - r_\perp^2)^{1/2}$ (see Fig. 1).

This result may be rewritten in a more transparent form by introducing a change of variables from (θ, ϕ) to $(\mu = \cos\theta, y = \beta \sin\theta \cos\phi)$ and interchanging the order of integrations to obtain

$$F(z) = \int_{\Delta\lambda} d\lambda Q(\lambda) \int_{-\beta}^{\beta} dy H(\lambda, y) e^{-\sigma(\lambda) N(z + r)}, \tag{3}$$

the measurement region extends to much higher altitudes, it is straightforward to include the next term in the expansion, of order z/r_E, in Eq. (9). Finally, it is convenient to make one more change of variables to the dimensionless quantity $u = [(z' - z)/\beta]^{1/2}$, which leads to the following expression for the number density:

$$n(z) = -\frac{1}{\pi}\sqrt{\frac{2\beta}{r_E}}\int_0^\infty du \left.\frac{dN(z')}{dz'}\right|_{z'=\beta u^2+z}. \tag{10}$$

For numerical computation, Eq. (10) has an advantage over Eq. (9) in that there is no singularity at the lower limit.

In concluding this section, we wish to point out that Eqs. (3)–(5) can also be obtained if the radiation source is treated as a two-dimensional disk rather than a sphere, as was done here. The equivalence of the two geometries can be established provided that $\zeta_m \ll 1$, i.e., the ratio of the radiation source size to the observing distance is much less than unity. For satellite observations of the Sun, $\zeta_m \approx 4 \times 10^{-3}$, and therefore the solar disk geometry will be an excellent approximation to the exact treatment given here. Roble and Norton[3] used the solar disk geometry and obtained an expression similar to Eq. (3). However, the function $H(\lambda, y)$ defined in Eq. (4) appears to differ from their result except in the limit of a uniform solar intensity distribution, $I(\lambda, \mu) \to I(\lambda)$. This difference results from different interpretations concerning the nature of the intensity distribution across the Sun. We believe that the derivation presented here is the most general possible and is consistent with actual solar observations.

3. FOURIER TRANSFORM SOLUTION

For the purpose of the present work, we shall make the assumption that the variation of $\sigma(\lambda)$ over the instrument bandwidth in Eq. (3) can be ignored, or suitably averaged, in performing the inversion. The validity of this assumption depends on the interplay between two factors: the exact bandwidth of the instrument and the detailed structure of the absorption cross section over this bandwidth. In practice this must be evaluated for the particular case of interest. Assuming a sufficiently narrow bandwidth and a smoothly varying $\sigma(\lambda)$, however, the approximation is reasonable. While this assumption simplifies the solution of Eq. (3) significantly, it is not essential to the inversion algorithm presented in the following sections. A straightforward generalization of the following solution which allows for the full functional dependence of $\sigma(\lambda)$ will be given elsewhere.[4] For the present, we will assume that $\sigma(\lambda) = \sigma_0$, a constant evaluated at the center of the bandpass. The function $I(\lambda, \mu)$ can then also be replaced in Eqs. (4) and (5) by its value at the central wavelength, or one may use the fully folded solar spectrum defined by

$$I_{\Delta i}(\mu) = \int_{\Delta i} d\lambda Q(\lambda) I(\lambda, \mu). \tag{11}$$

For simplicity of notation, we will subsequently denote this effective solar intensity distribution by $I_i(\mu)$. Note that with this assumption made, the explicit wavelength integration no longer appears in Eqs. (3) and (5) and the kernel is now a function of the variable y alone, i.e., $H(\lambda, y) \to H(y)$.

In order to facilitate the mathematical development, we next introduce the absorption profile defined by

$$G(z) = 1 - F(z). \tag{12}$$

This function has the useful property that $G(\infty) = 0$ since $F(\infty) = 1$. Equation (3) is then rewritten in the following form:

$$G(z) = \int_{-\beta}^{\beta} dy H(y) \chi(z + y), \tag{13}$$

where

$$\chi(u) = 1 - e^{-\sigma_0 N(u)} \tag{14}$$

From Eq. (14), the column density is given by

$$N(z) = -\frac{1}{\sigma_0}\ln[1-\chi(z)] \tag{24}$$

and, therefore,

$$\frac{dN(z)}{dz} = \frac{1}{\sigma_0}\frac{1}{1-\chi(z)}\frac{d\chi(z)}{dz}. \tag{25}$$

Inserting this result into Eq. (10), the expression for the number density becomes

$$n(z) = -\frac{1}{\sigma_0\pi}\sqrt{\frac{2\beta}{r_E}}\int_0^\infty du\,\frac{\chi'(\beta u^2+z)}{1-\chi(\beta u^2+z)}, \tag{26}$$

where the prime indicates differentiation with respect to the complete argument of χ. Since χ has been expressed in terms of the Fourier transform of the measured extinction profile, Eq. (26) constitutes the desired solution for the number density as a function of tangent altitude.

4. EXPANSION IN LAGUERRE POLYNOMIALS

It is obvious from the results of the last section, and in particular from Eq. (26), that the retrieval of accurate number density profiles from solar occultation measurements requires an accurate evaluation of the integral in Eq. (23). Although this integral looks relatively simple, it is in general highly singular. To see this, we consider the following polynomial parameterization of the solar limb darkening function:

$$I(\lambda,\mu)/I(\lambda,1) = \sum_{j=0}^{m} a_j(\lambda)\mu^j, \tag{27}$$

where the coefficients $a_j(\lambda)$ are empirically determined. Consistent with the discussion in Sec. 3, these will be replaced by their average value over instrument bandwidth, and denoted simply by a_j. The kernel then takes the form

$$H(y) = \frac{1}{K}\sum_{j=0}^{m}\frac{2^{j+1}}{\beta^{j+1}}a_j(\beta^2-y^2)^{(j+1)/2}B\left(\frac{j}{2}+1,\frac{j}{2}+1\right), \tag{28}$$

where $B(x,y)$ is the beta function. The corresponding function $Y(p)$ becomes

$$Y(p) = \frac{4\sqrt{\pi}}{K}\sum_{j=0}^{m}2^{\nu/2}a_j B\left(\frac{j}{2}+1,\frac{j}{2}+1\right)\Gamma\left(\frac{J+3}{2}\right)\frac{J_{j/2+1}(\beta p)}{(\beta p)^{j/2+1}}. \tag{29}$$

Here, J_ν is the Bessel function of order ν, $\Gamma(x)$ is the gamma function and the normalization factor is $K = \pi\Sigma_j a_j/(j+2)$.

The function $Y(p)$ has, in general, an infinite number of real zeros p_k, which means that the integrand in Eq. (23) has an infinite number of simple poles on the real axis. In addition to the p_k, there will also be singularities in the function $\tilde{G}(p)$ and the integral in Eq. (23) is determined by the sum of residues at these poles. Schematically, we write this sum as follows:

$$\chi(z) = 2\pi i\left[\sum_k R_k^{(1)} + \sum_j R_j^{(2)}\right] = \chi^{(1)}(z) + \chi^{(2)}(z), \tag{30}$$

where R_j and R_k are the residues evaluated at the poles of $\tilde{G}(p)$ and $1/Y(p)$, respectively. Since $z \geq 0$ by definition, the contour is closed in the upper half plane and only poles on the real axis or with positive imaginary parts contribute to the integral. The contribution from the poles of $1/Y(p)$ is of the form

$$\chi^{(1)}(z) = C\sum_k e^{ip_k z}\frac{\tilde{G}(p_k)}{Y'(p_k)}, \tag{31}$$

where $\tilde{\Psi}_n(p)$ is the Fourier transform of $\Psi_n(z)$. This sum may be evaluated analytically using

$$\int_0^\infty du e^{-su} L_n(u) = \frac{(s-1)^n}{s^{n+1}}, \tag{39}$$

with the result

$$\tilde{\Psi}_n(p) = \frac{1}{\sqrt{2\pi}} \frac{(ip - \frac{1}{2})^n}{(ip + \frac{1}{2})^{n+1}}. \tag{40}$$

The function $\tilde{G}(p)$ therefore has a single pole of order $n+1$ at $p = i/2$. The reader should keep in mind that the conjugate variable p is also now a dimensionless quantity, consistent with the substitution $p \to \beta p$. Combining Eqs. (23), (38) and (40), we can write $\chi(z)$ in the form

$$\chi(t) = \sum_{n=0}^{\infty} g_n \Gamma_n(t), \tag{41}$$

where the function $\Gamma_n(t)$ is defined by

$$\Gamma_n(t) = \frac{1}{2\pi} \int_{-\infty}^{\infty} dp e^{ipt} \frac{1}{Y(p)} \frac{(ip - \frac{1}{2})^n}{(ip + \frac{1}{2})^{n+1}}. \tag{42}$$

In order to evaluate this integral, we write

$$\frac{1}{(ip + \frac{1}{2})^{n+1}} = (-1)^n \frac{1}{n!} \left(\frac{d}{d\omega}\right)^n \frac{1}{(ip + \omega)} \bigg|_{\omega = 1/2} \tag{43}$$

and, therefore,

$$\begin{aligned} \Gamma_n(t) &= \frac{(-1)^n}{2\pi} \frac{1}{n!} \left(\frac{d}{d\omega}\right)^n \int_{-\infty}^{\infty} dp e^{ipt} \frac{1}{Y(p)} \frac{(ip - \frac{1}{2})^n}{ip + \omega} \bigg|_{\omega = 1/2} \\ &= \frac{1}{n!} \left(\frac{d}{d\omega}\right)^n e^{-\omega t} \frac{1}{Y(i\omega)} (\omega + \tfrac{1}{2})^n \bigg|_{\omega = 1/2}. \end{aligned} \tag{44}$$

The integral in Eq. (44) has been evaluated by taking the residue at the single pole $p = i\omega$, in accordance with the preceding discussion.

The function $\Gamma_n(t)$ can be evaluated directly from Eq. (44), which results in a closed form solution in terms of associated Laguerre polynomials, $L_n^{(\alpha)}(t)$. However, a more consistent approach is to expand $\Gamma_n(t)$ in terms of Laguerre functions, as we did for $G(t)$. We therefore write

$$\Gamma_n(t) = \sum_{k=0}^{\infty} \gamma_k^n \Psi_k(t), \tag{45}$$

with

$$\gamma_k^n = \int_0^\infty dt \Gamma_n(t) \Psi_k(t). \tag{46}$$

Inserting Eq. (44) into Eq. (46) and using Eq. (39) to evaluate the integral, gives the following result:

$$\gamma_k^n = \frac{1}{n!} \left(\frac{d}{d\omega}\right)^n \frac{1}{Y(i\omega)} (\omega + \tfrac{1}{2})^{n-k-1} (\omega - \tfrac{1}{2})^k \bigg|_{\omega = 1/2}. \tag{47}$$

It is obvious that $\gamma_k^n = 0$ for $k \geq n$, since the factor $(\omega - 1/2)$ then gives zero in the limit $\omega \to 1/2$. The expansion in Eq. (45) is therefore terminated at $k = n$. Upon further evaluation, it can be shown that the coefficients γ_k^n depend only on the difference $(n-k)$ and so can be written as a function of one index only. The reader is referred to Appendix 1 for a detailed derivation of these coefficients. The results can be summarized as follows:

$$\Gamma_n(t) = \sum_{j=0}^{n} \gamma_j \Psi_{n-j}(t), \tag{48}$$

expansion coefficients g_n and the functions $\Gamma_n(t)$ and $\Gamma_n'(t)$ (the prime indicates differentiation) are then calculated to order $n = M$ using Eqs. (37), (48) and (53), respectively. Once these quantities are known, the functions $\chi(t)$ and $\chi'(t)$ are generated from the expansions (41) and (51) and, finally, the Abel integral [Eq. (26)] is evaluated numerically to obtain the number density profile. The data enter only through the coefficients g_n, and this is therefore the only part of the calculation which is specific to a particular measurement. The $\Gamma_n(t)$ and their derivatives are characteristic functions of the problem; they are completely determined by the kernel of the integral equation (13) and thus, ultimately, by the form of the solar intensity distribution through Eq. (4). It is only necessary to calculate them once for a given parameterization of $I_\lambda(\mu)$, i.e., for a given wavelength. This calculation can be done as precisely as possible and the results written to a file for storage. In the actual data analysis, one need only calculate the g_n to the desired order, read in $\Gamma_n(t)$ and $\Gamma_n'(t)$ to the same order and then do the Abel integration. This is a very desirable feature of the algorithm in terms of accuracy and computational efficiency.

The calculation of the expansion coefficients g_n is a critical part of the inversion algorithm, and it is therefore worthwhile to briefly summarize the method used to evaluate the integral in Eq. (37). Because the data only determine $G(t)$ up to a maximum altitude, t_{max}, some physical assumption must be made regarding the behavior of this function as $t \to \infty$. We assume an exponential falloff, so that $G(t) = G(t_{max})\exp[-\alpha(t - t_{max})]$ for $t \geq t_{max}$. The parameter α may be determined by actually fitting the data to this form at t_{max}, or it may, for example, be assumed to be given by $\alpha = \beta/H$, where H is the (assumed) scale height of the absorbing species. In practice, the results show little sensitivity to the choice of α. The integral in Eq. (37) is evaluated by breaking the integration region into intervals determined by successive zeros of $\Psi_n(t)$, and integrating over each interval using an adaptive Romberg integration scheme. In performing the integration it is necessary to interpolate the measured profile $G(t)$ from the data grid onto the integration grid. Because realistic data always contain some statistical scatter, or noise, the profile $G(t)$ will not in general be smooth in the sense of an analytic function. It is important to realize that, in the limit as the number of terms in Eq. (34) goes to infinity, this noise in the data will be reproduced exactly. By truncating the expansion to a smaller number of terms, we are effectively low pass filtering the data, which allows us to control the amount of noise which is passed on to the density profile. Treatment of noisy data and a detailed discussion of the associated error analysis will not be included here but will be presented in a forthcoming paper.[4] In the present calculations the function $G(t)$ is smooth by construction (see discussion in Sec. 5.2) and it can be accurately evaluated at each integration point by doing a quadratic interpolation on the log of the data profile. As the results presented below demonstrate, the above procedure yields a very accurate determination of the g_n.

For the purpose of illustration, we will consider the case of a uniform solar intensity distribution in the results which follow. While this is the simplest possible case, it contains all the essential features of the solution and is sufficient to demonstrate the convergence properties and the accuracy of the calculation. For this case the function $Y(p) = 2J_1(p)/p$ and therefore the zeros needed to calculate the coefficients γ_j and ϵ_j [see Eqs. (49) and (54c)], are simply the zeros of the first order Bessel function, which are known analytically. In general, the roots of the equation $Y(p) = 0$ must be determined numerically since no analytic solution exists for arbitrary $Y(p)$ as given by Eq. (29). Note that in the present case $Y'(p_k)$ is proportional to $J_0(p_k) = (-1)^k|J_0(p_k)|$, so that the series in Eqs. (49) and (54c) alternate. Convergence is therefore slow and it is essential that the summation be done exactly to all orders in order to obtain accurate results for the coefficients γ_j and ϵ_j. In Appendix 2 we briefly discuss the method used to sum the series in Eq. (49); the same arguments apply to the evaluation of Eq. (54c).

In Figs. 2 and 3 the functions $\Gamma_n(t)$ and $\Gamma_n'(t)$ are plotted for several representative values of n. The maximum value $t = 5$ corresponds to an altitude range $z_{max} - z_{min} = 5\beta \approx 60$ km. These functions retain the general oscillatory behavior characteristic of the $\Psi_n(t)$; the frequency of oscillation is higher for larger n and, for a given order, decreases as t increases. However, unlike the $\Psi_n(t)$, which have an $n^{-1/4}$ dependence, the $\Gamma_n(t)$ are seen to increase with increasing order. In addition, for a given value of n, $\Gamma_n(t)$ is in general substantially larger than $\Psi_n(t)$, especially for large n. Because of the different behavior of the two functions in the limit $n \to \infty$, the series in Eq. (41) will not converge as fast as the original expansion for the data given by Eq. (34), and

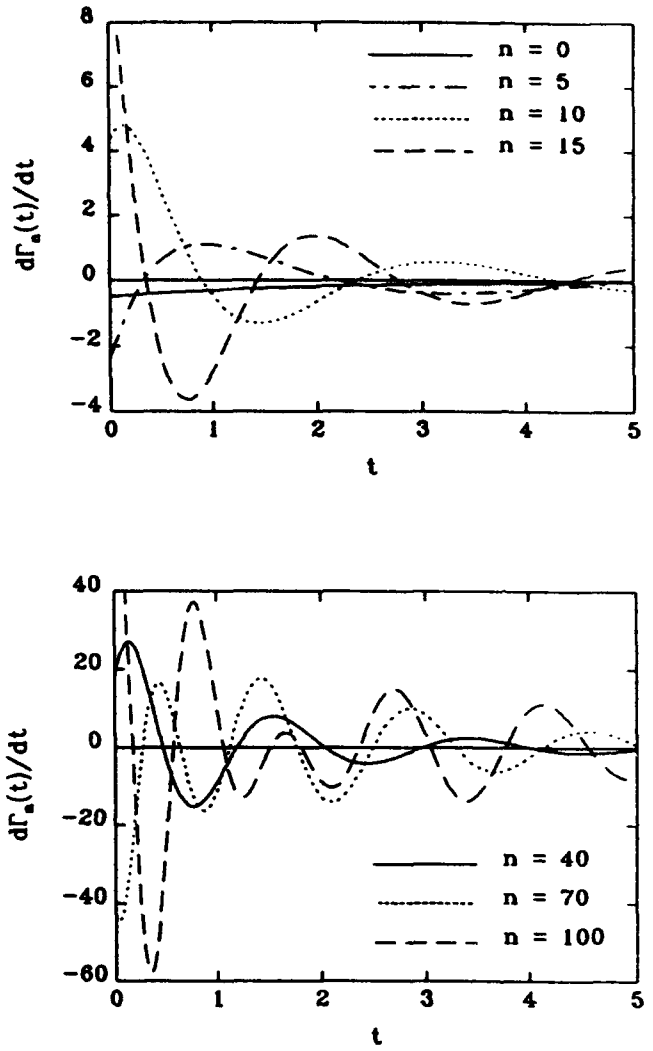

Fig. 3. Derivative of the functions $\Gamma_n(t)$ for the case of a uniform solar intensity distribution.

representative density profiles. A systematic application of the algorithm to the analysis or realistically simulated data for specific atmospheric constituents is deferred to a forthcoming paper.

We first consider the case of a purely exponential model density profile of the form $n_{mod}(z) = n_0 \exp(-z/H)$, where the scale height H is independent of altitude. This is the simplest realistic form of the model density and provides the least stringent test of the algorithm, since there is no vertical structure to reproduce in the profile. The most important physical parameter in this problem is the ratio $\delta = H/2\beta$, which is a measure of how much the density varies at the tangent point due to the finite extent of the Sun. One would expect that as $\delta \to \infty$, the normalized absorption profile yields the species column density directly, since $G(t) \approx \chi(t)$ from Eq. (13). In this limit the solar occultation problem becomes equivalent to the point source problem.

In all the examples to follow, the absorption cross section is chosen to be $\sigma_0 = 1$ in order to make the calculations as general as possible. The effect of this normalization is that the column density is now expressed in units of σ_0^{-1}, as is obvious from setting $\sigma_0 = 1$ in Eq. (3). The corresponding normalized number density is expressed in units of $[\sigma_0(\beta r_E)^{1/2}]^{-1}$ [see Eq. (26)]. These calculations may therefore be extrapolated to the case of absorption by a particular species simply by multiplying the resulting number density by this numerical factor, with a cross section appropriate for that species at the wavelength of interest. As a first example, we choose a scale height $H = 5$ km, which implies $\delta \approx 1/5$. The normalized model density profile and the resulting absorption profile

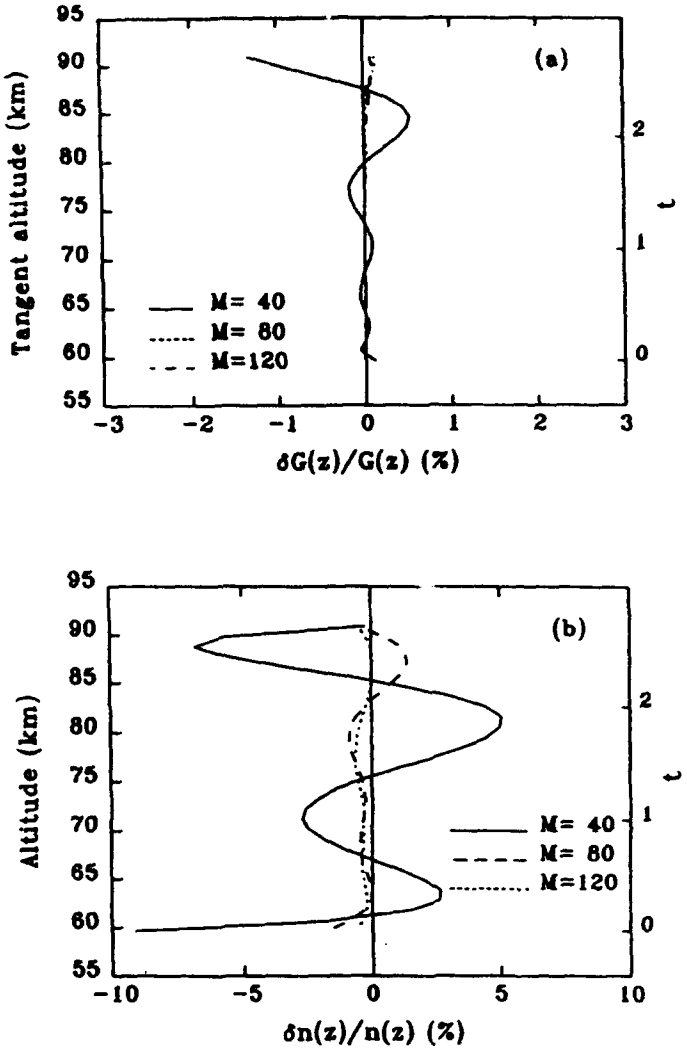

Fig. 5. (a) Percentage error, $[G_m(z) - G(z)]/G(z)$, where $G(z)$ is the data profile plotted in Fig. 4(b) and $G_m(z)$ is obtained from the expansion (34) with $M = 40$, 80 and 120 terms. (b) Corresponding percentage errors in the (normalized) deduced number density as obtained from Eq. (26).

In order to study the convergence of the expansions in more detail, the quantities $\delta G(t)$ and $\delta\chi(t)$ defined by

$$\delta G(t) = G(t) - \sum_{n=0}^{M} g_n \Psi_n(t) \tag{55}$$

and

$$\delta\chi(t) = \chi_{\text{mod}}(t) - \sum_{n=0}^{M} g_n \Gamma_n(t), \tag{56}$$

are shown in Table 1 as a function of M at several altitudes. Here, $\chi_{\text{mod}}(t)$ is given by Eq. (14) with $N(t) = N_{\text{mod}}(t)$. At a fixed altitude, the addition of successive terms in the expansion results in errors which oscillate about zero with decreasing magnitude. Note that $\delta G(t)$ is still converging to zero at $M = 120$, whereas in general $\delta\chi(t)$ reaches a minimum value at some lower order in the expansion and does not change as more terms are added. This saturation is a consequence of the precision of the γ_j coefficients, which is determined by the choice of the cutoff parameter N_j used to evaluate the sum in Eq. (49) (see Appendix 2). As N_j is increased, the asymptotic forms used to approximate the sum become more precise. However, there is always some finite error in the γ_j, and this translates into an effective lower bound on the error $\delta\chi(t)$.

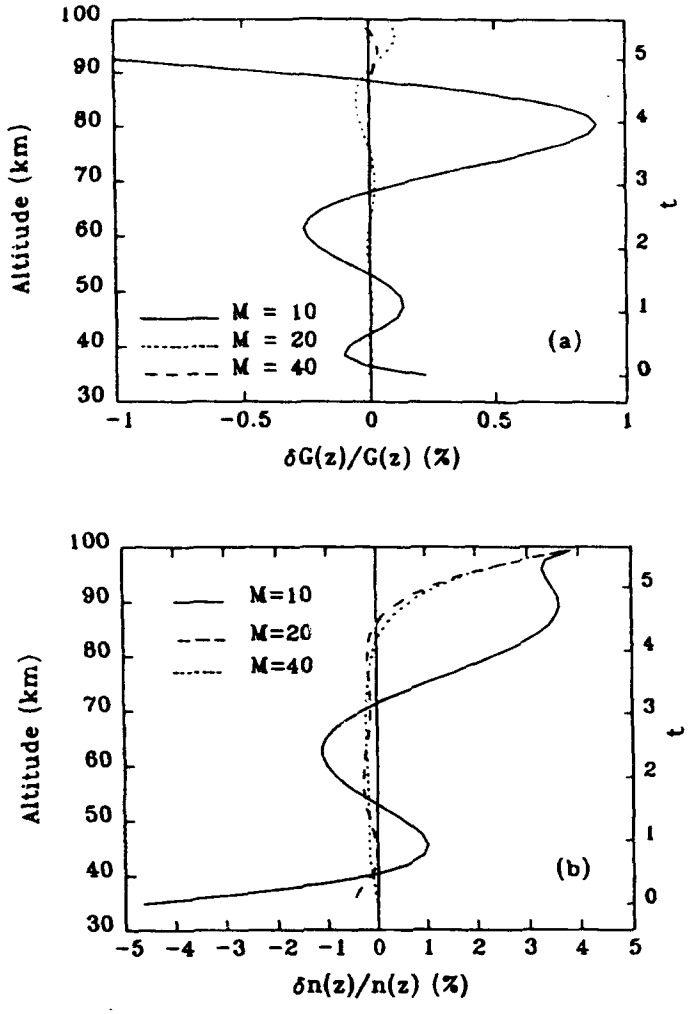

Fig. 6. (a) As in Fig. 5(a) except that the data profile has been generated using a model density with a 12 km scale height and the fit is obtained from Eq. (34) with $M = 10$, 20 and 40 terms. (b) Corresponding percentage errors in the deduced number density profile.

and n_0 was chosen to yield a peak to minimum ratio of 10 at $z = z_0$. The data profile generated by this model density has been plotted in Fig. 8(a). There is a good deal more structure evident in this absorption profile than in the previous example, although it is still very subtle in comparison to the structure in the density itself [see Fig. 9(a)]. The dotted curve in Fig. 8(a) represents the fit to $G(z)$ obtained with $M = 100$, and Fig. 8(b) shows the corresponding percentage error, which is within 1% over most of the altitude range.

In Fig. 9(a), the deduced number density profile is compared to the model profile for the cases $M = 100$, 150 and 200, with corresponding percentage errors plotted in Fig. 9(b). With 100 terms in the expansion, the deduced density underpredicts the sharp minimum at 75 km. The fit in this region is much better when the expansion order is increased but, as Fig. 9(b) indicates, even with $M = 200$, the maximum error is still on the order of 10% at this point in the profile. Nevertheless, these results demonstrate that the inversion algorithm is capable of retrieving more complicated model density profiles, although in general significantly more terms are required in the expansion and the accuracy is somewhat diminished. The important point is that the expansion is still converging so that, in principle, good accuracy can be achieved even in the case of profiles with significant vertical structure. Several methods are currently being investigated which might be used to improve convergence of the expansions in these cases, so that fewer terms will be required.

MIDDLE ATMOSPHERE CLIMATOLOGY

Over the past three years Mr. William Sawchuck of CPI has provided theoretical support to the Middle Atmosphere Program (MAP) at the Naval Research Laboratory. While most of this effort has been directed toward the area of middle atmospheric research. He has also worked on several modeling projects to study the atmospheres of Titan, Io, Triton, and Uranus. Primary contributions are divided into three general areas as outlined below.

Software Development (Data Analysis, Comparison, and Reduction)

The MAP theoretical effort at NRL is currently directed toward the characterization of the spatial and temporal distributions and variability of chemical species, such as ozone and water vapor, in the terrestrial stratosphere and mesosphere. These theoretical efforts have relied on the application of several state-of-the-art computer models which are used to simulate the latitudinal and seasonal distributions of these important trace gases in the atmosphere. A large component of Mr. Sawchuck's work at NRL has been focused toward the development of software which is used in conjunction with these theoretical models to analyze and interpret their output and in many cases compare them to the results of other models and observational data obtained from ground-based, satellite, and spacecraft measurements. Some of this software is also used to reduce large observational data sets for use as model input data. In addition, many specialized model analysis routines as well as several generalized graphical interface routines have been written for use with the MAP atmospheric models . A typical example which was produced with one of these generalized routines can be seen in figure 1.

Software Development/Maintenance (Theoretical Models)

Over the course of this contract the MAP group has maintained several large atmospheric models. These include a 1-Dimensional time dependent photochemical model which incorporates vertical transport by eddy and molecular diffusion, a general 2-Dimensional dynamics model which calculates meridional wind fields from atmospheric temperature data, and a 1-Dimensional neutral and ionospheric planetary model. Over the last few years, Mr. Sawchuck has been involved with the modification and continuing development of all of these models.

One of the primary tasks in this area is the development of a generalized 2-Dimensional Chemical/Dynamical model. The approach to this problem is to merge the above mentioned 1-D photochemical model with the 2-D dynamical model. This includes coding of many of the routines which are related to the incorporation of a self-consistent treatment of chemistry into the dynamical model. As an example, some of these routines, based on the 1-D model, have been designed to read an input list of chemical reactions and reaction rate constants and then calculate the effective production and loss rates for each chemical species. Since the 2-D chemical/dynamical model is computationally intensive, it was necessary to convert the code to run on the NRL Cray X-MP/24.

Project Participation (Theoretical Modeling)

Mr. Sawchuck has participated in several modeling projects during the past three years. These have included investigations on the seasonal variation of water vapor and ozone in the upper mesosphere and the diurnal variation of mesospheric ozone (figure 2). Also, he has been extensively involved in the generation and development of a trace constituent climatology.

Responsibilities included all of the model calculations made for the seasonal variation project as well as that of the diurnal ozone project. These required the development of the model comparison and analysis software for both of these projects. The paper that resulted from the H2O/O3 seasonal variation work won a 1990 Annual Research Publication Award at NRL.

The development and generation of a reference climatology of trace constituents in the atmosphere is based upon the best observational data available, and upon model extrapolations of these data where measurements are not currently available. We are now entering the third year of this project and the database currently includes most of the minor constituents in the atmosphere which affect UV, visible, and IR backgrounds, i.e.,O, O2, N2, NO, NO2, N2O, HNO3, CO, CO2, H2O, and O3 (see figures 3 & 4). This work has recently been presented at a conference of the International Union of Geodesy and Geophysics (IUGG) in Vienna, Austria in August 1991. It is expected that this work will be published when completed.

PUBLICATIONS and REPORTS

Summers M. E. and W.J. Sawchuck, Zonally Averaged Water Vapor and Ozone Climatology, Phase 1: A Self-Consistent Combination of Observations and 1-D Photochemical Model Results. Prepared for the Air Force Geophysics Laboratory (AFGL), 1990.

Summers, M.E., and W.J. Sawchuck, Zonally Averaged Trace Constituent Database, Phase 2: A Climatology of O, NO, NO2, N2O, HNO3, CO, and CO2, In preparation for the Geophysics Laboratory (AFSC), 1991.

Zommerfelds, W.C., K.F. Kunzi, M.E. Summers, R.M. Bevilacqua, D.F. Strobel, and W.J. Sawchuck, Diurnal Variations of Mesospheric Ozone obtained by Ground-based Microwave Radiometry, J. Geophys. Res., 94, D10, 12819-12832, 1989.

Although he is not an author on the following publications, much of Mr. Sawchuck's work was devoted to the projects that resulted in these papers and is evidenced therein.

Bevilacqua, R.M., D. R. Strobel, Summers, M.E., Olivero, J. J., M. Allen, The Seasonal Variation of Water Vapor and Ozone in the Upper Mesosphere: Implications for Vertical Transport and Ozone Photochemistry, 95, D1, 883-893, 1990.

Strobel, D.F., A. Cheng, M. E. Summers, and D. J. Strickland, Magnetospheric Interaction of Triton's Ionosphere, Geophys. Res. Lett., 17, No. 10, 1661-1664, 1990.

Strobel, D.F., M.E. Summers, F. Herbert, B.R. Sandal, The Photochemistry of Methane in the Atmosphere of Triton, Geophys. Res. Lett., 17, No. 10, 1729-1732, 1990.

Summers, M.E. and D.F. Strobel. Photochemistry of the Atmosphere of Uranus, The Astrophysical Journal, 346, 495-508, 1989.

Summers, M.E., D.F. Strobel, Triton's Atmosphere: A Source of N and H for Neptune's Magnetosphere, Geophys. Res. Lett., in press, 1991.

Summers, M.E., D.F. Strobel, R.M. Bevilacqua, X. Zhu, M.T. Deland, M. Allen, G. M. Keating. A Model Study of the Response of Mesospheric Ozone to Short-Term Solar Ultra-Violet Flux Variations, J. Geophys. Res., 95, D13, 22523-22538, 1990.

Summers, M.E., D.F. Strobel, Y.L. Yung, J.T. Trauger, and F. Mills. The Structure of Io's Atomic Corona and Implications for Atmospheric Escape, The Astrophysical Journal, 343, 468-480, 1989.

FIGURE CAPTIONS

Figure 1. Results from the Triton Atmospheric Model which show methane tangential column densities as a function of altitude and pressure. Top panel is for summer hemisphere at 45 degrees latitude and bottom panel is for winter hemisphere at 26 degrees latitude. Solid lines are Voyager 2 UVS measurements. Other lines are model calculations for various values of the eddy diffusion coefficient K. (Strobel and Summers, 1990)

Figure 2. Relative diurnal variation of the 0.4 to 0.8 MHz brightness temperature difference normalized by the average value over 1200 +/- 2hr time period. Thick solid line is ground based microwave data, other lines represent 1-D photochemical model calculations based on various suggested modifications to standard mesospheric odd hydrogen and odd oxygen photochemistry. (Zommerfelds et al., 1989)

Figure 3. Flow chart illustrating the general process by which the Trace Constituent Climatology Database was constructed.

Figure 4. Complete zonally averaged climatology for ozone. (Summers and Sawchuck, 1990)

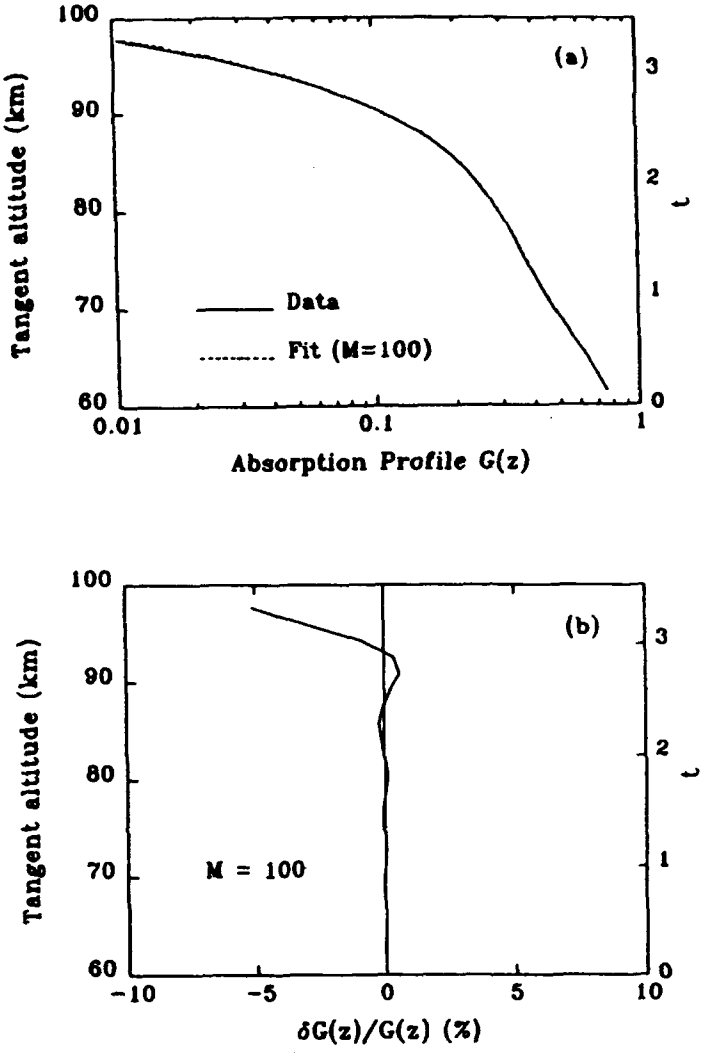

Fig. 8. (a) Solid curve represents the data profile generated using the model density plotted in Fig. 9(a). Dotted curve represents the fit to the data obtained from Eq. (34) with 100 terms. (b) Percentage error in the fit to the data using 100 terms in Eq. (34).

where $I_1(1)$ is the intensity at the center of the disk. This representation corresponds to taking $m = 1$ in Eq. (27). The corresponding value of $Y(i\alpha_j)$, obtained from Eq. (29) after some manipulation, is

$$Y(i\alpha_j) = \frac{6}{3-B}\left[(1-B)\frac{I_1(\alpha_j)}{\alpha_j} + \frac{B}{\sqrt{\pi}\,\alpha_j^2}\left(\cosh\alpha_j - \frac{\sinh\alpha_j}{\alpha_j}\right)\right]. \tag{60}$$

where $I_1(x)$ is the first order modified Bessel function. Solar u.v. limb darkening measurements[6] give a value $B = 0.797$ at 2600 Å, which implies an intensity at the limb ($m = 0$) which is only 20% of the value at the center. In order to determine the effect of this variation on the deduced number density, a data profile was generated using a single term in Eq. (58), with $b_1 = 1$ and $\alpha_1 = 2.5$. This profile was then inverted to obtain number density profiles both with and without the limb darkening effect included. The resulting density profiles are plotted in Fig. 10, where the solid line corresponds to taking $B = 0$ (no limb darkening included) and the dotted curve includes the limb darkening effect by using the value of B quoted above. It is obvious that the effect on the deduced density is substantial; the two curves differ by approx. 50%. The analysis, which ignores limb darkening effects, results in a larger deduced density because it effectively sees more photons and, in order to account for the measured amount of absorption, must deduce a larger density. This simple result demonstrates that it is essential to account accurately for realistic solar intensity distributions in the analysis of solar occultation data. A more systematic study of these effects,

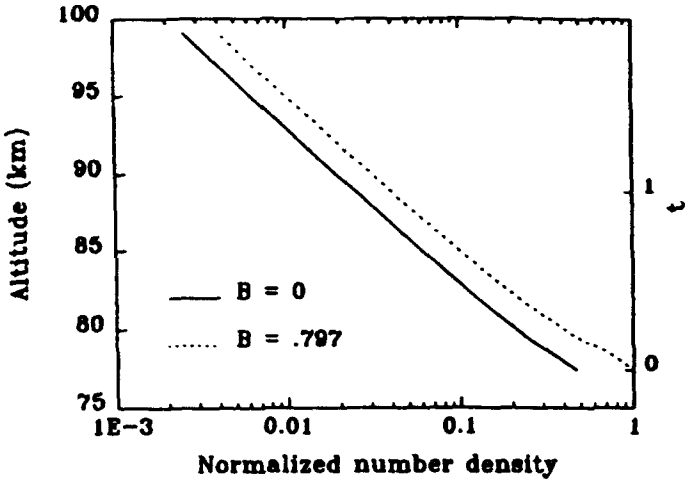

Fig. 10. Deduced number density profiles obtained from the exponential model data profile of Eq. (58) with $j = 1$. The dotted curve results from using a measured u.v. limb darkening coefficient B in Eq. (60), whereas the solid curve is the result obtained by ignoring limb darkening effects.

As an example of the numerical calculations, an algorithm has been successfully developed to extract density profiles in the case of a uniform solar intensity distribution. Numerical results of model calculations presented here demonstrate that the algorithm is capable of accurately reproducing physically motivated model density profiles used to generate model data. In general, the expansions which represent the extracted column density are found to converge more rapidly in the case where the density profile does not contain significant vertical structure. However, accurate results can be obtained even in cases where there is large structure if enough terms are allowed in the expansion. There are currently several options being considered which might be implemented in an effort to improve the convergence and accuracy of the expansions.

The computer code which has been developed to do the calculations for a uniform solar intensity distribution presented here can be generalized to do the analysis for arbitrary intensity distributions outlined in Secs. 3 and 4 of the paper. Preliminary results from the present analysis indicate that the inclusion of realistic limb darkening effects in the calculation has a significant impact on the deduced number density profile and is therefore essential to the retrieval of accurate density profiles from solar occultation data. This question obviously deserves careful numerical study and efforts are currently underway to make the necessary modifications to the code.

In conclusion, we have developed a rigorous mathematical method and accurate numerical procedures to deduce number density profiles of atmospheric species from solar occultation measurements. This approach can be extended to include the analysis of multichannel measurements capable of extracting information about several species simultaneously. It is also hoped that it may be used as a starting point to attack the problem of nonspherical density distributions using a similar measurement.

Acknowledgements—The authors wish to thank M. E. Summers, J. L. Lean, G. E. Brueckner, and M. E. Van Hoosier for discussions which were helpful in the preparation of this paper. This research was supported by the Solar Physics Branch of the Naval Research Laboratory through NASA DPR S-14798-D.

REFERENCES

1. R. G. Roble and P. B. Hays, *Planet. Space Sci.* **20**, 1727 (1972) and references cited therein.
2. W. P. Chu and M. P. McCormick, *Appl. Optics* **18**, 1404 (1979); W. P. Chu, M. P. McCormick, J. Lenoble, C. Brogniez, and P. Pruvost, *J. Geophys. Res.* **94**, 8339 (1989).
3. R. G. Roble and R. B. Norton, *J. Geophys. Res.* **77**, 3524 (1972).
4. J. D. Lumpe, C. S. Chang, and D. J. Strickland, in preparation (1991).
5. P. H. Hays and R. G. Roble, *Planet. Space Sci.* **16**, 1197 (1968); P. H. Hays and R. G. Roble, *J. Atmos. Sci.* **25**, 1141 (1968).
6. O. Kjeldseth Moe and E. F. Milone, *The Astrophys. J.* **226**, 301 (1978).
7. H. Jefferies and B. Jefferies, *Methods of Mathematical Physics*, p. 383, Cambridge Univ. Press, Cambridge, U.K. (1950).

by symmetry, since $p_{-n} = -p_n$ and $Y'(-p) = -Y'(p)$. This follows directly from the fact that $H(y)$ defined by Eq. (6) is an even function of y. Using these results, Eq. (A9) becomes

$$\frac{1}{Y(p)} = 1 + \sum_{n=-\infty}^{\infty} \frac{1}{Y'(p_n)}\left[\frac{1}{p - p_n} + \frac{1}{p_n}\right], \tag{A11}$$

and, therefore,

$$A^{(k)} = \left(\frac{d}{d\eta}\right)^k \left[1 + \sum_{n=-\infty}^{\infty} \frac{1}{Y'(p_n)}\left[\frac{1}{i(\eta + \frac{1}{2}) - p_n} + \frac{1}{p_n}\right]\right]_{\eta=0}. \tag{A12}$$

The first and third terms of Eq. (A12) contribute only for $k = 0$, since they are independent of η. However, since $A^{(0)} = [Y(i/2)]^{-1}$ is known by definition, we are only interested in the result for $k \geq 1$. For general k, we can make use of the relation

$$\left(\frac{d}{d\eta}\right)^k \frac{1}{i(\eta + \frac{1}{2}) - p_n} = (-i)^k k! \frac{1}{(i(\eta + \frac{1}{2}) - p_n)^{k+1}} \tag{A13}$$

and, upon taking the limit $\eta = 0$, we get the final result

$$A^{(k)} = (-i)^k k! \sum_{n=-\infty}^{\infty} \frac{1}{Y'(p_n)} \frac{1}{(i/2 - p_n)^{k+1}} = k!\, B^{(k)}. \tag{A14}$$

It is straightforward to prove that the $B^{(k)}$ are real by considering the symmetry of Eq. (A14) with respect to the substitution $n \to -n$, and therefore the γ_j are real also [see Eq. (A17)].

Inserting Eq. (A14) into (A8), rearranging sums and defining $m = k - 1$ gives

$$\gamma_j = -i \sum_{n=-\infty}^{\infty} \frac{1}{Y'(p_n)} \frac{1}{(i/2 - p_n)^2} \sum_{m=0}^{j-1} \binom{j-1}{m} \left(\frac{-i}{1/2 - p_n}\right)^m. \tag{A15}$$

This relation can be simplified by using the binomial theorem to rewrite the factor

$$\sum_{m=0}^{j-1} \binom{j-1}{m} \left(\frac{-i}{1/2 - p_n}\right)^m = \left[1 - \frac{i}{i/2 - p_n}\right]^{j-1}. \tag{A16}$$

The result is

$$\gamma_j = 8 \sum_{n=1}^{\infty} \frac{1}{Y'(p_n)} \frac{1}{1 + 4p_n^2} \sin(2j\theta_n) \quad (j \geq 1), \tag{A17}$$

where θ_n is defined in Eq. (50), and the sum has been restricted to positive integers only ($n \geq 1$) by use of the symmetry relation $p_{-n} = -p_n$.

APPENDIX 2

Calculation of Expansion Coefficients for Uniform Solar Disk

For the case of a uniform solar intensity distribution, Eq. (49) takes the form

$$\gamma_j = 4 \sum_{k=1}^{\infty} \frac{p_k}{J_0(p_k)} \frac{1}{1 + rp_k^2} \sin(2j\theta_k) \tag{A18}$$

for $j \geq 1$, with $\gamma_0 = [4I_1(1/2)]^{-1}$. Writing $J_0(p_k) = (-1)^k |J_0(p_k)|$ and defining the coefficient

$$a_k^j = 2 \frac{p_k}{|J_0(p_k)|} \frac{\sin(2j\theta_k)}{1 + 4p_k^2}, \tag{A19}$$

we can rewrite Eq. (A18) as

$$\gamma_j = 2 \sum_{k=1}^{\infty} (-1)^k a_k^j. \tag{A20}$$

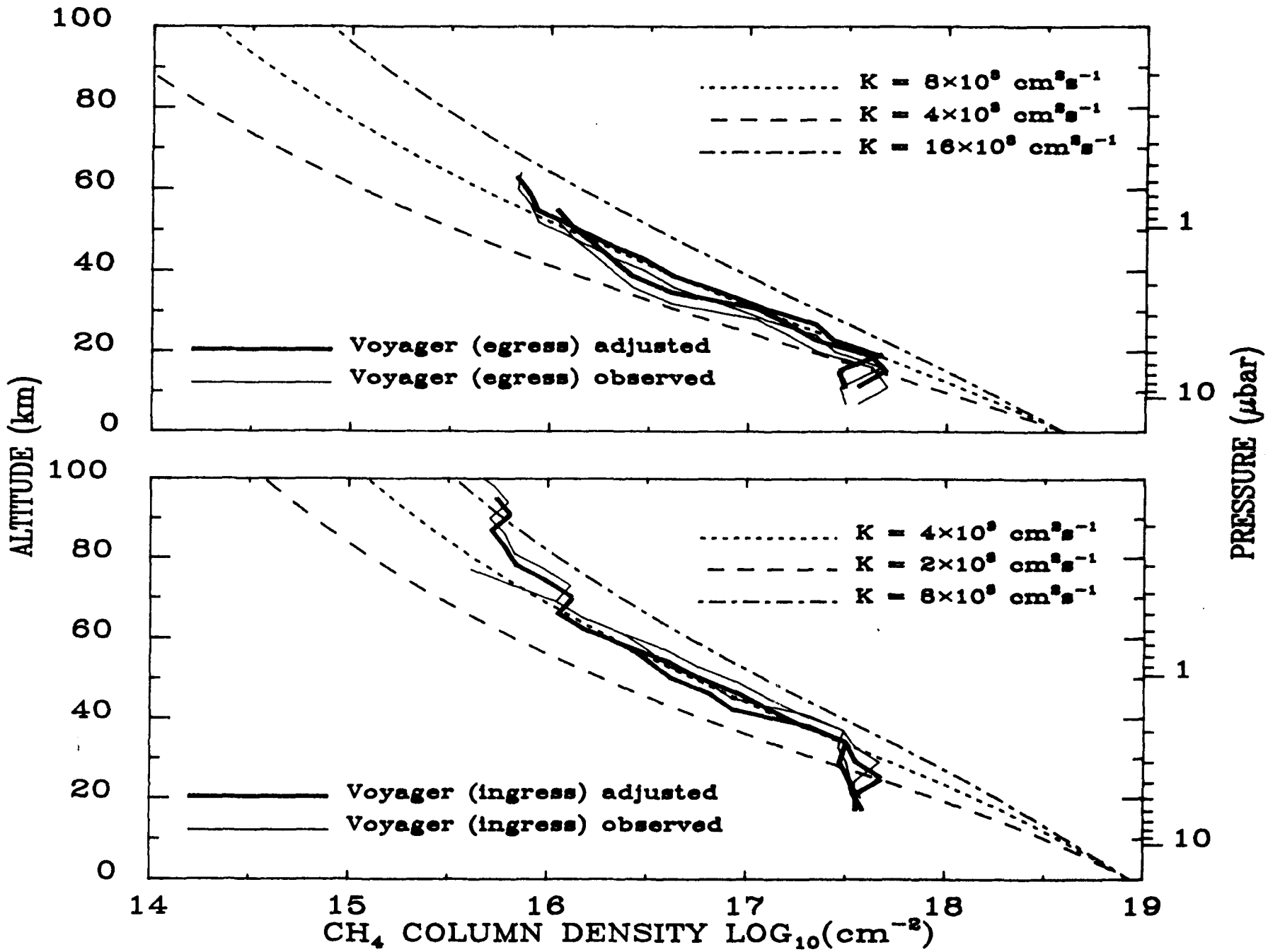
100
80
60
40
20
0
ALTITUDE (km)
K = 8×10⁸ cm²s⁻¹
K = 4×10⁸ cm²s⁻¹
K = 16×10⁸ cm²s⁻¹
Voyager (egress) adjusted
Voyager (egress) observed
1
10
PRESSURE (μbar)
K = 4×10⁸ cm²s⁻¹
K = 2×10⁸ cm²s⁻¹
K = 8×10⁸ cm²s⁻¹
Voyager (ingress) adjusted
Voyager (ingress) observed
14
15
16
17
18
19
CH₄ COLUMN DENSITY LOG₁₀(cm⁻²)

Figure 1

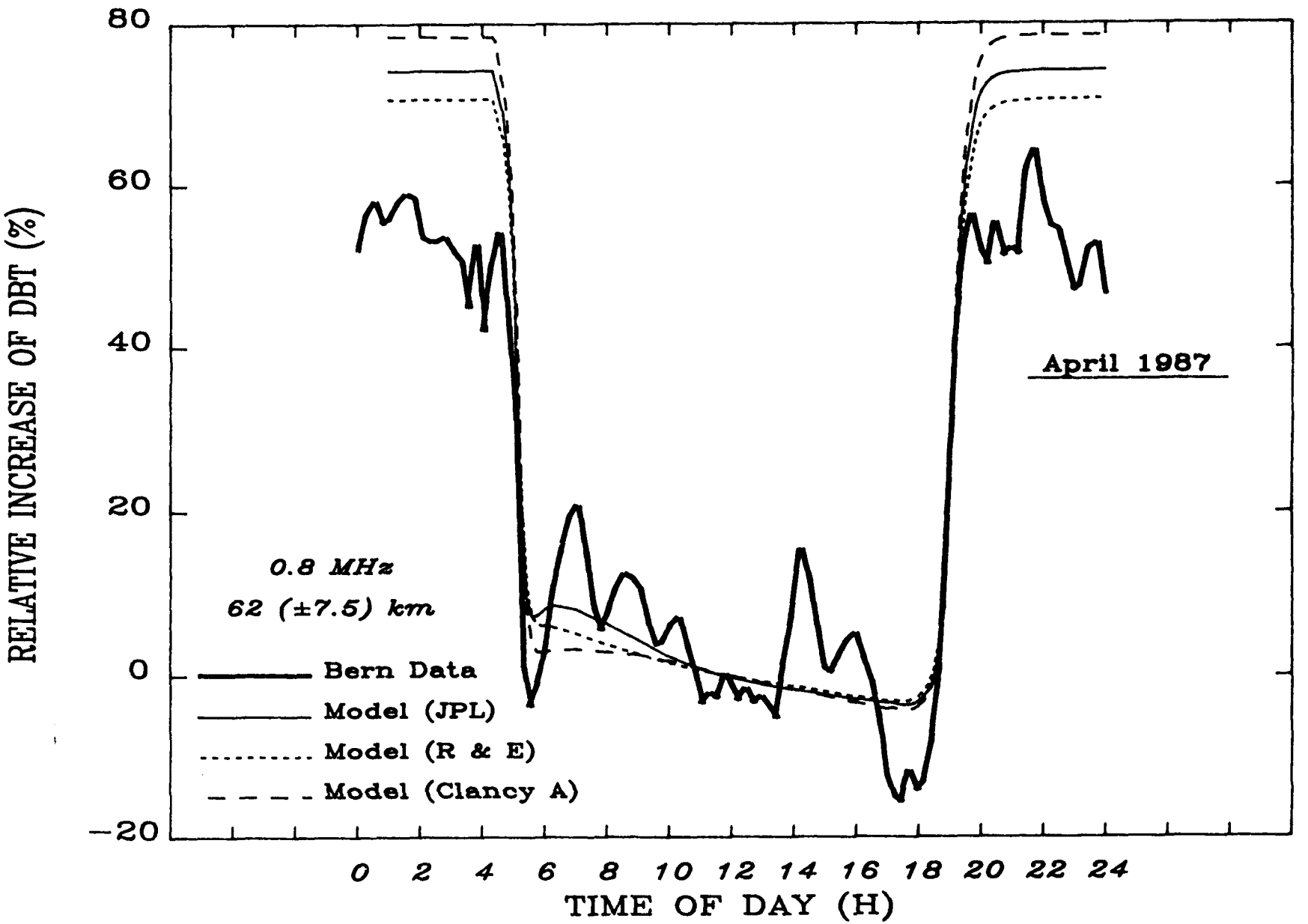
80
60
40
20
0
−20
RELATIVE INCREASE OF DBT (%)
0.8 MHz
62 (±7.5) km
Bern Data
Model (JPL)
Model (R & E)
Model (Clancy A)
April 1987
0 2 4 6 8 10 12 14 16 18 20 22 24
TIME OF DAY (H)

Figure 2

Generation of Trace Constituent Database

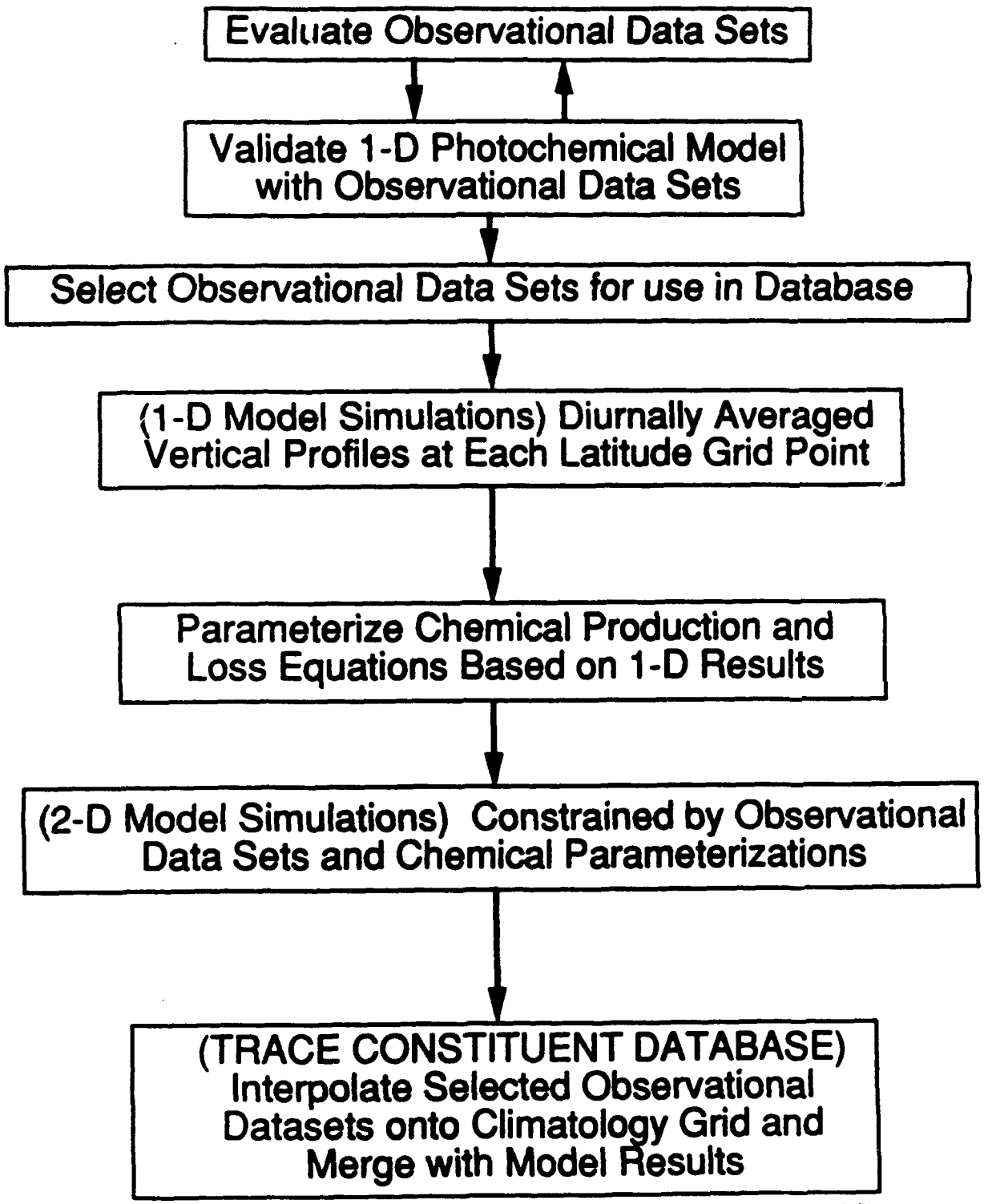

Figure 3

APPENDIX 4

DEVELOPMENT OF A CLIMATOLOGY OF THE MIDDLE ATMOSPHERE FOR NRL'S MIDDLE ATMOSPHERE PROGRAM

Contributor:

W. J. Sawchuck

APPENDIX 5

MODELING OF MILLIMETER-WAVE EMISSIONS OF THE MIDDLE ATMOSPHERE OBSERVED FROM THE GROUND AND DEVELOPMENT OF CONSTITUENT RETRIEVAL ALGORITHMS

Contributor:

D. L. Kriebel

REMOTE SENSING AT MICROWAVE FREQUENCIES

Satellite and ground-based observations at microwave frequencies have proven to be the method of choice for determining abundances of important species in the stratosphere and mesosphere. These observations, combined with a solid and comprehensive theoretical framework, are making an important contribution to an understanding of the middle atmosphere. CPI has been providing theoretical support to NRL in this area through the development of forward model calculations and retrieval method applications.

In the summer of 1989 Ms. Donna Kriebel of CPI's Annandale office began working with Dr. Richard Bevilacqua of NRL on the early phases of this effort. During this period the first versions of the META (Millimeter Emission Temperature of the Atmosphere) code were produced. At the same time a congenial, menu-driven setup code was developed to facilitate selection and modification of required input parameters.

META is an algorithm which generates synthetic emission spectra, using radiative transfer theory, to simulate ground-based microwave measurements. The program avoids some approximations of earlier forward model calculations, and has an added advantage in that flexibility has been a major consideration in its design. For example, it can be used in conjunction with appropriate driver routines to model various observing modes, such as beam-switching or single-beam in single or double sideband configurations. Provision is also made for determining background effects. Inputs include temperature, pressure, and mixing ratio profiles, in addition to the characteristics of the "measuring system". A spectral catalog compiled by the Jet Propulsion Laboratory is consulted for selection of contributing lines according to user-specified criteria. The simulated spectra so generated can then be used in the evaluation and application of various retrieval schemes.

Improvements to the initial version of META include a driver program which permits generation of a number of spectra using different mixing ratio profiles, or different temperature-pressure profiles, calling only those subroutines which are necessary to take into account the new inputs. Improvement of the partition function entailed expansion to include vibrational and electronic parts, whereas previously it was comprised of only a rotational part. In some molecules, such as ozone and ClO, these vibrational and/or electronic states assume some importance. In addition, a new pressure-broadening half-width was incorporated to describe the water vapor lineshape more accurately.

In the ongoing process of code refinement, comparisons were performed in which the effects of varying altitude resolution, varying criteria for individual line selection, and inclusion of the troposphere were studied, as well as differences between species.

Early calculations have supplied useful comparisons with independent results of investigators such as Dr. Brian Connor of NASA. The program has been routinely applied to emissions from H2O, O3, and ClO, and is capable of modeling spectra from a wide variety of other species